Dissertation

submitted to the
Combined Faculty of Mathematics, Engineering and Natural Sciences
of Heidelberg University, Germany
for the degree of
Doctor of Natural Sciences

Put forward by
Jan Kilinc
born in Pforzheim, Germany

Oral examination on the 8th of February 2024

A new setup for experiments with an ultracold ^{23}Na-^{39}K mixture

Referees: Prof. Dr. Markus K. Oberthaler
Jun.-Prof. Dr. Lauriane Chomaz

Abstract

This thesis reports on the development and characterization of a new ultracold atomic mixture experiment, featuring the bosonic species ^{23}Na and ^{39}K. With precise control over both inter- and intra-species interactions, this system serves as an ideal experimental platform for probing demixing dynamics with controlled miscibility.
We set up new laser systems for both atomic species, alongside magnetic field coils featuring precise control, crucial for trapping and adjusting interaction strengths. Additionally, we established and characterized a high-resolution imaging system, proving indispensable for detecting Bose-Einstein condensates.
Following evaporative cooling in a crossed optical dipole trap, a ^{23}Na Bose-Einstein condensate comprising approximately 7×10^4 atoms was achieved. With both, ^{39}K and ^{23}Na, in the trap, we performed atom-loss spectroscopy measurements, identifying several intra- and inter-species Feshbach resonances, providing valuable insights into the different interaction regimes. Substantial three-body losses in this atomic mixture at low magnetic fields pose significant challenges, impeding the achievement of dual-species condensation to date. We give perspectives for the improvement of the cooling strategy to minimize the time spent at these low magnetic fields.

Zusammenfassung

In dieser Arbeit wird über die Entwicklung und Charakterisierung eines neuen experimentellen Aufbaus, basierend auf einer ultrakalten Atommischung aus den bosonischen Atomspezies ^{23}Na und ^{39}K, berichtet. Mit präziser Kontrolle über die Wechselwirkungen zwischen und innerhalb der Atomsorten dient dieses System als ideale experimentelle Plattform für die Untersuchung von Entmischungsdynamik bei kontrollierter Mischbarkeit.

Wir haben neue Lasersysteme für beide Atomspezies sowie Magnetfeldspulen mit präziser Steuerung aufgebaut, die für das Einfangen der Atome und die Einstellung der Wechselwirkungsstärken entscheidend sind. Darüber hinaus haben wir ein hochauflösendes Bildgebungssystem installiert und charakterisiert, das für die Detektion von Bose-Einstein-Kondensaten unverzichtbar ist.

Nach evaporativem Kühlen in einer gekreuzten optischen Dipolfalle konnte ein ^{23}Na Bose-Einstein-Kondensat mit etwa 7×10^4 Atomen erzeugt werden. Mit sowohl ^{39}K als auch ^{23}Na in der Falle führten wir Atomverlustspektroskopie durch und identifizierten mehrere Feshbach-Resonanzen innerhalb und zwischen den Spezies, was wertvolle Einblicke in die verschiedenen Wechselwirkungsregime lieferte. Erhebliche Drei-Körper-Verluste in dieser Atommischung bei niedrigen Magnetfeldern stellen eine große Herausforderung dar, die das Erreichen der Doppel-Spezies Kondensation bisher verhindert hat. Wir zeigen Perspektiven für die Verbesserung der Kühlstrategie auf, um die Zeit, die bei diesen niedrigen Magnetfeldern verbracht wird, zu minimieren.

Contents

CHAPTER 1

Introduction

The first experimental observation of Bose-Einstein condensation (BEC) in a dilute atomic vapour in 1995 [1, 2] gave rise to a new field of research encompassing both atomic and condensed matter physics. Initially, the main focus of research were phenomena associated to the coherent, macroscopic matter-wave properties of these ultracold gases. Prominent examples include the observation of interference between two BECs [3] or the formation of vortices in a stirred BEC [4].

Over the past two decades, enormous progress was driven by two pivotal developments - the tunability of interactions using magnetically tunable Feshbach resonances [5–7] and the application of versatile optical potentials through specially shaped and interfering laser beams, creating periodic potentials [8]. Complete control over the strength and sign of inter-atomic interactions, combined with the ability to manipulate the system's dimensionality through optical potentials, positioned cold atoms as an ideal platform for realizing so-called analog quantum simulators [9, 10]. These quantum simulators offer a means to explore theoretically challenging problems, ranging from examining the universal dynamics of systems far from equilibrium [11, 12] to investigating the dynamics of quantum fields in curved spacetime [13, 14]. Additionally, the quantum simulation of strongly correlated many-body systems [15, 16] aims to address open questions related to high-temperature superconductivity [17, 18] and quantum magnetism [19].

In recent years, many efforts have been dedicated to ultracold atomic mixtures. Such mixture systems have been implemented using distinct hyperfine spin states within the same atomic species [20, 21], as well as through the use of different stable isotopes [22, 23]. Alternatively, entirely separate atomic species have been successfully combined and cooled to dual-species degeneracy [24, 25].

The interactions occurring within each component and between the two play a central role, determining whether the mixture exhibits miscibility or immiscibility. Immiscible fluids, as observed when attempting to mix oil and vinegar, will not mix but rather phase separate. Such phase separation phenomena are omnipresent in nature [26] and have been observed in condensed matter systems [27, 28], biological systems [29, 30],

and quantum systems [31,32]. Due to its relevance in such diverse areas of research, understanding the underlying processes and emergent phenomena associated with demixing dynamics is of fundamental importance.

Manipulating Bose-Einstein condensates using magnetically tunable Feshbach resonances has opened a significant pathway to explore the transition between miscible and immiscible mixtures, thereby enabling control over phase separation dynamics [33,34]. Additionally, the linear coupling of internal states has emerged as an alternative strategy, establishing effective interactions among dressed states and providing control over the spatial mixing-demixing dynamics within these condensates [35–37].

In early experiments exploring Bose-Bose mixtures [32, 33, 38], immiscibility was demonstrated by an asymmetry in the density profiles, connected to the spatial separation into distinct domains. Moreover, exploring the interaction between spatially separated condensates upon collision [21,39] revealed diverse dynamics dependent on the miscibility of the atomic mixture, where, for instance, a counter-intuitive bouncing motion was observed between miscible condensates [40].

The role of interactions in mixture systems was further extended to lower-dimensional setups, exploring demixing instabilities in two-dimensional box potentials [41,42] and quasi-one-dimensional spin mixture configurations [43]. In these studies, the investigation of the time-evolution of phase separation dynamics in immiscible spin mixtures revealed the process of coarsening. Herein, domains of the two components nucleate, and larger domains expand at the expense of smaller ones. This phenomenon often exhibits universal scaling behaviour [44–46], meaning that the typical size of domains increases with time according to a power-law relationship regardless of the initial conditions or microscopic interaction details, but rather emphasizing emergent behaviours during evolution.

The study of demixing dynamics in immiscible atomic mixtures is commonly conducted in a population-balanced system. In contrast, in a strongly population-imbalanced mixture, wherein isolated bosonic impurity atoms are immersed in a Bose-Einstein condensate (BEC) formed by the other atomic species, the quasi-particle description of this simple yet non-trivial many-body system becomes relevant. Resulting from the inter-species interaction, each impurity atom gets dressed by a cloud of Bogoliubov phonon excitations of the BEC, forming the so-called Bose polaron, as illustrated in figure 1.1 A. The polaron exhibits modified properties compared to the bare atom, including an effective mass, a different size, and a modified dispersion relation. In general, the interaction of impurities with a medium plays a pivotal role

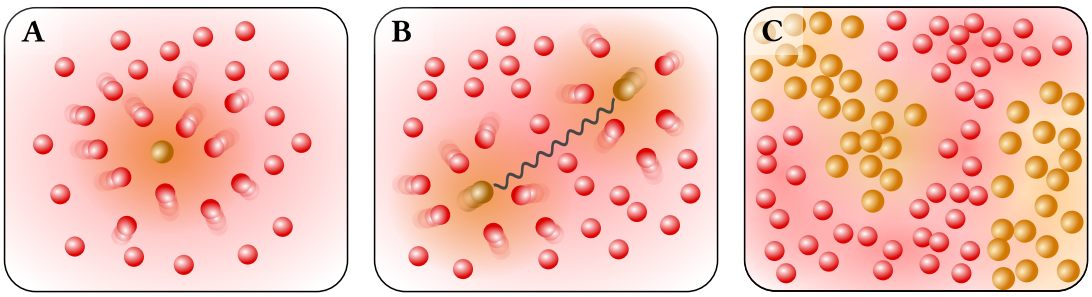

Figure 1.1.: Illustration of polaron and demixing physics. A: Impurity atom dressed by cloud of phononic excitations of a Bose-Einstein condensate, forming the Bose polaron. Figure adapted from [70]. B: Phonon-induced Casimir interaction between two polarons. C: Phase-separation in a population-balanced immiscible mixture.

when describing the transport properties of charge carriers in semiconductors, the Kondo effect in metals [47], or the electron-phonon interactions in high-temperature superconductors [48].

Using a Feshbach resonance to tune the interactions between the impurity and the BEC, recent experiments have been able to explore the strong-coupling regime [49–51]. While the underlying phenomena and characteristics of single isolated Bose polarons are an interesting theoretical challenge [52–59], the medium-induced Casimir-like interaction between two polarons, as shown in figure 1.1 B, has been subject of growing theoretical interest [60–64], as such fluctuation-induced interactions play a significant role in diverse research areas [65–69].

As the concentration of impurity atoms is systematically increased within the strong-coupling regime, where the mixture is immiscible, phase separation ensues, as illustrated in figure 1.1 C.

This thesis details the construction of an experimental platform to investigate the physics of demixing and the role that population imbalance plays in the formation of phase-separated domains.

Specifically, we chose the ultracold atomic mixture of ^{23}Na-^{39}K, as it features favourable scattering properties in the form of wide inter- and intra-species Feshbach resonances at low magnetic fields [71,72]. These resonances facilitate precise tuning of the homo- and hetero-nuclear interaction strength, enabling access to strongly attractive or repulsive regimes. Furthermore, sodium, having been among the first atomic species to be experimentally condensed to quantum degeneracy [2], can be readily cooled and manipulated using standard laser cooling and evaporative cooling techniques to reach

the ultra-low temperatures necessary for BEC formation.
Additionally, potassium has the advantage of possessing multiple stable isotopes, including ^{39}K, ^{40}K, and ^{41}K. ^{39}K, being a bosonic isotope and the focus of this work, can form a BEC, while the less abundant fermionic isotope ^{40}K would enable the investigation of Bose-Fermi mixtures when combined with ^{23}Na. Moreover, the positive s-wave background scattering length of ^{41}K makes it an intriguing system for quantum simulation studies, especially at low magnetic bias fields.

The thesis is organized as follows:

CHAPTER 2 introduces the relevant theoretical foundations, starting with the basics of Bose-Einstein condensation. After discussing the tunablity of interactions through magnetically adjustable Feshbach resonances, the chapter concludes by taking a closer look at the two-component system, which possesses an interesting miscible to immiscible phase transition.

CHAPTER 3 presents a detailed description of the experimental tools that are necessary for such an ultracold mixture machine. This encompasses the optical arrangement of the different laser systems, the design and construction of the magnetic field coils, and the theory and implementation of sophisticated detection methods.

CHAPTER 4 outlines the strategy to achieve sodium degeneracy, highlighting the different laser cooling and evaporation stages on the way to the ^{23}Na Bose-Einstein condensate.

CHAPTER 5 illustrates the challenges we face on our path towards dual-species degeneracy. After discussing the grey molasses cooling stage implemented for potassium, we turn our attention to the optical dipole trap, where the interactions can be tuned using a Feshbach resonance. We explore the rich inter- and intra-species Feshbach spectra, and apply the gained insights to further cool the atomic mixture.

CHAPTER 6 summarizes the main results of this work and gives a brief outlook into the next steps in the experiment.

CHAPTER 2

Theory fundamentals

In this chapter, I will review some key theoretical concepts that are relevant to the work presented in this thesis. I will start in section 2.1 with an introduction to the fundamental theoretical concepts concerning Bose-Einstein condensation. This includes the mean-field description using the Gross-Pitaevskii equation, its solution in the Thomas-Fermi approximation, and the discussion of elementary excitations using Bogoliubov theory.
In section 2.2, I will provide additional theoretical background regarding Feshbach resonances, which are an essential tool to tune the inter- and intra-species scattering properties.
The concepts are extended to the description of a two-component mixture in section 2.3. The interaction between the species gives rise to a set of two coupled Gross-Pitaevskii equations, which will be solved utilizing Bogoliubov theory. The resulting excitation spectrum will be analysed, highlighting an unstable regime that initiates demixing dynamics within the immiscible mixture. Lastly, we will take a closer look at the ^{23}Na-^{39}K scattering properties, relevant for the domain formation in an immiscible mixture.

2.1. Bose-Einstein condensation

Given the extensive body of literature in the form of textbooks [73, 74] and review articles [75, 76], this section serves as a concise summary of key elements related to Bose-Einstein condensation that are relevant to this work.
Starting with a dilute gas of bosons, their statistics are dictated by quantum mechanics once the wave-packets of individual particles begin to overlap. This particular state of matter, referred to as a *Bose-Einstein condensate* (BEC), is formed when the phase-space density exceeds a critical threshold:

$$\rho = n\,\lambda_{\mathrm{dB}}^3 \geq 2.61 \tag{2.1}$$

with the density of the gas n and the thermal de-Broglie wavelength $\lambda_{\mathrm{dB}} = \sqrt{\frac{2\pi\hbar^2}{mk_BT}}$. Hence, in order to satisfy equation 2.1, achieving high densities and low temperatures is required. This experimental challenge will be further addressed in chapters 4 and 5 when attempting to cool sodium and potassium below quantum degeneracy. Upon crossing this threshold, the bosons undergo a phase transition, leading to a macroscopic occupation of the lowest energy ground state and the formation of a macroscopic wave-function, characteristic of a Bose-Einstein condensate.

By treating the interactions between particles of mass m in a mean-field approximation, a non-linear Schrödinger equation for an interacting low-temperature Bose gas can be derived:

$$i\hbar\frac{\partial}{\partial t}\Psi(\mathbf{r},t) = \left[-\frac{\hbar^2}{2m}\nabla^2 + V(\mathbf{r}) + g\,|\Psi(\mathbf{r},t)|^2\right]\Psi(\mathbf{r},t) \tag{2.2}$$

This equation is known as the Gross-Pitaevskii equation [77, 78]. The three terms on the right-hand side correspond to the kinetic energy of the particles, the external trapping potential $V(\mathbf{r})$, and the inter-particle interactions within the system, parametrized by the coupling strength

$$g = \frac{4\pi\hbar^2 a}{m} \tag{2.3}$$

where a is the s-wave scattering length.

In the regime of strong interactions, where the cloud is dense, the Gross-Pitaevskii equation can be solved by neglecting the kinetic energy term, a simplification known as the *Thomas-Fermi approximation*. Within this approximation, the density profile is described by:

$$n(\mathbf{r}) = \frac{\mu - V(\mathbf{r})}{g} \tag{2.4}$$

with the ground state chemical potential μ. The explicit dependence of density on the external potential's shape is a characteristic feature of a degenerate atom cloud. Consequently, within a harmonic trap, the atomic density profile adopts an inverted parabolic shape. The point at which the density reaches zero, defined by $\mu = V(R_{\mathrm{TF}})$, designates the *Thomas-Fermi radius*. Additional information regarding the bimodal density distribution observed for partially condensed atom clouds is presented in appendix B.

Small perturbations on a background condensate can be treated using *Bogoliubov theo-*

ry [79]. In this approximation, owing to the macroscopic occupation of the ground state, the ground state operators are substituted with complex numbers. Additionally, higher-order an-harmonic terms involving multiple creation and annihilation operators are neglected. This leads to a simplified Hamiltonian that can be diagonalized via a linear transformation, yielding the Bogoliubov dispersion law for elementary excitations:

$$\epsilon(p) = \left[\frac{gn}{m}\, p^2 + \left(\frac{p^2}{2m}\right)^2\right]^{1/2} \tag{2.5}$$

In the limit of large p, the quadratic term dominates, as expected for non-interacting single-particle excitations. Conversely, at small momenta, the dispersion relation transforms into a linear form, indicating the presence of collective phononic excitations, often attributed to the system's collective behaviour.

2.2. Scattering theory

Let's consider the collisional process between two particles interacting via a short-ranged potential $V(\mathbf{r})$. As the interaction potential only depends on the relative positions $\mathbf{r} = \mathbf{r}_1 - \mathbf{r}_2$ of the atoms, this elastic scattering problem can be solved in the centre-of-mass frame using the Schrödinger equation:

$$\left[-\frac{\hbar^2}{2m_r}\nabla^2 + V(\mathbf{r})\right]\Psi_{\mathbf{k}}(\mathbf{r}) = E_{\mathbf{k}}\Psi_{\mathbf{k}}(\mathbf{r}) \tag{2.6}$$

with the reduced mass m_r. For a short-ranged potential, the scattered state can be described by the superposition of an incoming plane wave and an outgoing scattered spherical wave

$$\Psi_{\mathbf{k}}(\mathbf{r}) \propto e^{i\mathbf{kr}} + f(k,\theta)\,\frac{e^{i\mathbf{kr}}}{\mathbf{r}} \tag{2.7}$$

where the scattering amplitude $f(k,\theta)$ connects to relevant physical quantities such as the scattering cross section.

For a radially symmetric potential $V(\mathbf{r}) = V(r)$, the wave function can be expanded with respect to the angular momentum l into partial waves:

$$\Psi_{\mathbf{k}}(\mathbf{r}) = \sum_{l=0}^{\infty} P_l(\cos\theta)\frac{u_{k,l}(r)}{r} \tag{2.8}$$

where P_l are the Legendre polynomials and the functions $u_{k,l}(r)$ satisfy the radial Schrödinger equation:

$$\left[-\frac{\hbar^2}{2m_r}\frac{d^2}{dr^2} + V(r) + \frac{\hbar^2\, l(l+1)}{2m_r r^2} \right] u_{k,l}(r) = E_{\mathbf{k}} u_{k,l}(r) \tag{2.9}$$

In the context of partial waves with non-zero angular momentum $l \neq 0$, the centrifugal term acts as a potential barrier for the scattered particles. In the limit of low temperatures, as the wave vector k approaches zero, the collision energy becomes lower than the potential barrier. Consequently, the particles are unable to perceive the interaction potential. Therefore, when describing collisional processes in ultracold atomic gases only s-wave scattering ($l = 0$) will notably contribute. In this regime of extremely low temperatures, the interaction potential can be accurately characterized by a single parameter, namely the s-wave scattering length:

$$a = -\lim_{k\to\infty} \frac{\tan\delta_0(k)}{k} \tag{2.10}$$

where $\delta_0(k)$ is the phase shift of the outgoing spherical wave. This quantity plays a crucial role in the description of *Feshbach resonances* in ultracold weakly interacting gases [7, 73].

To motivate the underlying physics of Feshbach resonances, let's consider a scattering event involving two particles, as depicted by the potential curves in the left graph of figure 2.1. For large separations between the scattered particles, the inter-atomic potential, visualized by the solid black line, serves as an energetically accessible scattering channel, commonly referred to as an open or entrance channel. Additionally, there exist scattering potentials, indicated by the solid blue line, with higher asymptotic energies, which are referred to as closed channels. These closed channels can support bound states with an energy close to the energy of the free atoms in the open channel.
When the corresponding magnetic moments differ due to distinct spin configurations, the presence of an external magnetic field can modify the energy difference between the open channel and the closed channel bound state. This magnetic field dependence is shown in the top-right plot of figure 2.1.
In case of a small coupling between the two channels, the resulting channel mixing can drastically alter the scattering length, as illustrated in the bottom right graph of figure 2.1. If the bound state becomes degenerate with the asymptotic energy of the

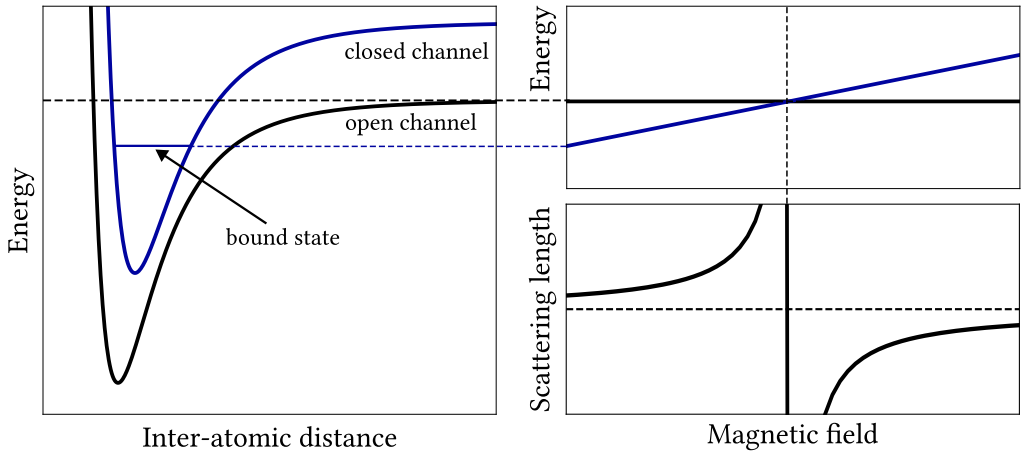

Figure 2.1.: Schematic illustrating the principle of a Feshbach resonance. Two colliding atoms in the open channel couple to the bound state of a closed channel. This coupling occurs when the threshold energy of the open channel is equal to the closed channel bound state energy and leads to a resonance feature (Feshbach resonance) in the scattering length. Due to differing magnetic moments, the two channels shift energetically with respect to each other as a function of magnetic field, enabling tunability of the scattering length across the resonance. Figure adapted from [80].

open channel at a certain magnetic field B_0, the scattering length diverges. Close to this resonance, the scattering length, as a function of the external magnetic field B, is given by

$$a(B) = a_{\mathrm{bg}}\left(1 - \frac{\Delta}{B - B_0}\right) \tag{2.11}$$

where Δ is the width of the resonance, and the background scattering length in the open channel is defined as a_{bg}. Consequently, interactions can be tuned to be attractive (negative scattering length) when the bound state is energetically shifted above the open channel threshold or repulsive (positive scattering length) in the opposite scenario, with the external magnetic field serving as the tuning parameter.

The feasibility of freely adjusting interactions using these magnetically tunable Feshbach resonances was first demonstrated in 1998 [5], utilizing an optically trapped Bose–Einstein condensate of sodium atoms. Naturally, these concepts can be extended to mixtures of different atomic species, enabling the manipulation of inter-species interactions. In the experiment, we can use these resonances as a tool to reach dual-species degeneracy, as further discussed in chapter 5, and as tuning knob to probe the miscible-immiscible phase transition, which will be motivated in the following section.

2.3. Two-species mixtures

In a mixture system, composed of two distinct bosonic species, we encounter three distinct parameters characterizing the interactions. The intra-species interactions within each component are parametrized by g_{11} and g_{22}, while the inter-species interaction strength is denoted by g_{12}. Employing separate wave functions to describe each condensate [81], we can formulate the coupled Gross-Pitaevskii equations for this system:

$$i\hbar\frac{\partial}{\partial t}\Psi_1 = \left[-\frac{\hbar^2}{2m_1}\nabla^2 + V_1(\mathbf{r}) + g_{11}|\Psi_1|^2 + g_{12}|\Psi_2|^2\right]\Psi_1 \tag{2.12}$$

$$i\hbar\frac{\partial}{\partial t}\Psi_2 = \left[-\frac{\hbar^2}{2m_2}\nabla^2 + V_2(\mathbf{r}) + g_{22}|\Psi_2|^2 + g_{12}|\Psi_1|^2\right]\Psi_2 \tag{2.13}$$

where the coupling constants are determined by the scattering lengths according to:

$$g_{11} = \frac{4\pi\hbar^2 a_{11}}{m_1}, \quad g_{22} = \frac{4\pi\hbar^2 a_{22}}{m_2} \quad \text{and} \quad g_{12} = \frac{2\pi\hbar^2 a_{12}}{m_r} \tag{2.14}$$

with the reduced mass of the mixture $m_r = m_1 m_2/(m_1 + m_2)$.

Equilibrium properties

Let us first examine a homogeneous system confined within a box potential of fixed volume V, where the atomic densities $n_i = |\Psi_i|^2 = \frac{N_i}{V}$ remain constant. The equilibrium ground state of this system is either a uniform mixture, where the two species spatially overlap, or a phase separated inhomogeneous one, with the two components occupying different regions of volumes V_i. The energy of the system in these two configurations is given by [73, 82, 83]

$$E_{\text{unif}} = \frac{1}{2}\left[g_{11}\frac{N_1^2}{V} + g_{22}\frac{N_2^2}{V} + 2g_{12}\frac{N_1 N_2}{V}\right] \tag{2.15}$$

$$E_{\text{sep}} = \frac{1}{2}\left[g_{11}\frac{N_1^2}{V_1} + g_{22}\frac{N_2^2}{V_2}\right] = \frac{1}{2}\left[g_{11}\frac{N_1^2}{V} + g_{22}\frac{N_2^2}{V} + 2\sqrt{g_{11}g_{22}}\frac{N_1 N_2}{V}\right] \tag{2.16}$$

Consequently, for the system to phase separate ($E_{\text{unif}} > E_{\text{sep}}$), the following condition must be fulfilled

$$g_{12} > \sqrt{g_{11}\,g_{22}} \quad \Longleftrightarrow \quad \delta g \coloneqq \frac{g_{12}^2}{g_{11}\,g_{22}} - 1 > 0 \tag{2.17}$$

where we have defined the miscibility parameter δg, that characterizes the transition between a miscible and an immiscible mixture.
Note that the conditions $\delta g > 0$ and $g_{12} < 0$ will lead to the mean-field collapse of the system, meaning that phase-separation requires repulsive inter-species interactions ($g_{12} > 0$). Beyond mean-field effects become relevant when the attractive inter-species interaction is small and balances the repulsive interactions within each species, leading to the formation of so-called *quantum droplets* [84–87].

Collective excitations

Having analysed the equilibrium properties of the ground state of a two-component mixture in the prior section, our focus now shifts towards investigating elementary excitations within the system. For simplicity, we examine a homogeneous system using Bogoliubov treatment, as outlined in [42, 74, 88]. The system's two collective excitation branches are given by

$$\Omega_{\pm}^2(k) = \frac{\omega_1^2 + \omega_2^2}{2} \pm \frac{1}{2}\sqrt{\left(\omega_1^2 - \omega_2^2\right)^2 + 4g_{12}^2 n_1^0 n_2^0 \frac{k^4}{m_1 m_2}} \tag{2.18}$$

with the single-component Bogoliubov dispersion relation $\hbar^2\omega_i^2 = \frac{\hbar^2k^2}{2m_i}\left(\frac{\hbar^2k^2}{2m_i} + 2g_{ii}n_i^0\right)$ and the condensate density n_i^0 for species i. This Bogoliubov spectrum with its two excitation branches is visualized in figure 2.2.
In the non-interacting case, where $g_{12} = 0$, we get

$$\Omega_{1,2}^2(k) = \frac{k^2}{2m_{1,2}}\left(\frac{\hbar^2k^2}{2m_{1,2}} + 2g_{11,22}n_{1,2}^0\right) \tag{2.19}$$

which is the regular Bogoliubov dispersion relation for two separate condensates as introduced in equation 2.5.

In the interacting scenario, where $g_{12} \neq 0$, the excitations within the system become coupled, resulting in the emergence of hybridized excitation branches denoted as $\Omega_{\pm}(k)$. Upon increasing the interaction strength to $g_{12} = \sqrt{g_{11}g_{22}}$, the low-momentum part of Ω_{-} approaches zero and eventually becomes imaginary. This occurs upon entering the immiscible regime, where $g_{12} > \sqrt{g_{11}g_{22}}$, as shown in figure 2.2 B. Consequently, the homogeneous system becomes unstable with even weak perturbations on the background leading to an exponential growth of long-wavelength modes, culminating in the demixing of the two species [46].

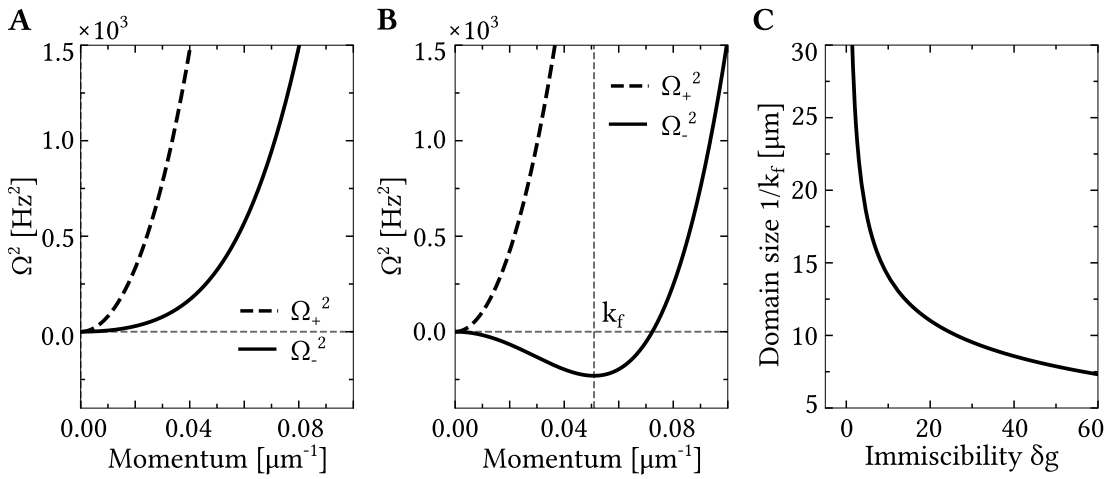

Figure 2.2.: Bogoliubov spectra for a two-species mixture. A: The two excitation branches for a miscible mixture with $\delta g = -0.9$. B: Bogoliubov spectrum for an immiscible mixture with $\delta g = 4.0$. The Ω_-^2 branch goes below zero, leading to demixing and has a minimum at a momentum k_f. C: Domain size $1/k_f$ as a function of the miscibility parameter δg.

The fastest growing modes, which are determined by the minimum of $\Omega_-^2(k)$, have wavenumber k_f and grow at a rate $\tau = 1/|\Omega_-(k_f)|$. These quantities provide an estimate for the length and time scale of domain formation [36, 88].

Furthermore, as the inter-species interaction strength and, consequently, the miscibility parameter δg are further increased, the minimum at k_f shifts towards higher momenta, leading to the formation of smaller domains. This behaviour is illustrated in figure 2.2 C, where we plotted the domain size $1/k_f$ as a function of δg, highlighting the significant reduction in domain size as the mixture becomes increasingly immiscible.

The formation of domains and their subsequent coarsening during time evolution is illustrated in figure 2.3, where we have numerically simulated the behaviour of the local density of one of the components $n_1(x, y) = |\Psi_1(x, y)|^2$ as a function of time. Initializing both components to be randomly distributed in two dimensions, the interaction strength is quenched to a miscible ($\delta g < 0$) or an immiscible ($\delta g > 0$) state at $t = 0\,\mathrm{s}$. For a miscible mixture, the two components are spread out evenly, and the time evolution does not show any significant features.

Conversely, the immiscible mixture shows the formation of small-sized domains that coarsen as a function of time. This phenomenon is a manifestation of the demixing process within the system.

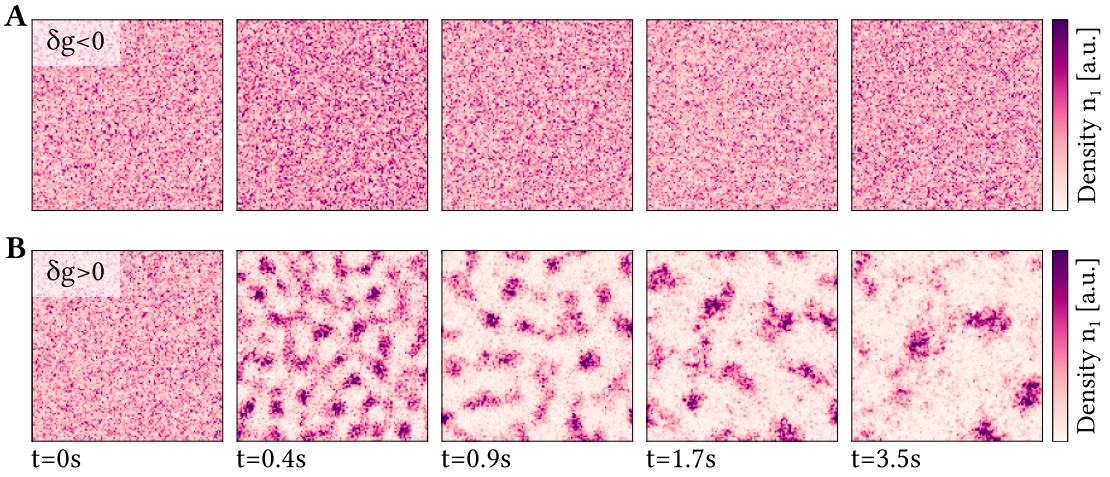

Figure 2.3.: Time evolution of the local density of one component $n_1(x, y) = |\Psi_1(x, y)|^2$ for a miscible (A) and an immiscible mixture (B) localized in two dimensions. The immiscible scenario, where $\delta g > 0$, illustrates the formation of domains and their coarsening dynamics.

Population imbalanced mixture

Up to this point, we have maintained a global zero atom number imbalance $z = \frac{N_{Na}-N_K}{N_{Na}+N_K} = 0$, assuming an equal population of the two clouds. In the experiment, adjusting the atom number ratio is achievable through the initial loading time in the magneto-optical trap (MOT). However, even minor shot-to-shot fluctuations in the initial atom numbers can propagate through the entire evaporative cooling sequence, significantly affecting the final population imbalance.

The influence of a density imbalance on the domain formation can be qualitatively understood by examining the overlap between the two clouds [36]. In an imbalanced mixture, the overlap diminishes, resulting in a reduced effective inter-species interaction strength. This affects the wavenumber of the most rapidly growing modes, shifting them towards smaller momenta. Consequently, the domains will be larger and exhibit slower growth as the imbalance increases.
This behaviour is quantitatively reproduced in figure 2.4, where we plot the unstable mode of the Bogoliubov spectrum, according to equation 2.18, as a function of the population imbalance. Indeed, the minimum of the spectrum (grey lines), i.e. the most rapidly growing unstable mode, shifts to lower momentum for increasing imbalance z.

Very large density imbalances pave the way to investigate the interactions of single impurities interacting with a BEC, giving rise to the formation of so-called *Bose po-*

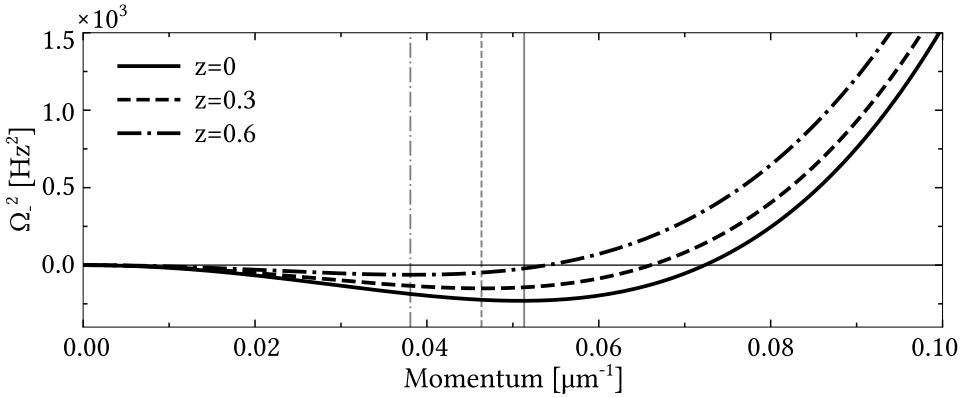

Figure 2.4.: Bogoliubov spectra for a two-species mixture for different population imbalances z. The most unstable mode, indicated by the grey lines, shifts to lower momenta for increasing imbalance.

larons. These quasi-particles possess significantly modified properties compared to the bare impurity atoms, including an effective mass and modifications to the spectral properties. An intriguing phenomenon emerges when immersing two impurities in a Bose-Einstein condensate. The polarons experience a long-range Casimir-like interaction [60–64], scaling as $1/r^3$ for large impurity separations r in the one-dimensional case.

Furthermore, the demixing instability can also be characterized within a strongly population imbalanced two-dimensional binary mixture, where the bath fills the entire space, and the minority species is restricted to a few atoms. In the immiscible regime, the minority species can, under particular conditions, form a localized wave packet, corresponding to the *Townes soliton* state [89, 90].

External trapping potential

In the experiment, the BECs do not exhibit perfect homogeneity but instead display an inhomogeneous density distribution resulting from an external trapping potential. In the presence of such a trapping potential, the density distributions for the two atomic species further depend on the intra-species interaction strength - an effect referred to as *buoyancy* [81, 88, 91]. In a buoyant mixture, the component with the lower intra-species interaction strength tends to localize in the central region of the trap, where higher atomic densities are present. This localization occurs as a means to minimize the system's energy. Conversely, the component with the stronger intra-species interactions tends to be constrained to the edges of the trap. It is important to note that this phenomenon is observed in both miscible and immiscible systems. To mitigate

this effect, the intra-species coupling strengths have to be tuned to be of similar magnitude, or a box-like uniform confinement has to be implemented.

Additionally, in the context of a mass-imbalanced mixture involving ^{23}Na-^{39}K, a differential gravitational sag will come into play. This gravitational effect, elaborated upon in section 5.3, diminishes the spatial overlap between the two species.

In a study by Gutierrez et al. [92], the influence of gravity and atom number ratio on a mass-imbalanced mixture was explored. The atom number ratio $\eta = N_{\mathrm{Na}}/N_{\mathrm{K}}$ was varied by adjusting the number of atoms in the minority species ^{39}K. The spatial overlap of the two atomic clouds served as a quantitative metric to evaluate the miscibility of the mixture. Figure 2.5 A presents the spatial overlap between the two clouds as a function of magnetic field and atom number ratio. A system is considered miscible when there is a significant spatial overlap, while deeply immiscible mixtures approach zero overlap. While the phase transition from miscible to immiscible mixture occurs at 109.1 G for a homogeneous system, the transition point shifts when accounting for an external potential. This dependence on the external trapping conditions is, furthermore, illustrated in figure 2.5 B, where the spatial overlap is plotted versus the magnetic field for different trapping parameters. Compared to the homogeneous case with no gravitational potential, the presence of different trapping potentials ϑ_i and the

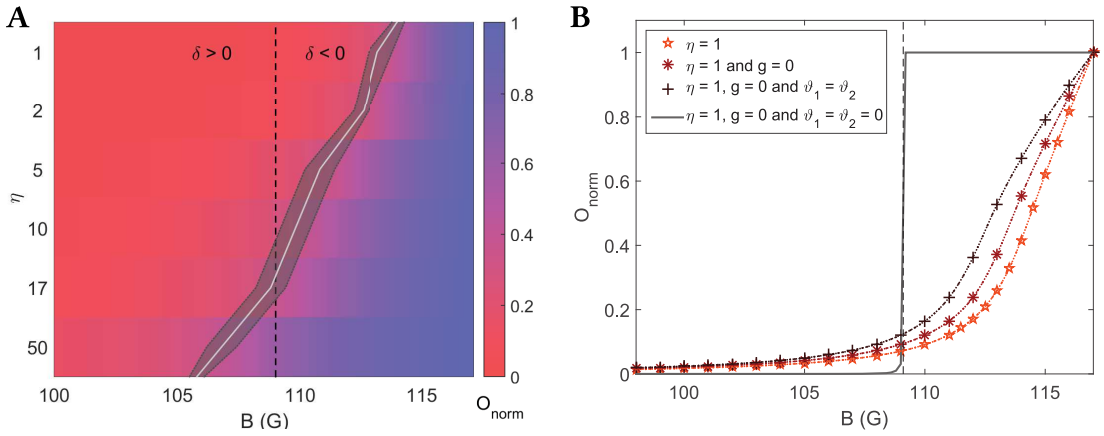

Figure 2.5.: Dependence of the overlap of the ^{23}Na-^{39}K mixture on different experimental parameters. A: Normalized spatial overlap as a function of the atom number ratio η and bias magnetic field B. The miscible to immiscible phase transition for a homogeneous system is represented by the white line. B: Spatial overlap of the two clouds for a fixed η and different trapping conditions (trapping potentials denoted by ϑ_i). Figures taken from [92].

effect of gravity $g \neq 0$ shifts the phase transition to higher magnetic fields.[1]

The quantitative characteristics of this phase transition are significantly reliant on the specific parameters of each individual experiment, such as the trapping frequencies. Nonetheless, this example provides valuable qualitative insights, emphasizing the necessity of considering both the external trapping potential and gravitational potential when determining the transition point from a miscible to an immiscible mixture. The miscibility parameter δg loses its validity as an indicator, given that the phase transition is notably influenced by the atom number ratio η and the external trapping parameters [92, 93].

Experimental properties

Ultracold atomic mixture experiments provide a clean and versatile platform to study the physics of demixing, as inter-species Feshbach resonances enable fine-tuning of interaction strengths using an external magnetic bias field. In the context of the ^{23}Na-^{39}K mixture, the scattering properties of the individual constituents have been extensively characterized:

SODIUM:

- First observation of a Feshbach resonance for the $|1,-1\rangle^2$ state by Stenger et al. [94] at a magnetic bias field of approximately 1195 G.
- Further narrow s-, d-, and g-wave resonances reported by Knoop et al. [95], while confirming no significant features at low magnetic fields. The background scattering length was calculated to be $54.54(20)\,a_0$.

POTASSIUM:

- D'Errico et al. [96] discovered magnetically tunable Feshbach resonances for the different $|F = 1\rangle$ Zeeman sub-levels in potassium 39.
- Comprehensive study of Feshbach resonances in potassium Bose-Bose mixtures ^{39}K-^{41}K, including a characterization of the resonance parameters by Tanzi et al. [97].
- Utilizing a combination of bound-state spectroscopy and atom-loss spectroscopy, Etrych et al. [98] measured several $|F = 1\rangle$ interstate resonances

[1] The difference between the bottom two cases in figure 2.5 B stems from differing intra-species interaction strengths and the resulting buoyancy effect described above.
[2] In this thesis, we use the notation $|F, m_F\rangle$ unless otherwise specified.

with a high level of precision. For the $|1,-1\rangle$ spin state, three resonances were located at 33.5820(14) G, 162.36(2) G and 561.14(2) G.

Sodium-potassium mixture:

- Viel et al. [99] carried out a theoretical study of Feshbach resonances for various isotopic Na-K pairs, namely Na-^{39}K, Na-^{40}K, and Na-^{41}K.
- Schulze et al. [71, 100] performed Feshbach spectroscopy measurements for ensembles in the $|1,-1\rangle$ spin state, locating inter-species resonances at 32.5(8) G and 247.1(2) G, with a zero-crossing at 117.2(2) G.
- Hartmann et al. [72, 101] conducted a detailed study of Feshbach resonances for various hyperfine spin combinations up to 750 G. Their work also included refined singlet and triplet ground state potentials of Na-K.

With this information at hand, the magnetic field region $40-160$ G, between the two potassium low-field resonances, offers both miscible and highly immiscible regimes when focusing on ensembles in the $|1,-1\rangle$ spin state. Implementing a quench from a miscible to an immiscible system requires either a rapid magnetic field ramp or a spin flip. Such a quench would then initiate the demixing dynamics, where the domain formation could be subsequently resolved using individual imaging schemes for the two atomic species.

Conclusion

At ultracold temperatures, the phase-space density of an atomic sample can exceed a critical threshold, resulting in the macroscopic occupation of the quantum mechanical ground state — a state known as a Bose-Einstein condensate (BEC). The mean-field description of this state can be effectively captured by the Gross-Pitaevskii equation, solvable in the Thomas-Fermi approximation, which involves neglecting the kinetic energy of the constituent atoms.
In the case of a two-species system, a set of coupled Gross-Pitaevskii equations offers an accurate representation. The system's behaviour — whether it tends towards miscibility or immiscibility — is contingent upon the strengths of intra- and inter-species interactions. To analyse the emergent instabilities in a homogeneous system, a Bogoliubov treatment has been applied, yielding estimations for the length scale $1/k_f$ and growth rate $\tau = 1/|\Omega_-(k_f)|$ of the emerging domains, where k_f is the wavenumber of the fastest growing unstable modes.

The modulation of inter- and intra-species interaction strengths is achievable through magnetically tunable Feshbach resonances. By adjusting the magnetic field across a resonance, the s-wave scattering length a can be adjusted to be strongly attractive or repulsive. This capability proves especially valuable when investigating domain formation through a controlled transition from a miscible to an immiscible mixture. Moreover, this tunability proves advantageous for the dual-species cooling process, where ensuring a substantial overlap between the two atomic clouds is imperative to facilitate effective sympathetic cooling.

CHAPTER 3

Experimental tools

Having introduced the necessary theoretical tools, we can focus on the experimental setup of our atomic mixture machine. Figure 3.1 displays a three-dimensional view of the vacuum system. The initial pre-cooling of sodium and potassium atoms occurs within two distinct two-dimensional magneto-optical traps (2D-MOTs). Subsequently, near-resonant push beams facilitate the transfer of atoms from their respective 2D-MOT chamber into the dual-species science chamber. Within this chamber, the atoms are further confined and cooled, which is the subject of chapters 4 and 5. In this chapter, I will focus on the experimental tools imperative for achieving quantum degeneracy with our sodium-potassium atomic mixture.

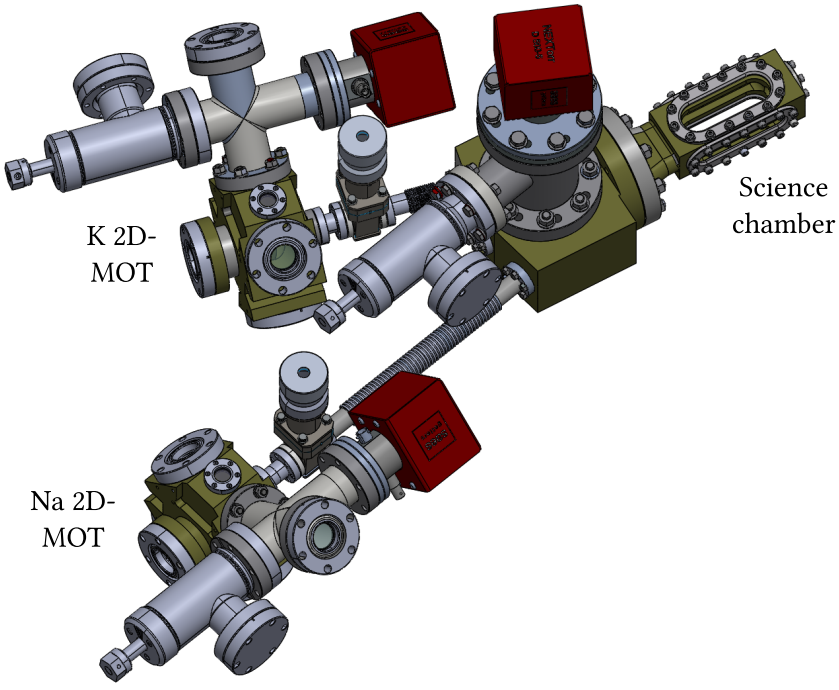

Figure 3.1.: Three-dimensional view of the vacuum system. The two independent two-dimensional magneto-optical traps (2D-MOTs) serve as a source of cold atoms for the subsequent cooling stages, which take place in the dual-species science chamber. The different chambers, which can be isolated from each other via gate valves, are pumped down using ion-getter pumps (*SAES NEXTorr Z100/D500*).

After discussing significant modifications and enhancements to the experiment in section 3.1, attention will be directed towards a detailed account of the two laser systems dedicated to sodium and potassium in section 3.2. In section 3.3, I will present the design, fabrication and characterization of the magnetic field coils. These coils are instrumental in generating magnetic field gradients and bias magnetic fields during the experimental sequence. Finally, in section 3.4, a thorough description and characterization of the absorption imaging method employed in the experiment will be provided.

3.1. Disruptive transformation of our mixtures lab

In the spring of 2022, important and difficult decisions had to be made regarding the experimental setup. Up to this point, the laboratory space was shared with a sodium-lithium (NaLi) mixture machine [102–105], imposing substantial spatial constraints. In our sodium-potassium (SoPa) experiment, both sodium and potassium atoms were loaded into a dual-species Magneto-Optical Trap (MOT), where we had studied the stochastic dynamics of few sodium atoms immersed in a potassium MOT using atom counting techniques [106, 107]. However, we encountered challenges in condensing sodium atoms, a crucial initial step in working with a dual-species apparatus, as sodium is supposed to act as a sympathetic coolant for the potassium atoms. We attributed these difficulties to limitations of our magnetic field coils, which had inadequate water-cooling, and issues with the implemented absorption imaging system. Additionally, during the evaporation stages, the atomic densities were insufficient to enter the runaway regime, thus impeding effective cooling.

As the NaLi-experiment reached the end of its lifetime due to persistent vacuum issues, we decided to dismantle the sodium-lithium apparatus and reorganize the laboratory space. With the additional available space, each species was assigned a dedicated optical table measuring 3 m × 1.5 m, providing a stable base for assembling the laser systems, as opposed to the previous configuration of two stacked optical breadboards. More space and easier access allowed for a better arrangement of optics and eased the optimization of acousto-optical modulator (AOM) alignments and fibre coupling efficiencies. Moreover, the optics and the laser from the previous setup were repurposed, providing an extra 1 W of sodium laser light to work with.

Substantial updates were also implemented on the experiment table. To enhance stor-

age capacity above and below the optical table and ensure laser safety, an enclosure made of *Item* aluminium profiles was built around the optical table. A laser curtain going around the side of this construction ensures laser safety for low-power stray light. The high-power dipole laser setup requires additional 3 mm thick anodized aluminium boxes, as this beam could otherwise burn a hole into the black curtain.

The top of the frame is closed with wooden multiplex boards and four flow boxes, establishing a ventilation system that provides a laminar flow of clean air. This airflow mechanism minimizes dust accumulation on the optics. The wooden boards also serve as a platform for organizing the wiring of the magnetic field coil connections. Two passbanks for fast current control and an H-bridge for switching the current direction through one coil are placed on top of these boards. Cables and optical fibres are guided through holes drilled into the multiplex boards.

Additionally, we replaced the previous coil design, which was limited to gradients below 150 G/cm due to inadequate water cooling. The new design employed coils wound from hollow-core wire, featuring efficient water cooling and thus permitting higher gradients. Furthermore, we changed the orientation of the coils from a side configuration to a top-bottom configuration, making it possible to keep most of the MOT optics on one common breadboard in the horizontal plane. For both the 2D- and 3D-MOT, the retro-reflected setup was replaced with independent beams along each direction,

Figure 3.2.: Sequence of images before, during and after the lab transformation.

leading to an improved alignment and beam balancing, which is particularly crucial during the sub-Doppler cooling stage.

These modifications and enhancements to the experimental setup have proven to be effective and fruitful, evidenced by the successful achievement of a sodium Bose-Einstein condensate (BEC) and the promising outlook for achieving dual-species degeneracy within a year of this disruptive transformation.

3.2. Laser systems

The experimental setup comprises one optical laser table for each species. On these tables, the near-resonant light for the magneto-optical traps and for imaging is frequency-stabilized, amplified, and appropriately shifted to achieve the desired frequency. Figure 3.3 illustrates the respective energy level schemes for ^{23}Na (A) and ^{39}K (B), where the cooling and repumping transitions are indicated by arrows. While only the D2-line is used to cool and address sodium, for potassium, both the D2- and D1-line will be of importance.

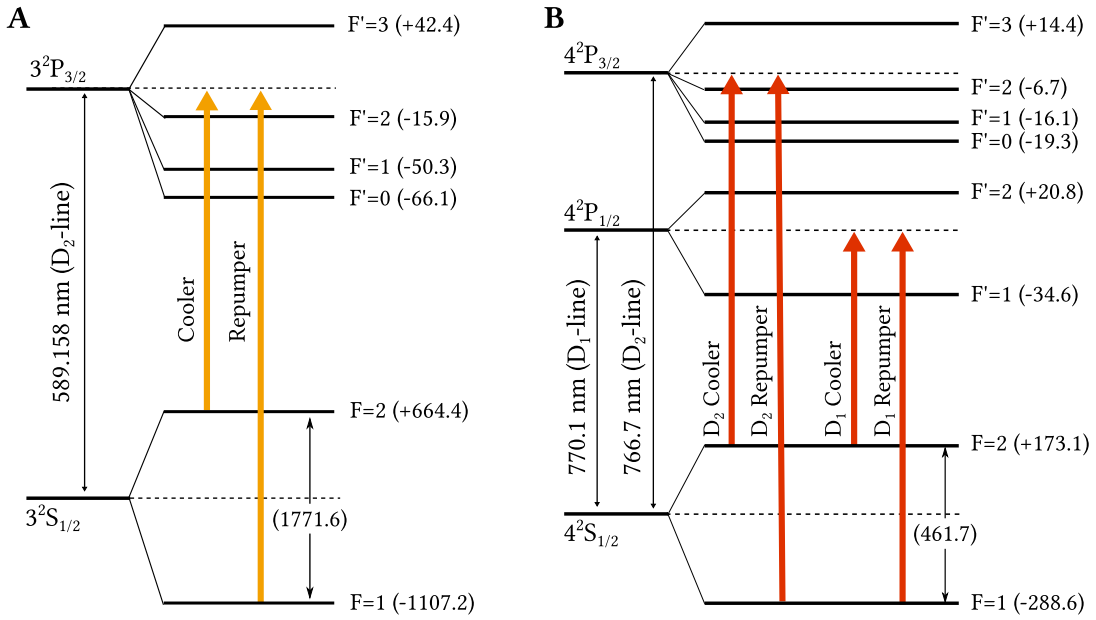

Figure 3.3.: Energy level schemes for ^{23}Na (A) and ^{39}K (B). The cooling and repumping transitions are marked by the respective arrows. While we only use the D2-line for cooling sodium, we utilize the potassium D1-line for grey molasses cooling. The hyperfine frequency shifts are displayed in brackets in units of MHz. Values are taken from [108] for ^{23}Na and [109] for ^{39}K.

3.2.1. Sodium laser table

The sodium laser system operates in a leader-follower configuration, necessitating two lasers. The leader-laser is frequency-stabilized to an atomic reference using saturated absorption spectroscopy [110, 111]. The follower-laser is then locked to this reference utilizing an offset beat lock method [112].
Both sodium lasers are frequency-doubled diode lasers[1] that involve amplifying light with a wavelength of 1178 nm from an external cavity diode laser and then frequency-doubling it within a second-harmonic-generation (SHG) cavity. This procedure yields a laser output of approximately 1.4 W of 589 nm light. Motorized in-coupling mirrors for the tapered amplifier and the SHG-cavity allow for an optimization routine, enabling automated alignment for optimal output power. Typically, this optimization routine is performed approximately once a week for standard operation.

Frequency stabilization

The output of the leader-laser is locked to an atomic reference by coupling a small fraction of light into a sodium spectroscopy cell. At room temperature, the vapour pressure, and thus the absorption rate for sodium, is too low. Therefore, the spectroscopy cell is heated to 180 °C. We experienced some issues with heating the spectroscopy cell as the current flowing through the heaters induced a magnetic field, disturbing the spectroscopy signal by causing energy level shifts due to the Zeeman effect. This problem was resolved by exchanging the heaters with alternative ones[2].
The saturated absorption spectrum yields an error signal by modulating the magnetic field within the spectroscopy cell. This modulation is achieved by supplying a sinusoidally varying current to a magnetic field coil wrapped around the spectroscopy cell, a technique known as Zeeman modulation locking [113]. Using this error signal, we lock the leader-laser to the D2 ground state crossover (CO), as illustrated in figure 3.4 A. The spectrum in the top graph shows three discernible features. From left to right, these correspond to transitions from $|F = 1, 2\rangle$ (CO) to $|F' = 2\rangle$, $|F' = 2, 3\rangle$ (CO) and $|F' = 3\rangle$. The central zero-crossing of the error signal marks the lock point, as indicated by the vertical dashed grey line.

The follower-laser is locked to the leader with a variable offset using an offset beat lock. This involves overlapping light from both lasers on a fast photodiode. A delay

[1] TOPTICA Photonics TA-SHG Pro
[2] Watlow MB1J1JN3-B12 were replaced by Acim Jouanin L3420C9A5.

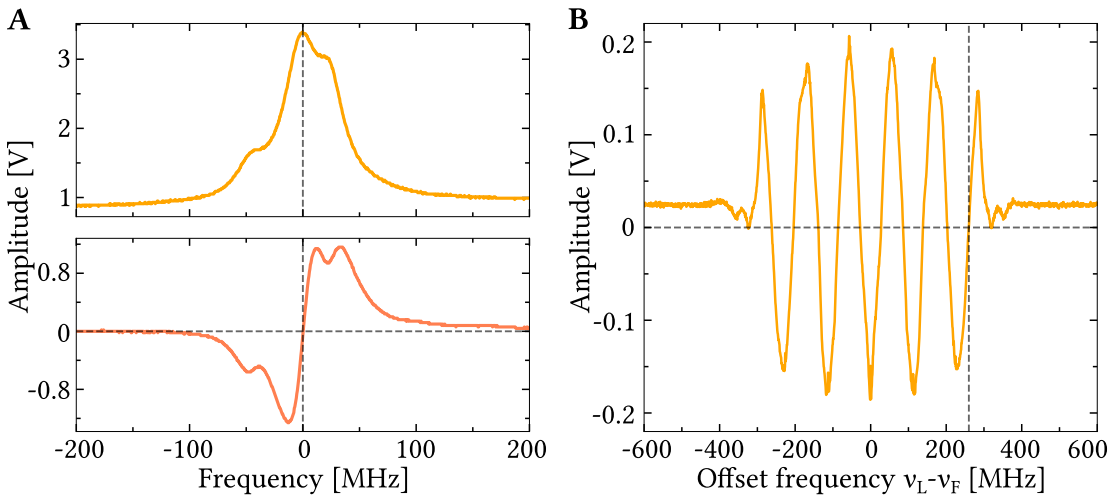

Figure 3.4.: ^{23}Na laser locking signals. A: Saturated absorption spectroscopy of the D2 ground state crossover line with the generated error signal below (dark orange curve). B: Error signal of the offset beat lock to frequency-stabilize the follower-laser. The frequencies of the leader- and follower-laser are denoted by ν_L and ν_F, respectively. The lock-points for the two lasers are indicated by grey dashed lines.

line introduces a frequency-dependent phase shift, generating an error signal that can be used to stabilize the follower-laser. Further details regarding this lock can be found in [114]. Figure 3.4 B illustrates the error signal from the offset lock, where the x-axis represents the frequency offset of the follower-laser relative to the leader-laser. The lock-point at 260 MHz is set to the zero-crossing of the last rising slope, indicated by the intersection of the dashed grey lines.

Frequency shifting

The stabilized laser output is divided into multiple beams and subjected to frequency shifting, as shown schematically in figure 3.5. Additionally, figure 3.6 provides an image depicting the assembled setup on the optical table.
The leader-laser supplies the light for the 2D-MOT, imaging, push, repumper and 3D-MOT cooler. The light is divided into these respective paths using half wave-plates and polarizing beam-splitters (PBS). To accomplish frequency shifting, acousto-optical modulators (AOMs) are employed in a double-pass configuration [115]. For each AOM path a 3:1 telescope, consisting of a convex ($f = 150$ mm) and a concave ($f = -50$ mm) lens, reduces the beam diameter to match the optical aperture of the AOM. Using a retro-reflecting mirror, the beam is passed twice through the AOM, ensuring that the doubly diffracted order is superimposed with the input. Incorporating a cat's eye lens

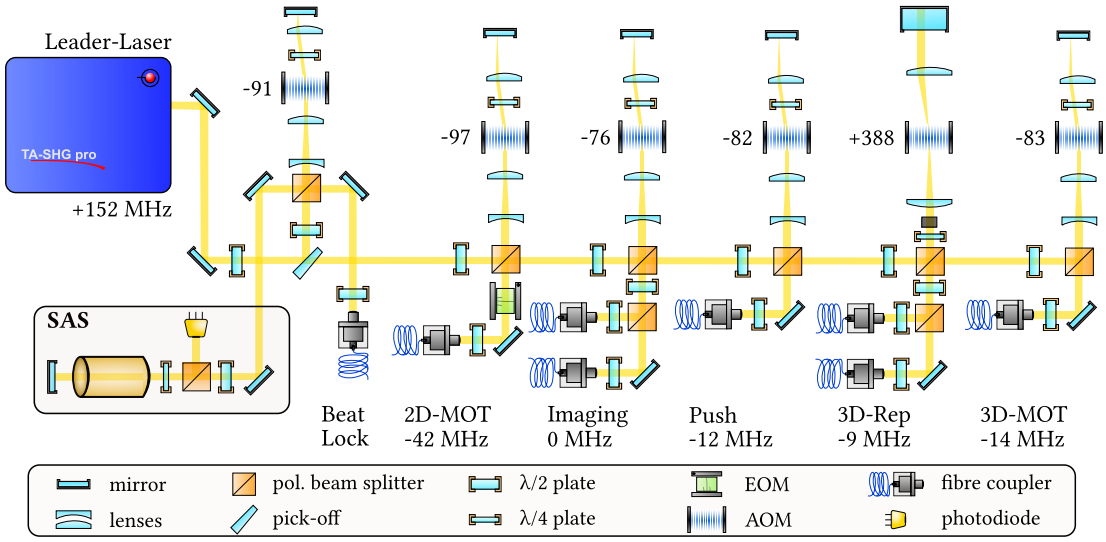

Figure 3.5.: Schematic of the sodium leader-laser system. The light is frequency-stabilized with a saturated absorption spectroscopy (SAS), and then split and frequency-shifted using acousto-optical modulators (AOMs). The corresponding AOM RF-frequencies for the different paths are displayed in MHz. The laser beams are eventually coupled into single-mode optical fibres that transport the light to the experiment.

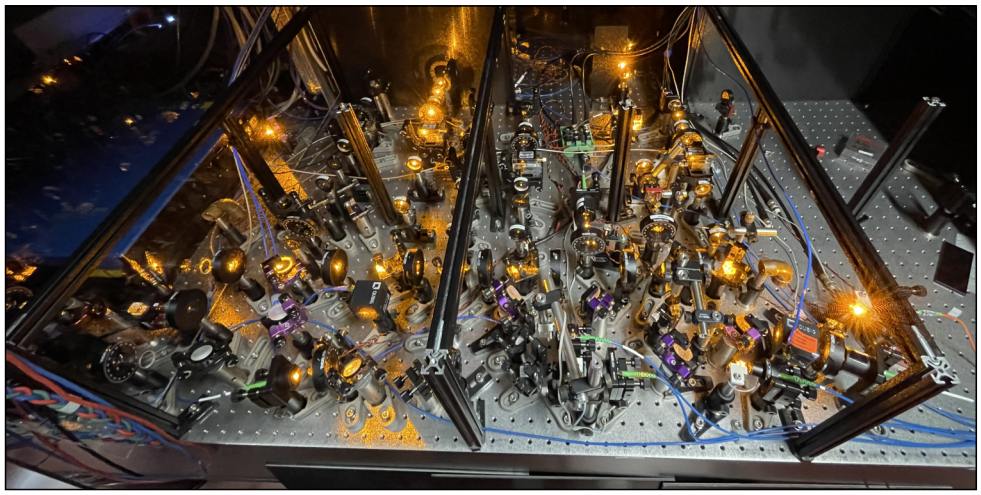

Figure 3.6.: Image of the sodium leader-laser system. The light from the sodium laser on the left is split up and frequency-shifted in AOM double-/quadruple-passes. The light is then coupled into optical fibres, which are bunched in the bottom right, and transported to the main experiment table.

($f = 75\,\text{mm}$) in the setup renders the alignment of the frequency-shifted beam independent of the applied RF-frequency. Consequently, fibre coupling is preserved when tuning the AOM frequency for optimization purposes. Subsequently, the frequency-shifted light is coupled into single-mode polarization-maintaining optical fibres. A dedicated half-wave plate ensures polarization-maintaining coupling.

The output of the leader-laser is stabilized to a point +152 MHz detuned with respect to the cooling transition by shifting the light with an AOM double pass before directing it to the saturated absorption spectroscopy setup. The frequencies of the other beams are then adjusted with respect to this reference using the respective AOM paths. All sodium laser frequencies and power values are summarized in table 3.1. The power for each path was measured behind the fibre out-coupler on the experiment table.

Lastly, each laser beam path features a mechanical shutter located in front of the optical fibre. This shutter is employed to permanently block the respective beam, ensuring no stray light and allowing to switch the AOM back on once the shutter is closed. For most laser beams, we use a razor blade affixed to an electromagnetic relay that moves the blade into and out of the laser beam depending on the applied TTL voltage, achieving switching times of a few ms. For the low-power imaging beam, a faster

Table 3.1.: Frequency detunings and power values for the different sodium laser beam paths. The frequency detuning is given with respect to the transition denoted in the second column. The power was measured after the fibre out-coupler on the experiment table.

	Transition $\|F\rangle \rightarrow \|F'\rangle$	Detuning [MHz]	Power [mW]
2D MOT cooling	$\|2\rangle \rightarrow \|3\rangle$	-42	130
2D MOT repump	$\|1\rangle \rightarrow \|2\rangle$	-23	65
Imaging	$\|2\rangle \rightarrow \|3\rangle$	0	0.1/0.3*
Push	$\|2\rangle \rightarrow \|3\rangle$	-12	3
3D MOT repump	$\|1\rangle \rightarrow \|2\rangle$	-9	5/10†
3D MOT cooling	$\|2\rangle \rightarrow \|3\rangle$	-14	55
Slower cooling	$\|2\rangle \rightarrow \|3\rangle$	-108	330
Slower repump	$\|1\rangle \rightarrow \|2\rangle$	-104	83

*The power values refer to the coarse and fine imaging, respectively
†The power values refer to the dark-spot and imaging repumper, respectively

and more reliable shutter design [116], inspired by [117], was adopted. These shutters incorporate an electric motor that rotates a 3D-printed plate to either block or unblock the laser beam, exhibiting switching times below 0.5 ms.

Generation of repumping light

As light tuned to the cooling transition $|F = 2\rangle \rightarrow |F' = 3\rangle$ can off-resonantly excite atoms to the $|F' = 2\rangle$ state, atoms have the possibility to relax to the $|F = 1\rangle$ ground state. Consequently, a repumping beam tuned to the transition $|F = 1\rangle \rightarrow |F' = 2\rangle$ is required to pump the atoms back into the cooling cycle. For sodium, the frequency difference between these two transitions amounts to 1713.3 MHz, which exceeds the modulation range of regular AOMs. On the other hand, an electro-optic modulator (EOM)[3] can generate sidebands at 1.7 GHz and can thus be placed into the beam path in order to add the repumper light. For an EOM, the carrier frequency and the unwanted sideband are overlapped with the repumping light. As this is not a major issue for the 2D-MOT and the slower beam, which is presented in figure 3.7 A, an EOM is used in these beams to create the repumping light.

[3] QUBIG PM-Na 1.7

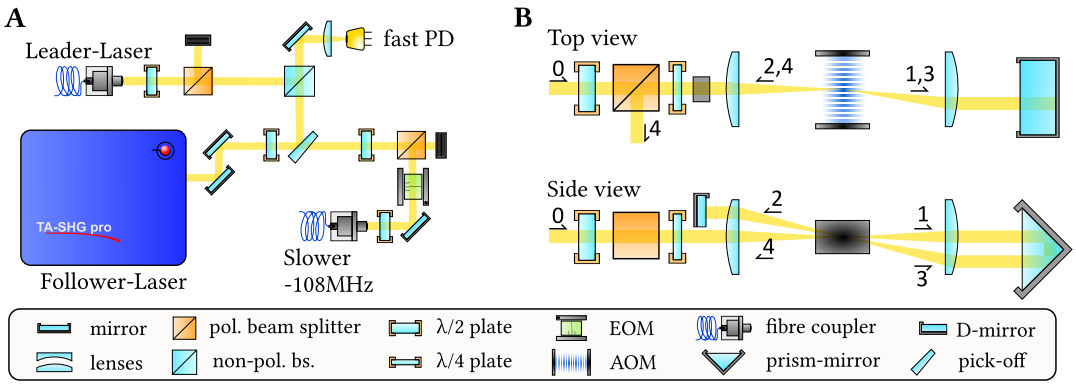

Figure 3.7.: Schematic of the sodium follower-laser system setup (A) and the AOM quadruple-pass to generate the sodium repumping beam (B). A: The follower-laser supplies the light for the Zeeman slowing beam in the 2D-MOT, where an EOM produces the repumping sideband. A small fraction of light from the follower laser is mixed with light from the leader-laser and overlapped on a fast photodiode (PD). B: Top and side view of the sodium AOM quadruple-pass. Light passes four times through this 400 MHz AOM, where the vertical axis is exploited to achieve more than two passes. A prism mirror vertically translates the beam, and a D-mirror retro-reflects after the second pass. The fourth order is split from the input light with a polarizing beam splitter.

However, for the dark SPOT repumper[4] and the imaging repumping beam, it is crucial to avoid the presence of cooling light. One possible solution involves the use of a high-frequency AOM[5] operating at 1.7 GHz. Unfortunately, this AOM yielded total efficiencies (diffraction efficiency and coupling efficiency) below 10 % and lacked long-term stability [105].

An alternative approach entails passing a regular AOM more than two times [118–120]. As the complexity of such a setup increases with every pass, we opted for implementing a quadruple pass using a 350 MHz AOM[6], similar to the setup presented in [121]. The optical layout from a top and side view is depicted in figure 3.7 B.
In this configuration, the beam initially passes through a half-wave plate and a PBS, and is then circularly polarized using a quarter-wave plate. As shown in the side view, the beam is focused into the AOM using lenses in double cat's eye configuration ($f = 100$ mm). The zeroth diffraction order is blocked, and the first order is vertically displaced by a right-angle prism mirror, such that this beam is frequency-shifted by f_{rf}[7]. Utilizing the vertical spatial axis, the beam passes through the AOM an additional three times. A D-shaped mirror is employed to selectively reflect the beam after its second pass. After passing the AOM four times, the beam is frequency-shifted by $4 f_{\mathrm{rf}}$ and can be coupled out by passing through the quarter-wave plate once again, generating s-polarized light that is reflected by the PBS.

We aligned this setup by starting with the single-pass and optimizing the diffraction efficiency into the first order to approximately 90 %. Subsequently, the prism mirror was introduced, and its position and angle were finely adjusted. The height of the prism influences the vertical spacing between the incoming and reflected beam, and has to be chosen large enough to achieve an adequate separation. As the angle of the prism had a substantial impact on the efficiency after the second and fourth pass, it was mounted on a rotation mount.
Once some light was detected in the fourth order, the alignment procedure was iteratively repeated. Adjustments were made to the D-shaped mirror, the AOM angle, and the alignment of the right-angle prism mirror. With the AOM frequency set to 388 MHz, we achieved a quadruple pass efficiency of 45 % and a total efficiency after coupling the output light into a single-mode optical fibre of 23 %. Although occasional

[4] Further details regarding this special repumping beam will be given in section 4.1.
[5] Brimrose EF-1700-100-589
[6] Gooch & Housego 3350-199
[7] This is the RF-frequency supplied to the AOM.

realignment is necessary, this setup is still easier to maintain and achieves more than twice the efficiency compared to the single 1.7 GHz AOM.

3.2.2. Potassium laser table

The potassium laser system, situated on a separate optical table, consists of two external cavity diode lasers[8]. One of these lasers emits D1-light at a wavelength of approximately 770.1 nm, while the other supplies D2-light at 766.7 nm.

Frequency stabilization

Similar to the procedure with sodium, the emitted light is frequency-stabilized to an atomic reference in a saturated absorption spectroscopy setup, depicted in figure 3.8 A. Both lasers' beams traverse a shared spectroscopy cell, which is heated to a temperature of approximately 70 °C. A coil, wrapped around the vapour cell, generates the magnetic field for the Zeeman modulation technique. To avoid obstruction of the incoming beam, retro-reflection (pump-probe configuration) of the beams after their passage through the cell is achieved using D-shaped mirrors.

[8]TOPTICA Photonics DL Pro

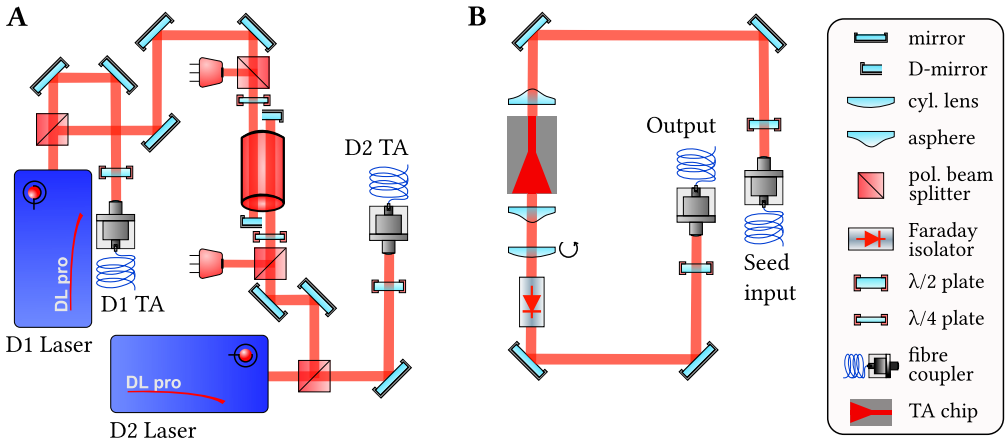

Figure 3.8.: ^{39}K optical layout for frequency stabilization and light amplification. A: The laser beams from the D1- and D2-laser pass through polarising beam splitters, such that a small fraction is used to lock the laser to an atomic reference, while the rest is coupled into a fibre. B: The coupled light acts as an input seed for a standalone fibre-coupled tapered amplifier (TA) unit. The seed light is amplified to approximately 2 W, and subsequently coupled into a fibre. A Faraday isolator prevents back-reflections that could damage the TA-chip.

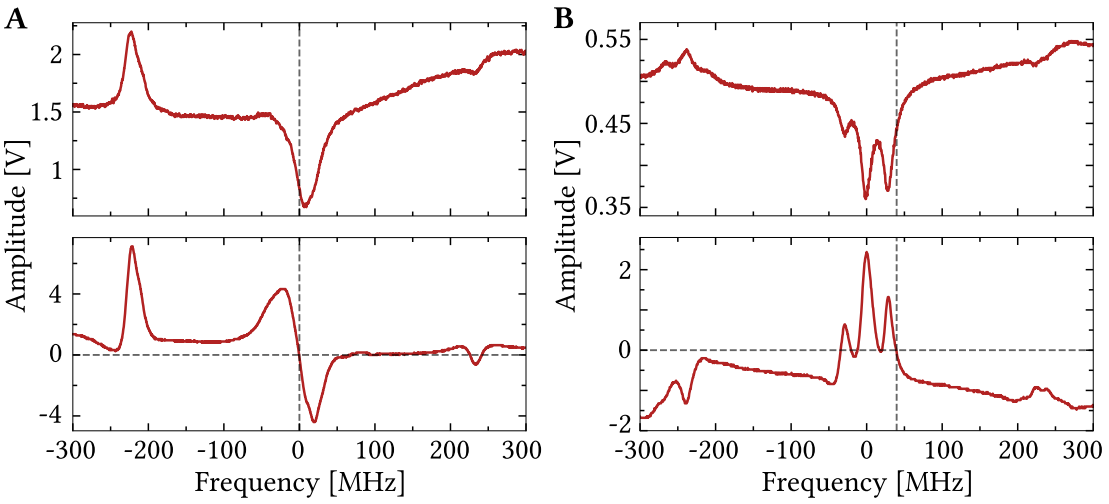

Figure 3.9.: ^{39}K laser locking signals for the D2- (A) and D1-line (B). A: The top graph shows the D2 spectroscopy signal with a central ground state crossover dip. The left peak corresponds to transitions $|F = 2\rangle \rightarrow |F' = 1, 2, 3\rangle$, while the feature on the right results from transitions $|F = 1\rangle \rightarrow |F' = 0, 1, 2\rangle$. The bottom graph presents the corresponding error signal. B: D1 spectroscopy and error signal featuring a central ground state crossover dip, several peaks on the left caused by transitions $|F = 2\rangle \rightarrow |F' = 1, 2\rangle$ and a feature on the right resulting from transitions $|F = 1\rangle \rightarrow |F' = 1, 2\rangle$. The lock-points are indicated by the grey dashed lines.

The resulting spectroscopy data and corresponding error signals are presented in figure 3.9. The D2-line, shown in panel A, exhibits transitions, namely $|F = 2\rangle \rightarrow |F'\rangle$ (left peak), $|F = 1\rangle \rightarrow |F'\rangle$ (dip on the right), and the central crossover feature $|F = 1, 2\rangle \rightarrow |F'\rangle$. The locking point, indicated by the dashed grey lines, corresponds to a frequency setting approximately 20 MHz red-detuned with respect to the transition $|F = 1, 2\rangle$ (CO) $\rightarrow |F' = 3\rangle$.

The spectroscopy and error signal for the ^{39}K D1-line are displayed in figure 3.9 B. Due to the larger energy splitting of the excited state, the fine structure of the excited state is resolved. The central ground state crossover exhibits three distinct features corresponding to transitions to the $|F' = 1\rangle$, $|F' = 1, 2\rangle$ (CO) and $|F' = 2\rangle$ excited states. The D1-laser is frequency-locked to a point approximately 13.9 MHz blue-detuned with respect to the transition $|F = 1, 2\rangle \rightarrow |F' = 2\rangle$ (as marked by the grey dashed line).

Light amplification

The diode laser outputs approximately 50 mW of light. However, a significant amount of light is lost during the subsequent frequency-shifting and fibre coupling processes.

To compensate for this power loss, we amplify the beams from the D1- and D2-lasers using fibre-coupled home-built tapered amplifier (TA) units [111, 122], referred to as the D1- and D2-TAs.

Figure 3.8 B shows a schematic of the optical layout for such an amplifier unit. The 20 mW of fibre-coupled seed light is amplified to approximately 2 W by guiding the light through a tapered amplifier chip[9]. An optical isolator, with a transmission of roughly 80 %, is employed to prevent any back-reflections, which could potentially damage the chip. The output mode after the TA chip is shaped using a cylindrical lens to efficiently couple the light after the isolator into a single-mode fibre. Through the inclusion of a rotation mount to align the axis of the cylindrical lens accurately, coupling efficiencies of up to 57 % were achieved, resulting in a fibre-coupled output power of approximately 1.04 W [123].

Frequency shifting

The amplified laser light is subsequently divided into several paths and frequency-shifted using acousto-optical modulators. A schematic outlining the optical layout of this process is provided in figure 3.10. Moreover, figure 3.11 showcases images of the potassium optical table.

In the case of ^{39}K, the hyperfine splitting in the ground state is about 461.7 MHz. Consequently, by stabilizing the lasers to the ground state crossover, we can utilize the first positive AOM diffraction order to produce the repumper, and the first negative order to generate the cooling beam. The light from these two AOM paths is then superimposed on non-polarizing beam splitters, resulting in a 50 % power loss in the unused output port.

For the push beam, we couple out a few mW of the 2D-MOT[10] cooling light. Given the substantial power requirement for optimal loading into the 3D-MOT, the 2D-MOT light traverses another custom-built tapered amplifier (2D-MOT TA) before being transferred to the main experiment table.

The 3D-MOT beams have to carry both D2-light for the MOT and D1-light for the grey molasses. Consequently, after combining cooler and repumper beams, the D1- and D2-light is overlapped on a tunable bandpass filter[11]. As the transmission band of this filter depends on the incident angle, it is mounted on a rotation mount, and

[9] Eagleyard Photonics EYP-TPA-0765-02000

[10] To prevent any back-reflections from entering the 3D-MOT or imaging AOM paths, we strategically positioned the 2D-MOT double-passes at the beginning.

[11] Semrock TBP01-790/12

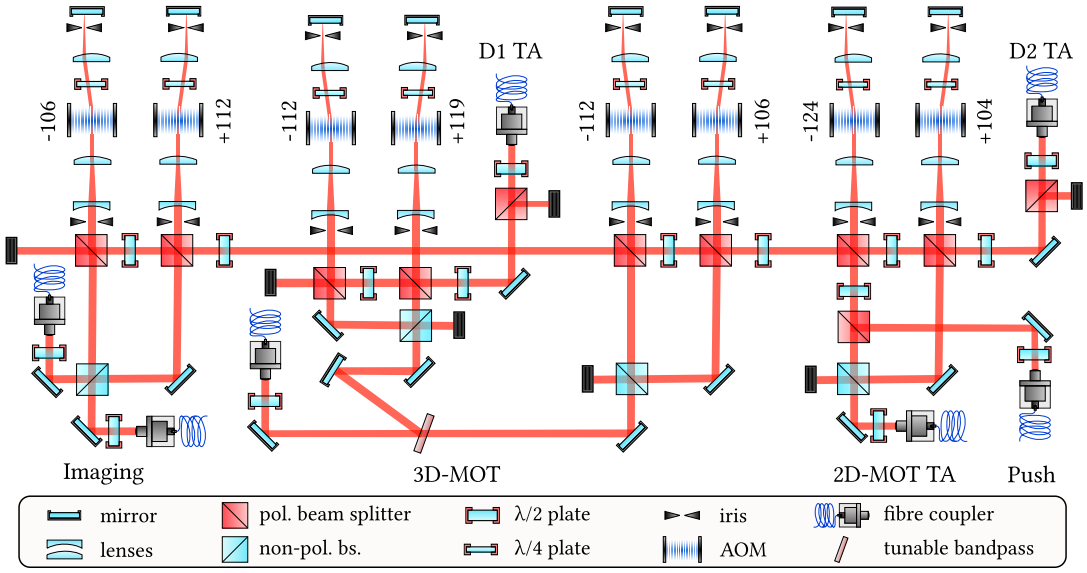

Figure 3.10.: Schematic of the ^{39}K laser system. Each path has a cooler and repumper beam, which are independently frequency-shifted and then superimposed on non-polarising beam splitters (non-pol. bs.). Following the frequency-shifting, the light is coupled into single-mode optical fibres transporting the laser beams to the experiment table. For the 2D-MOT light, there is another amplifier stage (2D-MOT TA) in between. The AOM RF-frequencies are given in MHz.

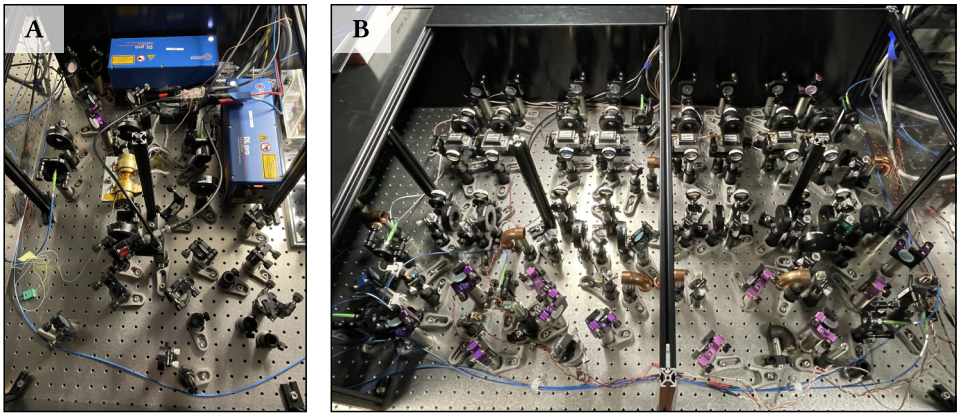

Figure 3.11.: Images of the ^{39}K laser system. A: D1- and D2-lasers with the saturated absorption spectroscopy setup. The spectroscopy cell is positioned in the centre, with the two brass band heaters standing out. B: Optical layout for splitting the light into multiple paths and frequency-shifting the individual beams using AOMs.

Table 3.2.: Frequency detunings and power values for the different ^{39}K laser beam paths. The frequency detuning is given with respect to the transition denoted in the second column. The power was measured after the fibre outcoupler on the experiment table.

	Transition $\|F\rangle \rightarrow \|F'\rangle$	Detuning [MHz]	Power [mW]
2D MOT cooling	$\|2\rangle \rightarrow \|3\rangle$	-37	300
2D MOT repump	$\|1\rangle \rightarrow \|2\rangle$	-22	150
Push beam	$\|2\rangle \rightarrow \|3\rangle$	-37	2
3D MOT D2 cooling	$\|2\rangle \rightarrow \|3\rangle$	-13	30
3D MOT D2 repump	$\|1\rangle \rightarrow \|2\rangle$	-18	20
3D MOT D1 cooling	$\|2\rangle \rightarrow \|2\rangle^*$	20.8	30
3D MOT D1 repump	$\|1\rangle \rightarrow \|2\rangle^*$	20.8	13
Imaging cooling	$\|2\rangle \rightarrow \|3\rangle$	-1	1
Imaging repump	$\|1\rangle \rightarrow \|2\rangle$	-6	1

*For this transition the excited state manifold is $4^2P_{1/2}$.

the angle is adjusted to optimize the reflectivity of the D1- and the transmission of the D2-light. Compared to a non-polarizing beam splitter with 50 % efficiency, this tunable bandpass filter enables us to achieve an efficiency of approximately 90 %.

Finally, the D2-light is also shifted close to resonance to serve as the absorption imaging beams. These imaging beams, carrying both cooler and repumper, are coupled into two separate single-mode polarization-maintaining optical fibres. This setup allows for the utilization of two separate imaging systems, each with its own magnification. Table 3.2 summarizes the frequency detunings and power settings for the various potassium beam paths. These settings were obtained through optimization of the MOT and grey molasses with respect to atom number and temperature.

3.2.3. Optical layout on the experiment table

The laser light is transported from the laser tables to the main experiment table, which accommodates the vacuum system, through 10 m long single-mode optical fibres. On the main experiment table, these fibres distribute the light to the 2D-MOT, push beam, 3D-MOT, and imaging setups. The arrangement of optics around the science chamber

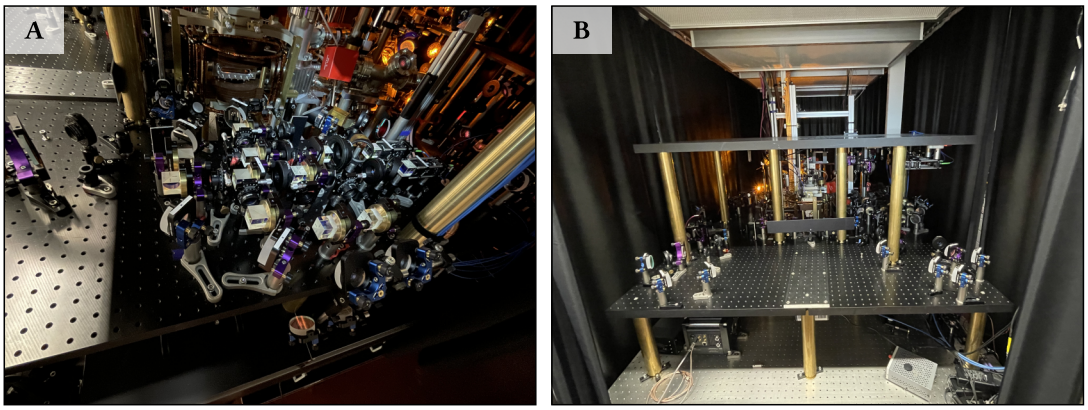

Figure 3.12.: Images of the optical layout on the main experiment table. A: Beam splitting optics for the sodium and potassium 3D-MOT. Due to the size of the MOT beams of 15 mm, 1 inch polarizing beam splitters are required. B: Image of the experiment table visualizing the basic structure of three levels separated by optical aluminium breadboards.

is structured into three layers, each separated by 30 mm thick anodized aluminium breadboards, that are mounted on brass posts, as shown in figure 3.12.

As the coils are mounted above and below the chamber, four of the six MOT beams lie in the horizontal plane, intersecting at right angles in the centre of the chamber. Since these coils block quite a lot of optical access, the elongated viewports on the sides of the chamber are the main entry points for additional laser beams, such as the dipole beams. Consequently, a large U-shaped breadboard[12] encircling the entire chamber is used to mount most of the MOT and dipole trap optics. The decision to mount a majority of the optics on a large, contiguous breadboard was made to enhance the stability of the system. By mounting optical components on a single breadboard, any potential vibrations or mechanical perturbations are effectively rendered common mode, rather than introducing differing perturbations.

The various cameras needed for imaging are positioned on the lowest level, directly on the optical table. The top layer, currently unoccupied, will be used to potentially install a digital-micro-mirror device (DMD) setup, facilitating the creation of arbitrary attractive or repulsive potentials in the xy-plane. Additionally, the underside of the breadboard serves as a mounting platform for the vertical MOT beams.

On the middle breadboard, the 3D-MOT light is coupled out of the fibre and colli-

[12] As the fabrication of such a large breadboard proved infeasible, we decided to construct two symmetrical halves and stitch them together using two thinner breadboards - one positioned on top and the other below.

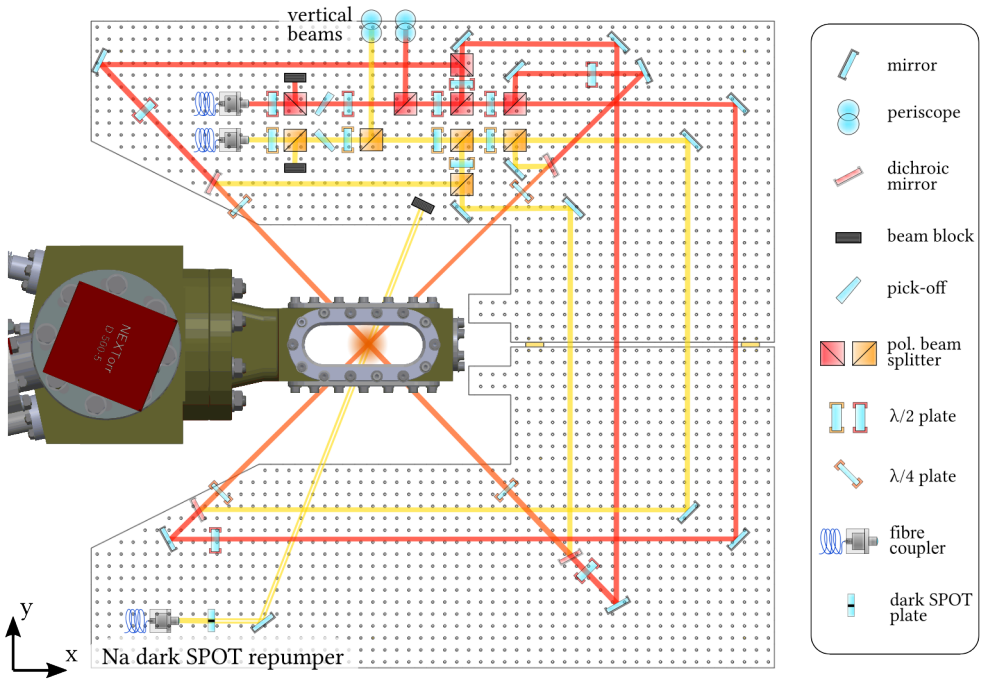

Figure 3.13.: Top view of the optical layout of the MOT optics on the main experiment table, mounted on a U-shaped breadboard. The three pairs of counter-propagating MOT beams for sodium and potassium are generated by splitting the beams using polarizing beam splitters. The implemented splitting configuration allows independent power balancing for each axis, facilitating the optimization of the optical molasses. The light for the two species is overlapped for each path at the very end using a dichroic mirror. The sodium dark SPOT repumping beam is provided by a separate laser beam (bottom left).

mated using an achromatic doublet lens ($f = 75\,\text{mm}$), resulting in a beam diameter of approximately 15 mm, tailored to match the size of the elongated viewports. This beam diameter necessitates the use of 1 inch PBS cubes and 2 inch mirrors. The optical layout is depicted in figure 3.13.

While the fibres are designed to preserve polarization, they exhibit slight polarization rotation with fluctuations in the room temperature. These polarization changes would translate to relative power drifts in the individual MOT beams, negatively affecting the MOT and molasses. To address this issue, an additional cleaning cube is employed to ensure polarization purity. Overall power fluctuations are monitored using a beam sampler that reflects 1 % of the incident light onto a dedicated photodiode.

Subsequently, the beam is divided into three pairs of counter-propagating beams, and the beam-balancing for each pair can be adjusted using a half-wave plate mounted in a

precision rotation mount[13]. This fine adjustment proved particularly beneficial during the optimization of beam balancing for the sensitive molasses stage.
The entire optical layout is replicated for the other species. The beams for the two species are overlapped on the final in-coupling mirror using a long-pass dichroic mirror[14] for each of the six directions. Each dichroic mirror reflects sodium light, while potassium light is transmitted. This arrangement, where the beams are superimposed only on the very last mirror, enables independent optimization of the MOT beam alignment for each species.
The working principle of an optical molasses relies on circularly polarized laser beams. This circular polarization is generated from the linear input using achromatic quarter-wave plates[15]. To ensure the correct circular handedness for both species, we inserted an additional half-wave plate in the potassium beam for independent adjustment. Furthermore, the sodium MOT is operated in a so-called *dark-SPOT MOT* configuration, which will be elaborated on in section 4.1. The six sodium MOT beams only carry cooling light, while the separate repumping beam (see bottom left of figure 3.13) features a hollow beam profile.

3.3. Magnetic field coils

In the field of ultracold atoms, a wide range of tools is available to manipulate the quantum-mechanical state of atoms. Magnetic fields are one of the most effective instruments. The utilization of magnetic fields commences in the 2D-MOT, 3D-MOT, and magnetic trap, where a quadrupole magnetic field gradient is required to generate a spatially-dependent trapping force. Moreover, in the latter stages of the cooling cycle, a magnetic bias field can be employed to adjust the interaction strength using magnetically tunable Feshbach resonances. There are two main approaches to create the desired magnetic field configuration - permanent magnets or magnetic field coils.

Permanent magnets are very easy to handle, compact, and cost-efficient. They have been employed in the past to create magnetic traps for neutral atoms [124, 125]. However, these magnets lack the capability to be switched off or varied in their field strength, which is essential for tasks such as time-of-flight measurements or adiabatic compression. For our 2D-MOT, serving as a source of cold atoms, we use neodymium bar

[13] Thorlabs CRM1PT/M
[14] Thorlabs DMLP605L
[15] Thorlabs AQWP10M-580

magnets[16], as tunability is less critical for this stage. Additional information regarding the field configuration in the 2D-MOT can be found in Lilo Höcker's Ph.D. dissertation [126], drawing inspiration from similar approaches outlined in [127, 128].
Magnetic field coils consist of wound copper wire, carrying electric current. Placing two coils at a certain distance along the same axis enables the generation of a bias or gradient magnetic field based on the relative direction of current flow (Helmholtz or anti-Helmholtz configuration). The magnetic field strength can be finely tuned, and the coils can be switched on or off by regulating the current accordingly. This tunability renders magnetic field coils ideal to create the necessary fields around the science chamber. However, for applications requiring large currents (in the order of a few hundred amperes), effective water cooling systems must be installed. Additionally, in case the water cooling is interrupted and the coil body heats up substantially, an interlock circuit (see appendix A.3) should interrupt the electrical connection.
In our experiment, two types of magnetic field coils are utilized, each differing significantly in dimension, geometry, and application:

OFFSET COILS serve the purpose of compensating stray magnetic fields, including the Earth's magnetic field. A pair of coils is positioned along each spatial direction to generate bias fields in the order of a few Gauss.

MAIN COILS produce the necessary magnetic field configurations for the MOT and magnetic trap, with gradients of up to 300 G/cm. Additionally, these coils have the capability to produce bias magnetic fields of up to 600 G, allowing for the fine-tuning of the s-wave scattering length across different inter- and intra-species Feshbach resonances.

In the following, I will first introduce the offset coils, focusing on the coil assembly and detailing the specifications of these coils. Following this, I will discuss the main coils, starting with the design considerations. After presenting the performance characteristics, the last section will cover current control and switching.

3.3.1. Offset coils

As previously indicated, the offset coils have to compensate stray magnetic fields in the order of approximately 1 G along all three spatial directions. This objective is achieved by positioning a pair of coils operated in Helmholtz configuration along each axis.

[16] ECLIPSE N750-RB

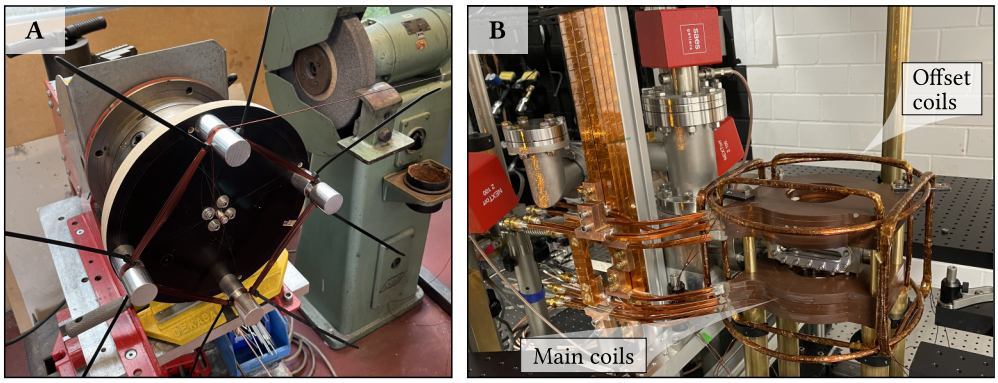

Figure 3.14.: Images of the offset coils. A: Fabrication of a rectangular offset coil using a lathe. Following the winding process, the coil is secured with cable binders and then tightly wrapped with Kapton-tape. B: Final coil configuration including the main coils and the offset coils. The offset coils are fixed to each other and to the main coils using cable binders.

The coils were wound from 1 mm enamelled copper wire using a lathe. For the square coil, four posts were attached to the lathe, and the wire was wound around these posts. In the winding process, shown in figure 3.14 A, it was essential to carefully wind the enamelled copper wire around the posts to achieve a uniform coil structure. The tension and alignment of the wire during winding were crucial to ensure that the resulting coil would meet the desired specifications and performance.

After reaching the correct number of windings, the coil was secured using Kapton-tape and subsequently detached from the lathe and the posts. This design does not require an additional holder, as the coil's shape is maintained through the Kapton-tape, resulting in a highly space-efficient design while still ensuring long-term stability [129]. In a similar fashion, the round coil was wound around a circular frame that was made to fit the dimensions of the coil design with respect to the inner radius. The individual coils are held together and fixed to the frame of the main coils using cable binders. The assembled coil setup is depicted in figure 3.14 B.

The coil dimensions and specifications, summarized in table 3.3, were determined through a design process that took into account spatial constraints imposed by the vacuum system, the desired magnetic field strength, and the homogeneity of the bias field in the centre. The chosen dimensions were a result of optimizing these factors. The field strength for each coil pair was measured along its common axis using a fluxgate magnetic field sensor[17].

[17]Bartington Instruments Mag03-IE-1000

Table 3.3.: Offset coils characteristics. For the square x- and y-coils, we report the mean side-lengths, while the mean diameter is given for the round z-coil.

	x-coil	y-coil	z-coil
Dimension [mm]	170 × 170	200 × 200	⌀270
Distance [mm]	230	145	150
Number of windings	50	30	30
Field strength [G/A]	1.78(1)	1.92(1)	1.62(1)

3.3.2. Main coils

One of the most advantageous features of the ^{23}Na-^{39}K mixture lies in the presence of multiple broad inter-species Feshbach resonances at relatively low magnetic bias fields. This characteristic offers a high degree of control over the interaction strength, enabling precise tuning from strongly attractive to repulsive regimes.
Considering the inter-species Feshbach resonances for the $|1, -1\rangle$ spin state at 32.5(8) G and 247.1(2) G [71], and the intra-species ^{39}K resonances located at 33.5820(14) G, 162.36(2) G, and 561.14(2) G [98], we established the requirement for the bias field to reach up to 600 G.
In our experimental setup, achieving the necessary magnetic field gradients is crucial for various cooling and trapping stages, such as the MOT or the magnetic trap. For the MOT, we require low magnetic field gradients in the order of 10 G/cm. On the other hand, to attain high densities, particularly in the runaway regime for microwave evaporation, the magnetic trap necessitates gradients of up to 300 G/cm.
To efficiently meet both these requirements, our objective was to design a single set of coils capable of switching between a magnetic field gradient and a homogeneous field. This design aims to provide the versatility needed to adapt to various stages of the experiment, enhancing its overall flexibility and performance.
In the following subsections, we will delve into the details of the design, fabrication, and performance of this coil pair, highlighting its ability to meet the specified criteria.

Coil design

An essential aspect when designing magnetic field coils is determining the optimal distance between the coils, which varies based on whether they are operated in Helmholtz or anti-Helmholtz configuration. In Helmholtz configuration, the first and second derivative of the magnetic field are zero when the distance between the coils is $d = R$,

with the coil radius denoted as R. Conversely, in an anti-Helmholtz setting, aimed at producing a linear gradient, the second and third derivatives vanish when $d = \sqrt{3}\,R$. To implement both configurations with the same pair of coils, we adopted the following approach. We utilized the entire coil for gradient operation while relying solely on the innermost windings to generate a homogeneous bias field. This configuration is illustrated in figure 3.15, which shows a view from the side cutting through the water-filled hollow-core copper wire.

Another more technical challenge, as evident in figure 3.15, is the limited amount of available space. The science chamber imposes a restriction on the minimum distance between the coils ($d_{\text{inner}} > 60$ mm), while the vacuum flange on the left limits the outer diameter of the coil to a maximum of 180 mm.
In addition to the physical constraints imposed by the vacuum system, careful consideration must be given to the optical access requirements for various laser beams. The high numerical aperture (NA) imaging objective, with an outer diameter of 54 mm, needs to fit within the bottom coil close to the viewport. Furthermore, the coil connections have to be bent in a manner that does not obstruct the MOT beams, as depicted in figure 3.14 B.

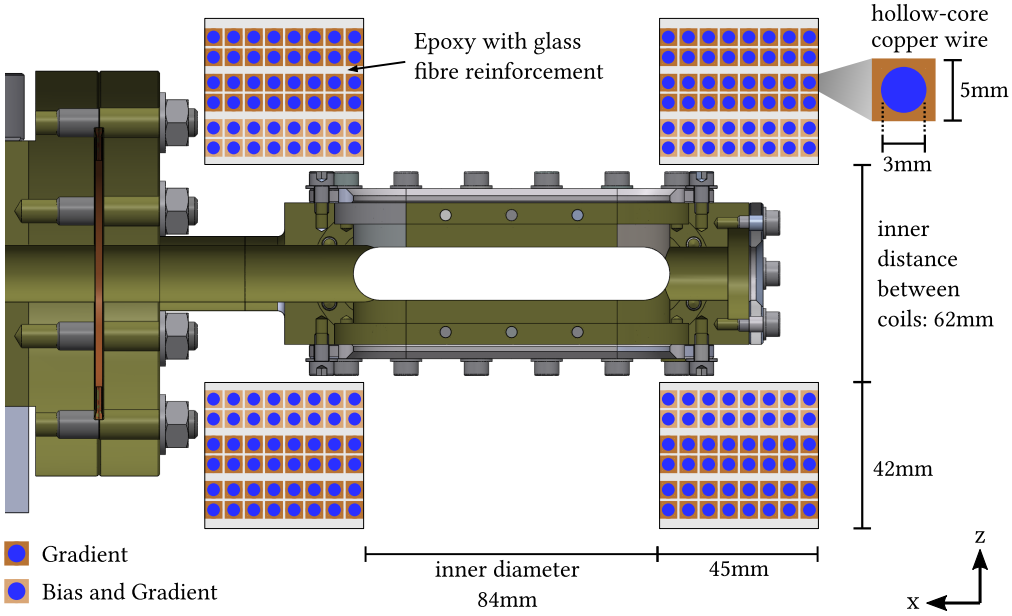

Figure 3.15.: Cross-section of the science chamber with the main magnetic field coils. The coils, wound from hollow-core copper wire, consist of eight radial and six axial windings. The main coil and the different distances are to scale with respect to the dimensions of the science chamber.

To produce the strong magnetic bias and gradient fields required for our experiment, high currents are necessary, resulting in a dissipated power in the kW range. Hence, an efficient active cooling solution has to be implemented to effectively dissipate this heat.
In our previous coil design, based on a bulk-machined electromagnet approach [130], we encountered difficulties with heat dissipation. The coils were fabricated by cutting a spiral into a bulk copper block using a wire erosion machine, and filling the gaps between the individual windings with epoxy. A PEEK cap screwed onto the copper coil facilitated a water channel, ensuring direct contact between the cooling water and the copper windings. However, during fabrication, we encountered some difficulties with air bubbles forming in the epoxy, leading to minor leaks in the system. Despite sealing these water leaks, there were still issues with the water-tight fit between the copper coil and the PEEK component. Moreover, as the innermost and outermost windings were not in direct contact with the cooling water, these regions heated up quickly, rendering a continuous operation at currents exceeding 150 A impossible.
To address these issues and enhance the coil design, we took inspiration from other experimental setups within our research group [131, 132]. We decided to make new hollow-core coils, where water flows through an internal channel, significantly improving cooling efficiency owing to the large surface area of the water-to-copper interface. This upgrade was critical in enhancing heat dissipation and enabling continuous operation at higher currents, meeting the demands of our experiment.

The final optimized coil design features an outer diameter of 174 mm with 8×6 windings per coil. Each coil has an inner hole diameter of 84 mm and a thickness of 42 mm. The coils are fabricated in stacks of 8×2 windings each with a thickness of 14 mm, such that the top and bottom coil each consist of three of these coil stacks. A technical drawing of such a coil stack is attached in appendix A.4. The distance between the two coils is set to 62 mm, providing a slight space buffer for the screws of the science chamber vacuum flange.
To evaluate the performance of these coils, we simulated their behaviour using the Biot-Savart law and perform numerical integration to calculate the field within a region of 100 µm around the centre. In Helmholtz configuration, the magnetic field scales as 2.0 G/A[18], while the gradient varies with the applied current as 1.02 G/cm/A. Thus, a current of 300 A would be sufficient to reach our predefined targets.
Figure 3.16 illustrates the homogeneity of the coils around the centre when operated

[18]The experimentally extracted calibration using microwave spectroscopy is given in table 5.2.

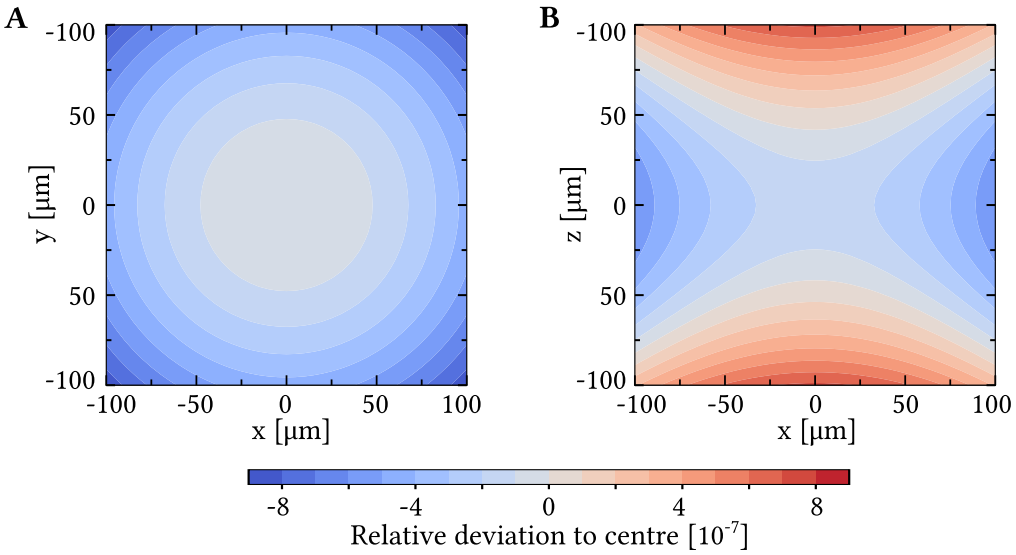

Figure 3.16.: Simulated homogeneous magnetic field produced by the main coils in the xy- and xz-plane, showing the relative deviation with respect to the centre value, which scales as 2.0 G/A. While the field exhibits a maximum in the centre of the xy-plane (A), the field increases in the z-direction when moving away from the centre towards the coils (B).

in Helmholtz configuration. Over a range of 100 µm, the magnetic field changes by approximately 8×10^{-7}. The typical operation regime for our particular atomic mixture is in the range of 150 G, leading to absolute magnetic field changes in the order of 0.12 mG. Achieving this high level of homogeneity is essential, particularly for the Feshbach resonances, ensuring a consistent interaction strength across the atomic cloud.

Coil fabrication and assembly

The coils are wound from hollow-core copper wire, featuring a rectangular profile with 5 mm side length and a circular hole diameter of 3 mm. The resistance of this wire is specified to be $1.017\,\mathrm{m}\Omega\,\mathrm{m}^{-1}$. The coils were externally manufactured[19] in stacks of eight radial and two axial windings. The copper wire was wound around a cylinder, resulting in a coil configuration where the connections for the two axial windings are positioned on the outside next to each other. This arrangement simplifies the setup for current and water connections. To ensure structural stability and durability, each coil stack was firmly secured using casting resin with additional glass-fibre reinforcements. Each final coil consists of three stacks, totalling 48 windings, with six current/water

[19] Krämer Energietechnik GmbH

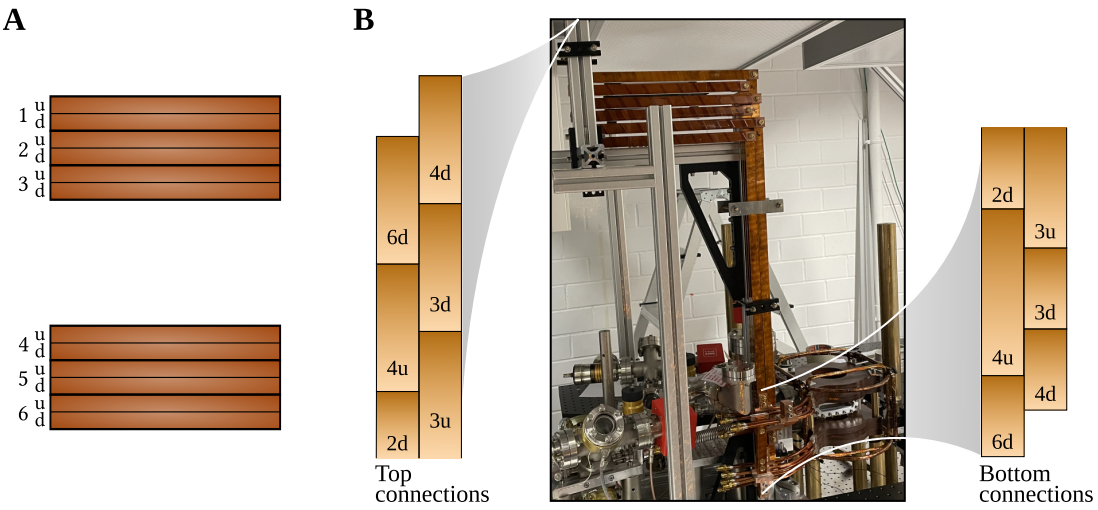

Figure 3.17.: Magnetic field coil connections. A: Side-view of the magnetic field coils. The coil stacks are numbered from 1 to 6, with each stack consisting of two axial windings, denoted by up (u) and down (d). B: Coil connections to the copper bars on the coil side (bottom connection) and on the top side connecting to the switching circuitry. The windings 2u, 1d, 1u, 5u, 5d and 6u are hard-wired in gradient configuration, as illustrated in figure 3.19.

connections per coil.

In the assembly of each coil stack, precise measures were taken for wire connection and current conduction. The connection wires were cut to the appropriate length, followed by soldering of the water connectors[20] to the wire ends. During this soldering process, careful attention was given to prevent any solder from entering the hollow-core and causing blockages.
For the current connections, copper pieces were soldered to the wires, and these soldered connections were then finally screwed to the corresponding connections. The outer two stacks of the top and bottom coils are fixed in an anti-Helmholtz configuration. On the other hand, the innermost coil stacks are designed to be switchable, keeping all four connections flexible. Additional details regarding the assembly of the coil configuration are contained in appendix A.5.

The current is led away to the top of the experimental table housing using six copper bars, that are clamped to *Item* construction posts. This construction, along with the assignment of the copper bars to the different coil windings, is shown in figure 3.17.

[20] Swagelok B-6M0-6

The copper bars have a cross-section of 1 cm × 2 cm, reducing the amount of dissipated heat while efficiently carrying currents of up to 300 A. A straight connection from the coil to the current control circuitry positioned on top of the optical table enclosure, proved to be impossible, because of a flow box that was in the way. Therefore, we opted for the solution shown in figure 3.17 B, that involved adding horizontal copper bars between the vertical ones to by-pass the flow box.

Several 185 mm^2 copper-stranded wires further connect to the switching circuitry and the current source. We utilize a current source[21], capable of supplying up to 440 A at 15 V[22].

The bottom coil stacks are mounted on 300 mm long brass posts with a diameter of ⌀30 mm. The length of these posts is set by the height of the science chamber above the optical table. To ensure proper positioning, brass spacers were added to address a slight initial misalignment, guaranteeing symmetrical placement of the coils with respect to the chamber.

On the other hand, the top coil stacks are fixed to the bottom construction using 62 mm long brass spacers with a diameter of ⌀10 mm. The position and diameter of these spacers was carefully chosen to minimize any obstruction to optical access. The coil connections were bent to the side and attached to the copper bars. This entire coil construction also serves as a mounting platform for the offset coils.

The water cooling system for these coils is provided by a dedicated chiller[23], which is connected to the institute's cooling water system to effectively dissipate the heat. The chiller's inlet and outlet are linked to a distribution setup that uses deionised water. The inlet is filtered and pressure-limited to maintain a water pressure of 4 bars. Subsequently, the water is distributed into three inlets and outlets, terminated by faucets and 1/2 inch hose fittings. A garden hose[24] transports the cooling water to the experiment table, where it is divided into twelve 6 mm plastic tubes using a custom brass water distributor. A technical drawing of this water distributor is attached in appendix A.4. The 6 mm plastic tubes are connected to the hollow-core copper wires through the Swagelok tube fittings that were soldered to the wire ends. This arrangement provides parallelized cooling for the six coil stacks.

[21] Delta Elektronika SM 15-400
[22] If the voltage becomes a limiting factor, a second power supply can be connected in series.
[23] EF cooling WKW 86
[24] Gardena SuperFLEX 13 mm

Current control and switching

During an experiment cycle, magnetic fields have to be adjusted and turned on or off on microsecond time-scales. The circuitry, connecting to the top end of the copper bars and enabling the rapid current control, is shown in figure 3.18.
The fast switching times can be achieved with a *passbank*, which consists of a series of transistors connected in parallel. Each transistor is equipped with an LED, indicating whether the transistor is properly functioning or not[25]. The passbank enables rapid control of the magnetic fields by modulating the current flowing through the coils (further details in [133]). To precisely monitor the current, two current transducers (LEM1 and LEM2) are employed, serving as feedback sources for the PID drivers of the passbanks. This feedback mechanism ensures accurate regulation of the current, aligning with the experimental requirements. More details on the passbank driver, including the circuit diagram, are presented in appendix A.2.
Additionally, an H-bridge configuration is utilized to reverse the current direction through one of the coils, changing between gradient and Feshbach configuration. In the gradient configuration, it is required that the current directions in the top and bottom coils are opposite, while a bias field is generated when the current flows in the same direction. The coil connections for both cases are outlined in figure 3.19.

[25] On a few occasions, the passbank overheated, damaging one or two transistors. These faulty transistors were then easily identified by looking at the LEDs.

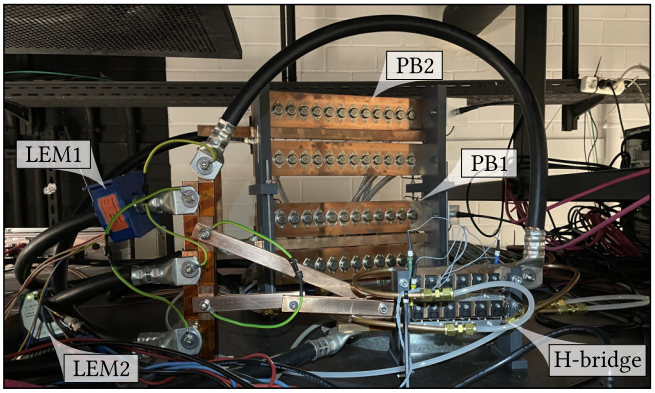

Figure 3.18.: Image of the current control and switching circuitry located on top of the experimental table housing. Copper bars and thick copper stranded wires connect from the copper bars to the H-bridge, passbanks (PB1 and PB2), and the power supply, that is located in a neighbouring laboratory. The two passbanks are mounted on top of each other to conserve the limited amount of space. The electric current passing through the coils is measured with two current transducers (LEM1 and LEM2).

In both cases, the current is initially directed through coil stack 4. The current direction through coil stack 3 can be inverted by toggling the H-bridge between its two states, enabling control over the direction of current flow through this coil. Subsequently, the connections are split up, and depending on the states of the two passbanks, depicted at the bottom, the current flow through the outer coils can be regulated. Specifically:

GRADIENT CONFIGURATION: No current flow through passbank 2 (PB2), while PB1 is utilized to regulate the field strength on LEM1. The outer coils are involved in this configuration, allowing for gradient field adjustments.

FESHBACH CONFIGURATION: In this configuration, PB1 is closed and there is no current flow through the outer coils. The bias field is exclusively produced by coils 3 and 4 and regulated on the signal of LEM2 using PB2.

Given that the outer coils are only used in Anti-Helmholtz configuration, the outer coil stacks 1, 2, 5, and 6 are hard-wired to generate a gradient field. Consequently, only the wires 2d and 6d are available for connections, as shown in figure 3.17 B. Conversely, for the inner coil stacks, all four connections are necessary to link to the power supply and the different H-bridge banks.

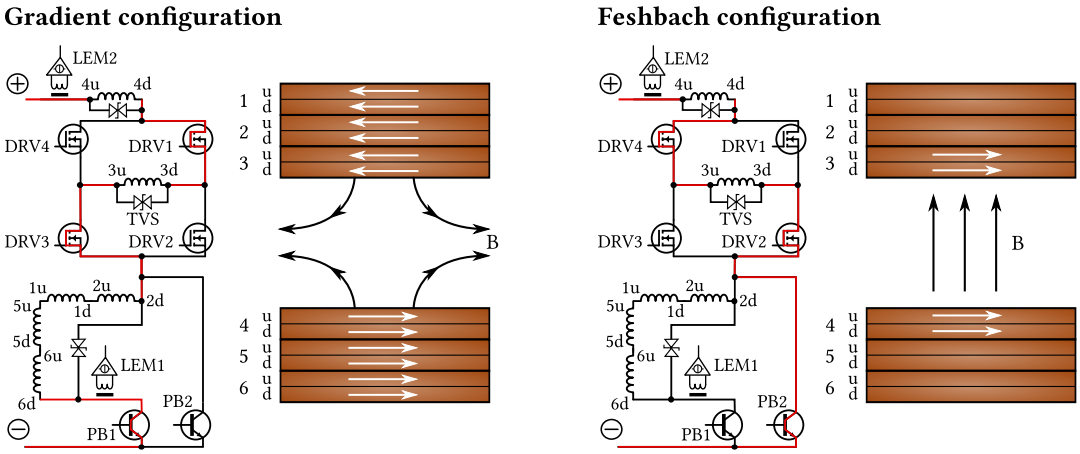

Figure 3.19.: Schematic of the magnetic field coil switching between gradient and Feshbach configuration. An H-bridge reverses the direction of current flow (indicated by red lines) through coil stack 3, while two passbanks (PB1 and PB2) are used to regulate the current for the two configurations using current transducers (LEM1 and LEM2) as a feedback mechanism. As a protective measure against voltage spikes during turn-off, the coils are equipped with TVS diodes.

Table 3.4.: Summary of the H-bridge connections. Depending on the state of the two inputs, the four outputs drive the different banks of the H-bridge. Controlled by the state of the "Switch" input, the coils can be operated in gradient or Feshbach configuration. If the "Disable" input is triggered, the current flow is interrupted.

Input Switch, Disable	Drive 1 blue*	Drive 2 red*	Drive 3 yellow*	Drive 4 green*	Config.
0,0	1	0	1	0	Gradient
0,1	0	0	0	1	Off
1,0	0	1	0	1	Feshbach
1,1	1	0	0	0	Off

*These are the colours of the connectors on the H-bridge.

The H-bridge configuration comprises four banks, with each bank incorporating six MOSFETs[26] to withstand the high current load. The circuit diagram for the H-bridge driver is presented in appendix A.1, with additional details on the design and functioning of the H-bridge described in [131].

The driver circuit features two inputs - SWITCH and DISABLE - where the former enables switching of the individual banks to reverse the current direction through the connected coil, whilst the latter is used to turn off the current flow completely by changing the bottom two MOSFET banks (drive 2 and 3) to non-conducting. The corresponding logic for the two inputs and the four drive outputs connected to the H-bridge is summarized in table 3.4.

Switching large currents on such small time-scales can induce significant voltage spikes. As a protective measure, the coils are equipped with TVS diodes that shunt excess current at high voltages and absorb much of the transient energy. In the experiment, we installed one bi-directional TVS diode[27] across each coil connection (see figure 3.19).

[26] International Rectifier IRLZ 44N
[27] Littelfuse Inc. 15KP58C

3.4. Detection methods

Absorption imaging theory

One of the most fundamental and widely used imaging techniques in the study of ultracold atoms is absorption imaging [75]. It can provide quantitative information about the atom number, spatial distribution, and temperature of an atomic cloud.

In absorption imaging, the atomic cloud is exposed to illumination from a resonant laser beam that propagates along the y-axis. Atoms within the cloud absorb the light, while the transmitted beam is captured on a camera. The absorption of this probe beam is described by Beer-Lambert's law:

$$I(x,z) = I_0(x,z)\, e^{-\mathrm{OD}(x,z)} = I_0(x,z)\, e^{-n(x,z)\,\sigma_{eg}} \tag{3.1}$$

where $I(x,z)$ is the measured transmission, $I_0(x,z)$ is the incident intensity, $\mathrm{OD}(x,z)$ is the optical density, $n(x,z)$ is the column density, and $\sigma_{eg} = \frac{3\lambda^2}{2\pi}$ is the absorption cross section, with λ being the wavelength of the laser.

In the experiment, atoms are released from the trap and allowed to fall freely during a specific time interval, referred to as the time-of-flight. After the time-of-flight, the first imaging pulse is shone on the atoms, generating a signal $I_{\mathrm{at}}(x,z)$, that displays the atomic absorption, as shown in the left image of figure 3.20. After ensuring that the trap is empty, a second imaging pulse illuminates the atoms to obtain a reference image $I_{\mathrm{ref}}(x,z)$, displaying only the beam profile without any atomic absorption. Finally, a third dark image is captured without any imaging light, denoted as $I_{\mathrm{dark}}(x,z)$. The

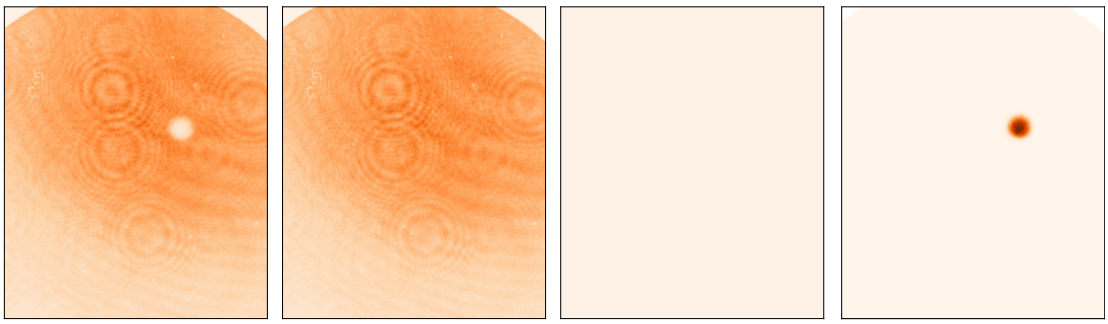

Figure 3.20.: Example images taken for the absorption imaging technique. The optical density (right image) is calculated from the atom image, reference image and dark image according to equation 3.2.

optical density is obtained from these three images by

$$\mathrm{OD}(x,z) = -\ln\left[\frac{I_{\mathrm{at}}(x,z) - I_{\mathrm{dark}}(x,z)}{I_{\mathrm{ref}}(x,z) - I_{\mathrm{dark}}(x,z)}\right] \tag{3.2}$$

This equation is only valid in the low-intensity limit, as otherwise saturation effects become relevant and can affect the accuracy of the atom number estimation. The application of this equation is illustrated in figure 3.20, where the atomic cloud is easily discernible in the optical density graph.

From this two-dimensional array, we can extract the atom number of the imaged cloud through

$$N_{\mathrm{at}} = \frac{A}{\sigma_{eg}} \sum_x \sum_z \mathrm{OD}(x,z) \tag{3.3}$$

where A denotes the area that is imaged onto each pixel, which depends on the pixel size and the magnification of the optical imaging system.

During the time-of-flight, the atomic cloud undergoes a ballistic expansion. As the expansion dynamics depends on the temperature of the atomic sample, one can extract the temperature using such a time-of-flight scan measurement. The relation between the Gaussian width $\sigma_{x,z}$ and the temperature $T_{x,z}$ in a ballistic expansion at different times t is given by

$$\sigma_{x,z}^2(t) = \sigma_{x,z}^2(0) + \frac{k_B T_{x,z}}{m} t^2 \tag{3.4}$$

Here, k_B is the Boltzmann constant, m is the atomic mass, and $\sigma_{x,z}^2(0)$ represents the square of the initial Gaussian width. Consequently, the temperature of the atomic cloud can be obtained from a linear fit of $\sigma_{x,z}^2$ versus t^2.

Design considerations

When designing an imaging setup for our experiment, several critical parameters need to be considered to ensure optimal performance and accuracy in capturing atomic densities, which include:

- The **resolution** of the imaging system determines the size of the smallest details that can be differentiated within an image. In the experiment, we will be seeking to trap the atoms in a two-dimensional trap, with high trapping frequencies of several kHz along gravity-direction. Therefore, a spatial resolution of a few µm is required to accurately observe the trapped atoms. The resolution depends on the systems numerical aperture (NA), which is the spread of angles

the optical system can collect light from. A high NA requires small working distances and a large collection area, translating to a lens with a small focal length and a large diameter. The resolution of any imaging system, even when minimizing the effects of aberrations, is fundamentally limited by diffraction effects. The diffraction-limited resolution is described by the Rayleigh criterion [134], which is satisfied if the central maximum of one point emitter overlaps with the first minimum of the other. It is given by:

$$r = \frac{1.22\lambda}{2\,\mathrm{NA}} \tag{3.5}$$

where λ is the wavelength of the incident light.

- The **field-of-view** (FOV) is the area in the object plane that the imaging system captures. Depending on the application, we need two different FOVs. For optimization routines regarding the atom number and temperature in the initial stages like the magneto-optical trap, optical molasses, and magnetic trap, a high FOV imaging setup with a low magnification is required. On the other hand, once we load the atoms into the crossed optical dipole trap and reach the quantum degenerate regime, a high magnification is essential to capture fine details.

- There are quite a few **geometric constraints** that constrict the imaging system. Firstly, the chamber itself is 55 mm wide (in y-direction, including the glass viewports). With the additional vacuum flange and flange screws, this sets the minimal possible working distance to 40 mm. Furthermore, the optical access for the MOT and dipole beams has to be considered.

- The **wavelength** of the imaging light is chosen to be close to the resonance of the atomic transition being imaged. As we are dealing with an atomic mixture system, there are two wavelengths that need to be considered, 589 nm for sodium and 767 nm for potassium. The resulting chromatic focal shift (chromatic aberration) has to be taken into account for the design of the imaging system. Furthermore, since sodium and potassium imaging is carried out simultaneously, there is a need to efficiently combine and split the imaging light for the two species. This involves using dichroic mirrors to separate and direct the light to dedicated cameras for each species.

Considering the above points, we utilize two setups for absorption imaging, tailored

to different requirements. Firstly, a large field-of-view and low magnification imaging system with a single achromatic doublet lens[28] ($f_{\text{coarse}} = 180\,\text{mm}$) and a CMOS camera[29] enables the characterization of atomic clouds in the initial cooling stages. Secondly, a diffraction-limited, high-precision aspheric lens[30] with a diameter of 1 inch and a focal length of $f_{\text{fine},1} = 50\,\text{mm}$ serves as the primary lens for the high-resolution imaging setup. Compared to standard plano-convex lenses, this special aspheric lens is designed to eliminate spherical aberrations, enabling diffraction-limited performance. The size and focal length of the lens was determined as a compromise between retaining a relatively high numerical aperture and keeping enough optical access for the MOT and dipole beams. A 2 inch achromatic doublet lens[31] with $f_{\text{fine},2} = 1000\,\text{mm}$ is utilized as a secondary lens. A dichroic mirror[32] splits the two wavelengths, facilitating the compensation of the chromatic focal shift by adjusting the distance between the secondary lens and the camera independently for each species. An sCMOS camera[33] featuring a 2560×2160 pixel sensor and low-noise detection capabilities, as demonstrated in [135], is used for each species.

Characterization of the high-resolution imaging system

The initial design and evaluation of the planned high-resolution imaging system has been simulated using OSLO (Optics Software for Layout and Optimization). This process involved exploring various lens combinations and evaluating their performance using analysis tools such as the modulation transfer function or the optical path difference.

For the two-lens setup with $f_{\text{fine},1} = 50\,\text{mm}$ and $f_{\text{fine},2} = 1000\,\text{mm}$, we achieved a *Strehl ratio* of 0.8 (0.74) for sodium (potassium). The Strehl ratio, representing the intensity at the central peak of the point spread function normalized to an ideal Airy diffraction pattern, is a key parameter in determining the performance of an optical system. According to the *Maréchal criterion*, an optical system can be described as diffraction-limited if this quantity exceeds a value of 0.8. Thus, our lens system is expected to achieve close to diffraction-limited performance. Moreover, by minimizing the optical path difference for the final focus, the distance between the secondary lens and the camera was found to be 1006 mm (900 mm) for sodium (potassium).

[28] Thorlabs AC508-180-AB
[29] Mako G-030B
[30] Thorlabs AL2550H
[31] Thorlabs ACT508-1000-A/B
[32] LensOptics custom
[33] Andor Zyla 5.5

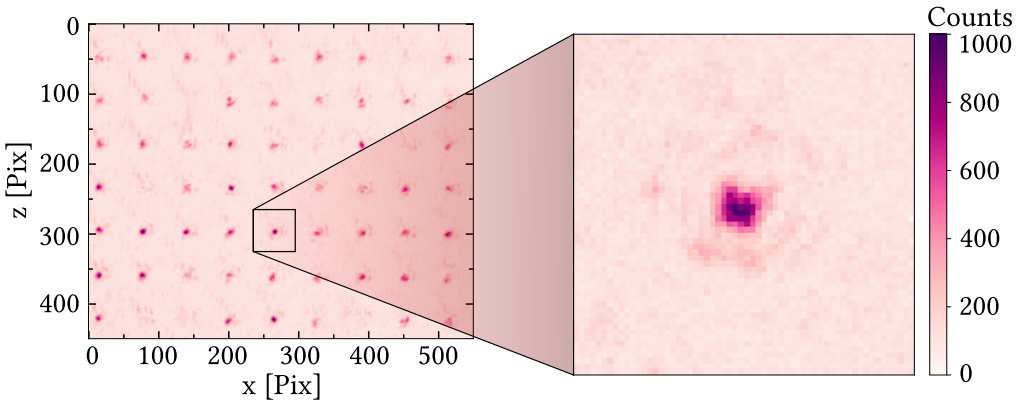

Figure 3.21.: Image of the gold grating illuminated with sodium laser light, which is used to experimentally characterize the resolution of the imaging setup.

The experimental evaluation of the imaging system's performance is critical to ensure that it meets the expected specifications and requirements for the experiment. The use of a test target, in this case a gold foil [136] with a grid of equidistant holes each with a diameter of 650 nm and a spacing of 20 µm, allows for a controlled and systematic assessment of the imaging quality.

Notably, the gold foil with its grid of equidistant holes introduces some complications due to near-field diffraction effects. The gold foil acts as a periodic grating, where the image of the grating is reproduced at regular distances from the grating. This diffraction effect is called the *Talbot effect* [137]. To ensure that the grating is positioned in the true focal plane of the imaging lens, we can make use of some additional bigger rectangular holes at the edges of the gold foil. Consequently, we adjust the grating to get a sharp image of such a rectangular hole and subsequently translate the grating in the xy-plane to recover the image of the grating[34] [136, 138].

By uniformly illuminating the test target with a collimated laser beam at the chosen wavelength (589 nm or 767 nm), we simulate the actual experimental conditions as closely as possible. Placing a glass plate[35] made from the same material as the viewport (N-BK7) at a distance of 21.5 mm from the test target replicates the experimental conditions, providing valuable insights into how the imaging system will function under real circumstances.

The image of the pattern is subsequently collimated with the objective lens $f_{\text{fine},1}$ and finally focused onto the camera chip using the achromatic doublet lens $f_{\text{fine},2}$. Figure 3.21 displays a camera image of the test pattern, which was illuminated with sodium

[34] The subsequent translation of the gold foil can introduce an additional source of error in case the grating is not mounted perfectly straight.

[35] Edmund Optics 34-430

light (589 nm), revealing the periodic intensity pattern. The close-up image of the transmission through a single hole offers a detailed view of the imaging quality, showcasing the system's ability to resolve small features.

To characterize the resolution of this setup, we extract the integrated x- and y-profiles of the different holes in the test pattern and fit the Airy disc intensity distribution [138]

$$I(r) = I_0 \left[\frac{2\, J_1\left(\frac{1.22\pi}{\Delta x} x\right)}{\frac{1.22\pi}{\Delta x} x} \right]^2 + I_{\text{offset}} \tag{3.6}$$

to this data, where I_0 denotes the peak intensity and Δx is the resolution based on the Rayleigh criterion.

The experimental procedure involves varying the z-position of the gold foil (distance between gold foil and glass plate) using a linear translation stage, capturing the intensity profiles, and performing the fitting and analysis routine for both sodium and potassium light. Resolution and maximum intensity for each position is displayed in figure 3.22. The position of optimal focus is characterized by a minimum in the res-

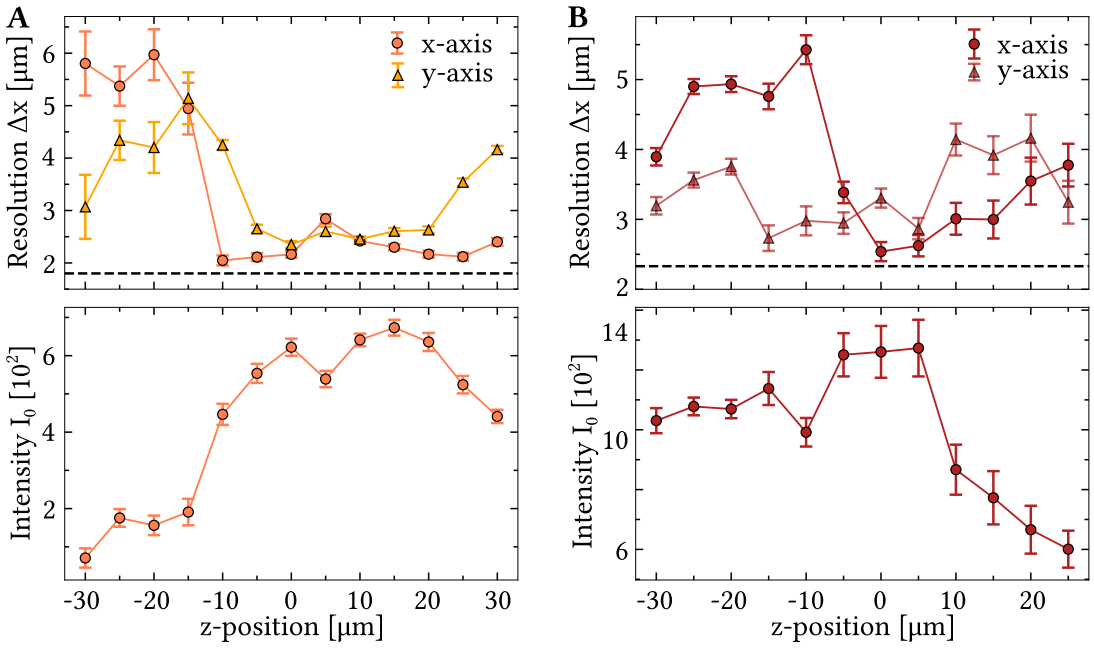

Figure 3.22.: Characterization of the high-resolution imaging system using a gold grating as a test pattern. The graphs show the width Δx and peak intensity I_0 of the Airy disc patterns for sodium (A) and potassium light (B) as a function of the z-position of the test target. The black dashed line represents the diffraction-limited resolution.

olution and a maximum in the peak intensity. Both sodium and potassium imaging setups perform close to the diffraction limit of $r_{Na} = 1.80\,\mu m$ and $r_K = 2.34\,\mu m$, indicated by the dashed black lines. However, we observe a very broad minimum in the resolution, featuring a slight asymmetry that could be caused by spherical aberrations. In the presence of such aberrations, the different light rays do not intersect after the lens in one focal point, but are refracted more or less depending on how far off-centre the rays are. This can lead to a broadening of the feature and to the appearance of fringes around the main peak, that are visible in figure 3.21 and negatively affect the fitting routing. Furthermore, the analysis also suffers from a low signal-to-noise ratio observed for some point sources in the gold foil.

Optical layout

The optical layout of the implemented absorption imaging system is illustrated in figure 3.23. Everything centres around the atomic cloud, which is positioned in the

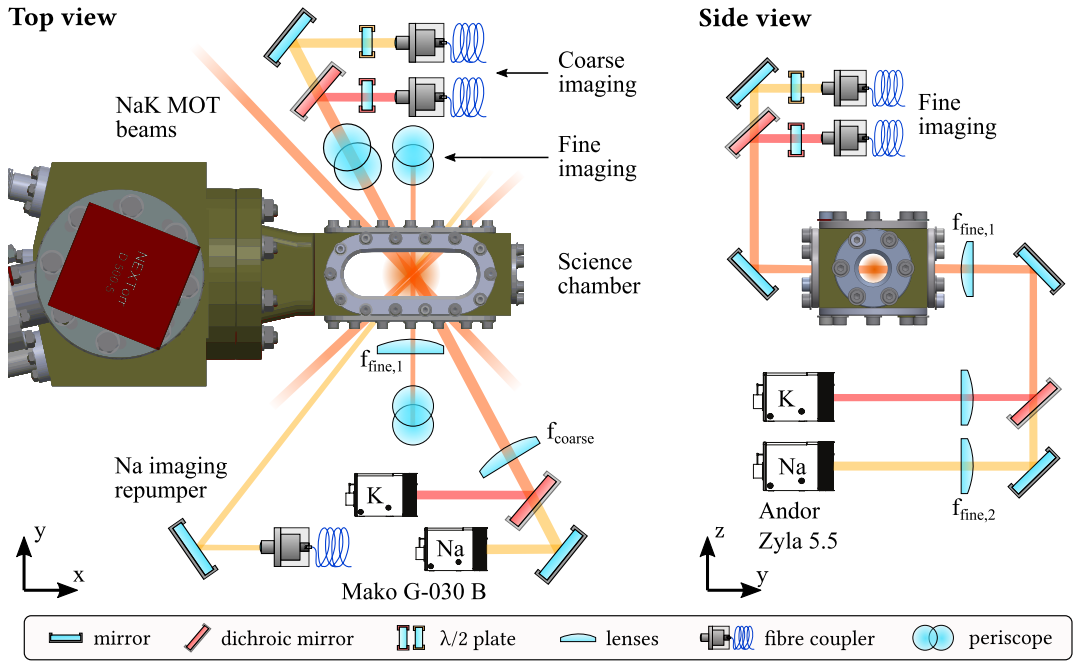

Figure 3.23.: Optical layout for absorption imaging in the horizontal plane. Views from the top and the side show the high field-of-view (coarse) and high-resolution (fine) imaging setups. The absorption beams for sodium and potassium are superimposed on a dichroic mirror and directed onto the atomic cloud. The transmitted light is imaged onto dedicated cameras for each species. Sodium requires an additional repumping beam for imaging, as the absorption beam only possesses cooling light.

centre of the science chamber. As the space in the horizontal plane is already quite congested from the MOT beam splitting optics, we utilize periscopes to move out of this plane. For sodium, a dedicated repumping beam is employed pumping the $|F = 1\rangle$ atoms back into the cooling cycle. To simultaneously image both the sodium and potassium clouds, the absorption beams are combined and split using a dichroic mirror and then focused onto a dedicated camera for each species.

The coarse imaging setup uses a single-lens configuration with a focal length of $f_{\text{coarse}} = 180\,\text{mm}$. The distance to the image plane is 260 mm, resulting in a theoretical magnification of $M_{\text{coarse}} = 0.44$.
For an independent verification, we also experimentally extracted the magnification of this setup using time-of-flight measurements of the potassium grey molasses, which is further described in section 5.2. By turning off the trap and allowing the atoms to fall, multiple images were captured at different flight times to map out the free fall. Assuming a constant acceleration due to gravity of $g = 9.81\,\text{m/s}^2$, the experimentally extracted magnification for the coarse imaging setup was found to be $M_{\text{coarse,exp}} = 0.445(2)$, in good agreement with the value obtained from rough distance measurements. In the image plane, a dedicated CMOS camera[36], equipped with an optical filter[37] that blocks any unwanted stray light, captures the absorption of the respective atomic species.

To achieve high-resolution imaging for the atoms in the dipole trap, a different imaging setup is employed (see figure 3.23). Similar to the high field-of-view imaging, the fibre out-couplers for sodium and potassium are located on a vertically higher platform. The 1 mm collimated laser beams are overlapped on a dichroic mirror and then translated to the atom plane using a periscope. After passing through the chamber and getting absorbed by the atoms, the light passes through the objective lens mounted close to the science chamber side viewport, ensuring that the atoms are in the focal plane of this lens. The beam is then translated downward with another periscope, where we eventually split the beams and focus them onto dedicated sCMOS cameras[38] using the secondary lenses. All three lenses are mounted on linear translation stages to adjust and optimize the focus position.
We measured the magnification of this setup in a similar way as for the coarse imaging,

[36] Mako G-030B
[37] Edmund Optics 65-162 for sodium and 65-177 for potassium
[38] Andor Zyla 5.5

but now using the sodium BEC. By taking images of the atomic cloud at different time instances, we mapped out the atoms' free fall, as shown in figure 3.24. While a slight expansion of the cloud can be observed, more noticeably the mean z-position of the atoms changes in a quadratic fashion. From a fit to the parabolic trajectory, we can acquire the imaging magnification for the horizontal fine imaging as $M_{\text{fine}} = 20.36(3)$.

Table 3.5 summarizes the characteristics of the two employed absorption imaging setups in the horizontal plane.

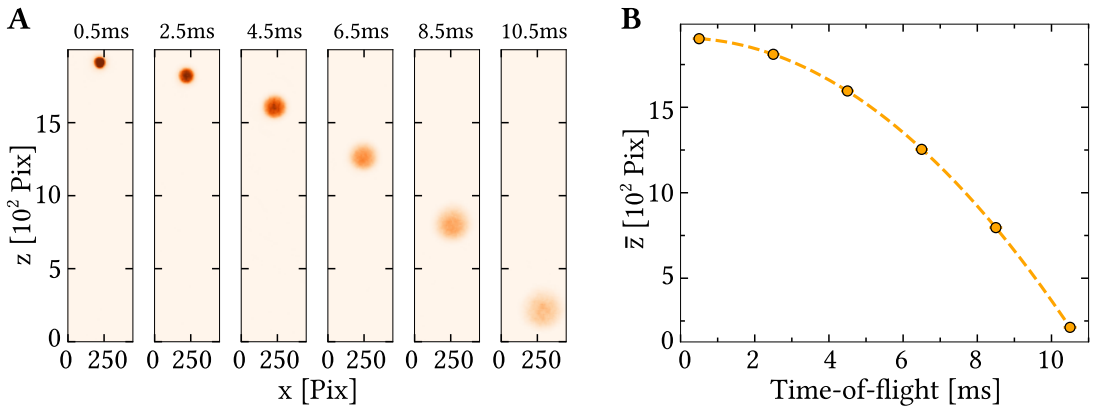

Figure 3.24.: Measurement of the magnification of the high-resolution imaging system using a time-of-flight scan of the sodium BEC in free fall. A: Absorption images of the sodium BEC for different time-of-flight settings with the z-axis along gravity direction. B: Mean z-position of the sodium cloud as a function of time-of-flight. The free fall due to gravity, which is visible from the quadratic dependence, is fitted using the dashed line, enabling the extraction of the imaging magnification (see the main text).

Table 3.5.: Summary of characteristics for the coarse, high FOV, and the fine, high-resolution horizontal imaging setups. The magnification of the two imaging systems was extracted through time-of-flight scans of the potassium grey molasses and the sodium BEC, respectively.

	Coarse imaging	Fine imaging
Camera	Mako G-030B	Andor Zyla 5.5
Sensor format	644 × 484	2560 × 2160
Pixel size [µm]	7.4	6.5
Lenses focal length [mm]	180	50, 1000
Magnification	0.445(2)	20.36(3)

Imaging sequence

At the end of each experimental sequence, we perform a destructive imaging process, constituting our measurement. As depicted in figure 3.25, we turn off the trap and wait for a specific time, which we denote as the time-of-flight (TOF), during which the cloud can freely expand. As mentioned before, the temperature of the atomic cloud can be extracted through a scan of this parameter. Following the time-of-flight, the three images, with which we reconstruct the atomic density profile, are recorded.

Firstly, while the atoms are still present, we pulse the imaging beam for 20 µs using an RF-switch[39] that triggers the AOM. At the same time, we expose the camera to capture the atomic absorption in this initial image. While for potassium, the absorption beam contains both cooling and repumping light, the sodium beam only has cooling light. However, given that we are working with atoms in the $|1, -1\rangle$ hyperfine ground state, which is not addressed by the cooling light, a separate repumping beam is employed, as demonstrated in figure 3.23. This beam is triggered in unison with the cooling light.

[39] Mini-Circuits ZASWA-2-50DRA+

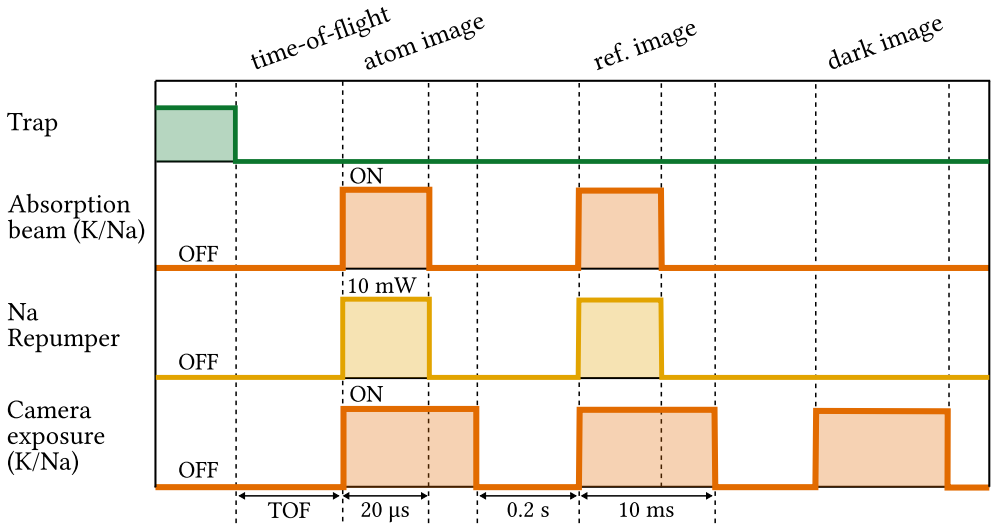

Figure 3.25.: Timing sequence for absorption imaging of sodium and potassium. After a time-of-flight, three pictures are taken. For the first two images, the absorption beam is turned on for 20 µs. For sodium, the imaging beam only possesses cooling light, such that an extra repumping beam is required to pump the $|1, -1\rangle$ atoms into the cooling/imaging cycle. This additional beam is triggered simultaneously with respect to the absorption beam. The last image, where the absorption beam is turned off, serves for the subtraction of any possible stray light.

Subsequently, after a 200 ms delay to ensure that there are no atoms left any more, we repeat the pulsing of the AOM and triggering of the camera. This results in a reference image containing only the signal from the imaging light (no atoms). Following an additional 200 ms waiting period, we exclusively expose the camera to obtain the dark frame, effectively eliminating any stray light that might hit the camera sensor.
From these three images, we compute the optical density and subsequently calculate the atom number of the cold atomic sample according to equation 3.3. The sodium and potassium absorption beams and camera exposures are triggered simultaneously.

Imaging problems and solutions

Lastly, I want to discuss some challenges we faced with imaging and how we have either dealt with them or plan to in the future.
For quite some time, we were using an EOM to generate the repumping sideband for the imaging beam. The RF power, supplied to the EOM, allowed us to control the intensity ratio between the cooler and repumper. However, we observed that we were limited in the repumper power, due to the unwanted sideband. This limitation proved especially detrimental when trying to image atoms in the $|1,-1\rangle$ hyperfine ground state. Consequently, we decided to utilize a separate repumping beam by branching off light from the quadruple-pass AOM path, which provided an independent control of the cooling and repumping intensities.

Secondly, the objective lens for fine imaging has to be mounted very close to the science chamber because of the short working distance. To bridge the 25 cm gap to the large U-shaped breadboard, the lens is secured inside an extended 1 inch aluminium lens tube. The fact that the lens tube is only fixated on one side creates a substantial lever, introducing instabilities into the setup. Moreover, the presence of aluminium between the magnetic field coils is not ideal, as induced eddy currents can disrupt the magnetic field experienced by the atoms. For these reasons, we intend to replace the aluminium tube with a PEEK tube, properly secured to the breadboard to enhance the stability of the system.

Moreover, as eluded to earlier, when imaging dense atomic clouds well above saturation intensity using absorption imaging, saturation effects need to be considered. Following the approach introduced by Reinaudi et al. [139], equation 3.2, which describes the calculation of the optical density based on the measured intensities, is modified. An additional factor, proportional to the difference between the atom intensity and the

reference intensity, is added, requiring a calibration to determine the proportionality factor. Notably, the atom number estimates presented in this thesis do not account for this extra term. Consequently, the reported values will likely underestimate the true atom number in the imaged atomic cloud.

With the current scheme, absorption imaging can be performed effectively at low magnetic fields. However, an increase in the magnetic field induces shifts in the magnetic sub-levels due to the linear Zeeman effect. Moreover, as the magnetic field is further increased, the system enters the Paschen-Back regime, requiring substantial modifications to the imaging frequency. Furthermore, for moderate magnetic fields, in a region where the mixture of ^{23}Na-^{39}K exhibits favourable scattering properties, the optical cycling transitions are no longer strictly closed. Therefore, absorption imaging at high/intermediate magnetic fields requires an adapted optical pumping scheme, as further elaborated on in [140] for the case of potassium.
The implementation of such an improved imaging scheme, possessing the flexibility of operating at both low and high magnetic fields, would be beneficial for this mixture experiment. Currently, following the cooling sequence, it is necessary to sweep to zero magnetic field, crossing inter- and intra-species Feshbach resonances, resulting in atom loss. In contrast, adopting this high field imaging approach would eliminate the need for additional ramps, allowing immediate high signal to noise imaging at the set magnetic field. Consequently, we are already actively working on implementing this imaging process for potassium and are looking into possibilities for extending this scheme for sodium.

Conclusion

In this chapter, we have introduced the necessary tools to cool and trap our sodium potassium mixture. Specifically, we have detailed the operation of individual laser systems that emit light at the correct wavelength, which is subsequently split, frequency-shifted, and transported to the main experiment table using optical fibres. On the experiment table, this light is used to cool, transport, and image the cold atoms.
In addition to the velocity-dependent cooling force generated by the lasers, a spatially dependent force is required to confine the atoms within a magneto-optical trap (MOT) or magnetic trap. This confinement is accomplished by establishing a magnetic field gradient through the utilization of magnetic field coils configured in an anti-Helmholtz arrangement. As we also need bias magnetic fields to tune the Feshbach resonances

in the latter stages of the experimental sequence, we implemented an H-bridge setup to switch the current direction through one coil stack. This configuration enables the achievement of magnetic field gradients up to approximately 300 G/cm and bias fields reaching 600 G.

Finally, each experimental sequence is concluded by a destructive detection method. We set up a high field-of-view coarse absorption imaging system with a magnification of 0.445(2), essential particularly in the early cooling stages when characterizing and optimizing the MOT, molasses, and magnetic trap with respect to atom number and temperature. For imaging the BEC in the crossed optical dipole trap and eventually within a two-dimensional optical trap, we incorporated a high-resolution imaging system in the horizontal plane, featuring an imaging magnification of 20.36(3) and achieving near diffraction-limited resolution.

CHAPTER 4

First step: Cooling sodium to degeneracy

Our primary objective is to set up a mixture experiment, with our initial focus directed towards sodium. This choice was motivated from its intended role as a sympathetic coolant for potassium. Consequently, a single-species ^{39}K-BEC is not required, whereas we do need to reliably condense the sodium atoms. This preliminary step enables the subsequent addition of potassium and facilitates the cooling of the mixture to achieve dual-species degeneracy.

This chapter outlines the sequential stages involved in the cooling process for sodium, as schematically depicted in figure 4.1. Firstly, in section 4.1, I will introduce the magneto-optical trap (MOT), which represents the first cooling stage and a cornerstone of every cold atom experiment. Following this, the atoms are transferred from the MOT to a quadrupole magnetic trap, where a microwave evaporation stage is performed to further reduce the temperature and increase the phase-space density of the atomic cloud (see section 4.2). Subsequently, the atoms are loaded into a far-red detuned crossed optical dipole trap. Section 4.3 comprehensively discusses this optical trap, culminating in the characterization of the Bose-Einstein condensate of sodium. This condensate is obtained after forced evaporative cooling within the dipole trap.

4.1. Sodium magneto-optical trap

A standard magneto-optical trap (MOT) employs counter-propagating red-detuned circularly-polarized laser beams along the three spatial directions. These MOT beams induce cooling of atoms through a mechanism called Doppler cooling, wherein atoms absorb and spontaneously re-emit photons from the laser beams, thereby losing ki-

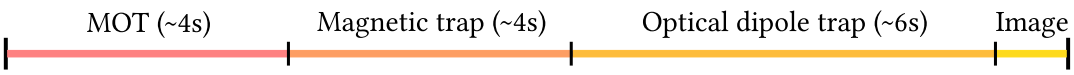

Figure 4.1.: Sketch of the experimental sequence, illustrating the various cooling and trapping stages, as well as the subsequent destructive imaging process.

netic energy. The position-dependent trapping force in a MOT is generated by an external magnetic field gradient, which confines the cooled atoms [141–143].
As outlined in the previous chapter, the MOT beams generally carry both D2 cooling light $|F = 2\rangle \rightarrow |F' = 3\rangle$ and repumping light $|F = 1\rangle \rightarrow |F' = 2\rangle$, as off-resonant excitations could otherwise remove atoms from the MOT cycling transition.
The efficiency and performance of the magneto-optical trap are influenced by several parameters:

- **Beam alignment:** Achieving optimal cooling and trapping requires precise alignment of the six MOT beams. The intersection point of these beams within the chamber should align with the magnetic field zero position. Additionally, the counter-propagating beams need to overlap on both sides of the chamber. As an initial alignment guide, we used paper masks with appropriately positioned holes, placing them on the viewports, and beam-walking the individual beams.

- **Power balancing:** The intensity of the counter-propagating beams must be balanced to equalize the cooling forces in the two directions. To achieve this balancing, half-wave plates mounted in precision rotation mounts are utilized in combination with polarizing beam splitters to control power distribution. In total, the cooling beams carry 55 mW of light, while the repumper beam's power is set at 5 mW. Both beams are collimated to a diameter of 15 mm, allowing them to pass precisely through the side-viewports of the science chamber.

- **Polarization:** The MOT beams have to be circularly polarized, with the horizontal beams requiring left-handedness and the vertical beams right-handed circular polarization[1]. A 1 inch achromatic quarter-wave plate[2] is used for each beam, converting the linear polarization from the PBS output to circular polarization. Achromatic wave plates are used to accommodate both sodium and potassium light. The polarization of the light is set by rotating this wave plate and measuring it directly in front of the chamber with a polarization analyser[3].

- **Frequency detunings:** The light used for MOT operation, comprising both cooling and repumping light, requires red-detuning with respect to the atomic resonance frequency. This red-detuning is crucial to slow down the atoms and

[1]The polarization handedness depends on the coil configuration.
[2]Thorlabs AQWP10M-580
[3]Schäfter + Kirchhoff SK010PA

effectively trap them. The detuning can be adjusted by changing the RF-frequency supplied to the AOM and is set to −14 MHz for the cooling light and −7 MHz for the repumping light.

- **Magnetic field gradient:** The spatial extent and stability of the trap are influenced by the gradient of the magnetic field. This gradient determines the strength of the trapping forces and the volume within which the atoms are confined. An optimal magnetic field gradient of 8.6 G/cm [4] has been identified as suitable for both sodium and potassium, ensuring effective trapping.

- **Magnetic offset fields:** The offset coils create small bias fields of a few Gauss to compensate for external stray magnetic fields, including the Earth's magnetic field. Moreover, the current running through these coils can be adjusted in order to move the zero position of the magnetic gradient field, which becomes especially relevant for the optical molasses.

The performance of the sodium MOT concerning these parameters can be evaluated utilizing the fluorescence of the MOT. We monitor the integrated fluorescence signal on a dedicated amplified photodiode, providing an estimate of the total number of trapped atoms. In addition to the steady-state fluorescence counts, the atom loading rate is of particular importance. This rate is determined by triggering the shutter, which controls the MOT beams, offering a quantitative metric for adjusting power settings and frequency detunings in the 2D- and 3D-MOT, thereby serving as a valuable optimization tool.
An advantageous aspect of using sodium is the wavelength of the fluorescent light, which is approximately 589 nm. This specific wavelength allows for easy visual observation of the cold atomic cloud by the naked eye, facilitating the qualitative optimization of the beam alignment.

Dark SPOT MOT

One major issue concerning a MOT is the fact that the maximum achievable atomic density is limited by two processes. Firstly, light-assisted collisions between ground state and excited state atoms result in atom loss from the trap [144]. Secondly, the reabsorption of scattered light generates repulsive forces, limiting the attainable density within the MOT [145].

[4] The corresponding analog channel of our experimental control system is set to 0.26 V to achieve this magnetic field gradient.

To overcome these limitations, the concept of a *dark SPOT MOT* was introduced by Ketterle et al. [146]. The dark SPOT MOT maintains atoms at the centre of the trap in a dark hyperfine ground state, effectively isolating them from the detrimental effects of repumping light. By using only cooling light in the MOT beams and implementing a spatial mask to block the separate repumper beam in the central region, the atoms in the centre accumulate in the $|F = 1\rangle$ dark state and do not interact with the cooling light any more. This reduction in re-scattering events allows for the achievement of higher atomic densities.

On the main experiment table, we collimate the repumping beam to a diameter of 15 mm and then insert a transparent glass plate with a black disc in the centre into the beam path, creating a hollow repumping beam by blocking its central part. The diameter of the dark SPOT was optimized to 6 mm to ensure an efficient transfer of atoms into the subsequent magnetic trap, a critical step in the cooling process.
To optimize the dark-SPOT MOT with respect to atom number and loading rate, we initially adjusted beam alignment and power balancing while observing the bright MOT[5]. After adding the dark-SPOT, a script-based optimization procedure was adopted, utilizing absorption images to quantitatively measure the atom number within the dark-SPOT MOT.

While the underlying principles of a dark SPOT MOT are clear and its execution improves the transfer into the magnetic trap, our current implementation has room for improvement. Firstly, using a Gaussian laser beam and blocking its central part with a black disc effectively discards the most intense parts of the laser beam. An alternative approach involves reshaping the intensity distribution using an axicon lens, as described in [147], to create a hollow laser beam.
Secondly, by simply placing a black disc into the repumping beam, we observe diffraction effects making the dark SPOT not entirely dark at the position of the atoms. A more effective approach, in line with other ultracold sodium experiments [148–151], entails imaging the dark SPOT with a 1:1 telescope onto the MOT.

MOT loading

To evaluate the difference between the bright and dark SPOT MOT, the loading rate can be used as a quantitative figure of merit. The process of loading N atoms into a

[5]For the bright MOT, we simply remove the glass plate with the black disc from the repumping beam path.

magneto-optical trap can be described by the following rate equation [152, 153]:

$$\frac{dN(t)}{dt} = L - \alpha\, N(t) - \beta\, N(t)^2 \tag{4.1}$$

where L represents the loading rate, α describes the one-body loss rate due to collisions with the background gas, and β accounts for the two body-loss resulting from collisions between sodium atoms within the MOT. The solution to this differential equation with the initial condition $N(0) = 0$ is given by:

$$N(t) = \frac{\sqrt{\delta}}{2\beta} \tanh\left[\frac{\sqrt{\delta}\, t}{2} + \operatorname{arctanh}\left(\frac{\alpha}{\sqrt{\delta}}\right)\right] - \frac{\alpha}{2\beta} \tag{4.2}$$

where the loading rate is defined as $L = (\delta - \alpha^2)/4\beta$, and $N_{\text{sat}} = (\sqrt{\delta} - \alpha)/2\beta$ describes the stationary atom number in the steady state.

In figure 4.2, the loading curves for the sodium bright and dark SPOT MOT are presented. These data sets were obtained using the coarse absorption imaging setup described in section 3.4. The dashed lines in the figure represent fits of the loading curves, taking into account intra-MOT collisions, according to equation 4.2.

The dark SPOT MOT exhibits a loading rate of $2.9(1) \times 10^8$ atoms/s, reaching a steady-state atom number of $2.49(1) \times 10^8$ atoms. Consequently, a loading time of 4 s is sufficient for the sodium dark SPOT MOT. In contrast, intra-MOT collisions limit the atomic density in the bright MOT, causing the atom number to saturate after only about 0.5 s to a value of $0.61(8) \times 10^8$ atoms.

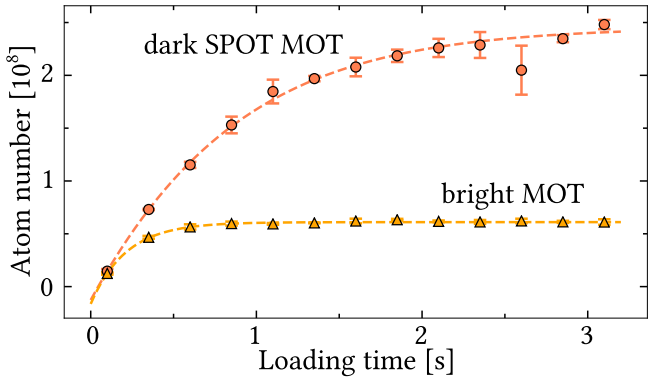

Figure 4.2.: Loading rate measurement of bright and dark SPOT sodium MOT. The dashed lines represent loading curve fits to the experimental data using equation 4.2.

Experimental sequence

The experimental sequence is initiated by heating a 1 g ingot ampoule containing sodium to a temperature of approximately 170 °C. The thermal atoms effusing from the oven are subsequently pre-cooled in a two-dimensional magneto-optical trap (2D-MOT). Further details on the design and characterization of this cold atom source can be found in [126].

Following pre-cooling, the atoms are transported into the science chamber using a near-resonant push beam. In the science chamber, the atoms are re-trapped in a dark SPOT MOT. A simplified schematic representing this experimental sequence is displayed in figure 4.3. For the initial MOT loading, both the magnetic field gradient and the 3D-MOT beams (cooler and repumper) are turned on. This step marks the initiation of the MOT operation, effectively beginning the cold atom trapping process.

After 4 s of MOT loading, the atoms are optically pumped to the $|F = 1\rangle$ hyperfine ground state by turning off the repumping beam and keeping the cooling beam on for a duration of 200 µs. During this period, only the cooling beam is active, driving the transition $|F = 2\rangle \rightarrow |F' = 3\rangle$, resulting in the accumulation of atoms in the $|F = 1\rangle$ ground state due to off-resonant excitations. Following the optical pumping process, the cooling light is also turned off, and the atoms are transferred to the magnetic trap, as discussed in the next section. At the end of the MOT cooling stage, we have roughly 2×10^8 atoms at a temperature of approximately 200 µK.

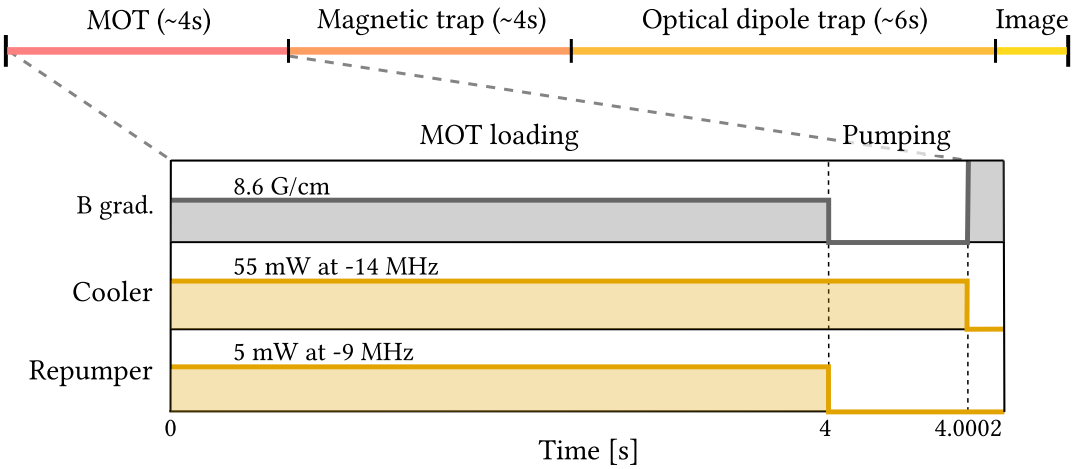

Figure 4.3.: Sketch of the sodium MOT experimental sequence. The MOT is loaded for 4 s in dark SPOT configuration, after which the atoms are pumped for 0.2 ms to the $|F = 1\rangle$ ground state.

Typically, the initial MOT stage is followed by a sub-Doppler cooling phase (optical molasses) [154, 155] to further reduce the temperature of the atomic cloud below the Doppler limit. However, in the case of sodium in single-species configuration, incorporating this additional cooling stage did not initially yield a significant improvement in the phase-space density. This was attributed to imperfections in beam balancing and challenges in compensating stray magnetic fields.

In contrast, when the experimental focus shifted to working with potassium, a more advanced cooling technique called grey molasses cooling was implemented for potassium atoms (see section 5.2). In this process, magnetic stray field compensation was improved using microwave-spectroscopy, and the beam alignment was adjusted. These improvements allowed the successful implementation of a molasses cooling stage for sodium as well, achieving temperatures as low as 60 µK during dual-species operation[6].

Laser cooling techniques, such as those employed in the MOT, rely on the principle of directional absorption and isotropic emission of photons. When an atom absorbs a photon, it receives a momentum kick in the direction of the incident light's propagation. Due to the isotropic nature of the spontaneous emission, the net force exerted on the atom will oppose its motion. Consequently, the lowest achievable temperatures using this cooling technique are constrained by the minimum momentum kick an atom can receive when it absorbs and emits a single photon. This limit is referred to as the *recoil limit* and typically corresponds to temperatures of a few µK or velocities of $v_r \approx 1\,\mathrm{cm/s}$ [143].

To further reduce the temperature of the atomic sample, the atoms must be transferred into a conservative trapping potential that does not rely on photon scattering, as is the case in a magnetic trap. In such a trap, a different cooling technique, which will be discussed in the following section, can be implemented.

4.2. Magnetic trap and microwave evaporation

The magnetic quadrupole trap, pioneered by Migdall et al. [156], operates based on the Zeeman interaction between the permanent magnetic moment of neutral atoms $\vec{\mu}$, and an inhomogeneous magnetic field $\vec{B}(\vec{r})$. Assuming that the atom's magnetic moment

[6] We are considering implementing a D1 grey molasses scheme for sodium alongside the potassium method described in section 5.2.

is aligned with the magnetic field, the trapping potential is given by

$$V_{\text{mag}} = -\vec{\mu}\,\vec{B}(\vec{r}) = -g_F m_F \mu_B B \tag{4.3}$$

where g_F is the Landé g-factor, m_F is the magnetic quantum number, and μ_B represents the Bohr magneton. The trapping behaviour is dictated by whether the product $m_F g_F$ is positive or negative. Atoms with $m_F g_F < 0$ are repelled by high magnetic field amplitudes and are termed *low-field seekers*, while those with $m_F g_F > 0$ are attracted to magnetic field maxima and are known as *high-field seekers*. The magnetic trap relies on the trapping of low-field seekers in a local magnetic field minimum of the quadrupole potential, effectively repelling atoms in high-field seeking states.

In the context of sodium and potassium (^{39}K), the magnetically trappable states for the ground states are $|2,1\rangle$, $|2,2\rangle$, and $|1,-1\rangle$[7]. Hence, optical pumping to the correct spin state prior to transferring atoms into the magnetic trap is essential. While the state $|2,1\rangle$ is unstable against spin-exchange collisions, making it unsuitable, sodium atoms can be condensed in the $|2,2\rangle$ state, as first demonstrated in [157]. However, this requires efficient optical pumping and spin purification to eliminate undesired atoms in the $|2,1\rangle$ state[8]. Consequently, the $|1,-1\rangle$ state was chosen for its robustness and simplicity.
Ideally, complete transfer of atoms to the $|1,-1\rangle$ spin state via spin polarization is desired. However, this technique is less effective for sodium, achieving transfer efficiencies of only around 35 % [158] due to high atomic densities present in the dark SPOT MOT and the small frequency separations of possible transitions. Higher transfer efficiencies, up to approximately 75 %, have been reached [159, 160], but require strong magnetic bias fields up to 100 G. As this exceeds the capabilities of our offset coils, we do not spin-polarize the atoms prior to magnetic trap loading. Instead, optical pumping of atoms to the $|F = 1\rangle$ hyperfine ground state is carried out by turning off the repumper and only shining cooling light for 200 µs, as described in the previous section. Subsequently, the atoms populate the three m_F states with equal probability, resulting in a maximum achievable transfer of atoms into the magnetic trap of 1/3.

Another critical factor for a successful transfer is the alignment and overlap of the MOT position with the location of the magnetic trap minimum. Poor mode-matching

[7] In this thesis, we use the notation $|F, m_F\rangle$ to denote the different spin states (if not specified otherwise).
[8] We attempted spin polarization to the $|2,2\rangle$ stretched state, but faced challenges with low optical pumping efficiencies, as outlined in section 5.1.

between the two traps can lead to additional heating and subsequent atom loss. We optimized this overlap through a two-stage process. In the first step, the fluorescence of the bright MOT was observed while sinusoidally modulating the magnetic field gradient, providing an initial estimate for the magnetic trap location. Beam alignment and power balancing were then adjusted to maintain isotropic expansion and compression of the cloud. The second stage involved looking directly at the atom absorption signal in the magnetic trap, loaded from the dark SPOT MOT, and optimizing this signal with respect to atom number and temperature.

Depending on the elastic collision rate, the evaporative cooling stage in the magnetic trap, which is the subject of the following subsection, typically lasts several seconds. Therefore, it is imperative to ensure a sufficient lifetime of sodium atoms in the magnetic trap. The dominant mechanism of atom loss within the magnetic trap stems from collisions between sodium atoms and the background gas.

A lifetime measurement was conducted to analyse the dependence of the sodium atom number on the hold time in the magnetic trap, specifically at the usual operation gradient of 300 G/cm. Figure 4.4 illustrates the results of this measurement. To obtain this data, atoms were transferred from the MOT to the magnetic trap following an optical pumping stage. Subsequently, the atoms were held in the magnetic trap for a variable hold time. After this period, the magnetic field was turned off, and the atoms were imaged using the coarse absorption imaging system following a short time-of-flight of 0.1 ms. An exponential decay curve fitted to the experimental data yields a lifetime of $\tau = 20.4(5)$ s. Consequently, the relative atom loss attributed to undesired

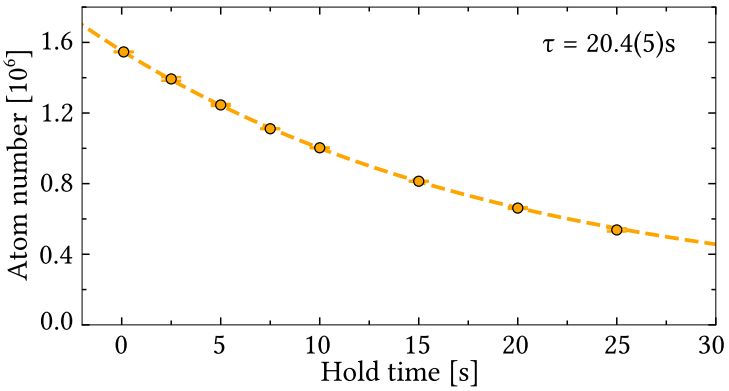

Figure 4.4.: Lifetime measurement of sodium atoms in the magnetic trap. An exponential atom-loss curve is fitted to the data resulting in a trap lifetime $\tau = 20.4(5)$ s.

collisions with the background gas during the entire magnetic trap stage, which lasts approximately 4 s, is only about 15 %.

Microwave evaporation

In the magnetic trap, we perform microwave evaporation to selectively evaporate the sodium atoms. In the context of single-species operation, the well-established RF-induced evaporation technique [161, 162] could be applied. However, given the dual-species nature of this experiment involving both sodium and potassium, the emphasis is placed on selectively evaporating sodium atoms. Due to the thermal contact between the species, the cold sodium atoms then act as a buffer, sympathetically cooling down the potassium atoms while maintaining a constant population.

To implement this selective evaporation technique, particular attention is given to the ground state hyperfine splitting of both sodium and potassium. The hyperfine splitting is approximately 1771 MHz for sodium and 461 MHz for potassium at zero magnetic field.

Figure 4.5 shows a schematic depiction of the energy level splitting of the hyperfine ground states in the presence of a magnetic field gradient. The Zeeman effect causes the different magnetic sub-levels to shift linearly in energy. Within the magnetic trap, the magnetic field gradient induces a spatially-dependent energy shift. As previously mentioned, atoms are trapped in the low-field seeking $|1, -1\rangle$ state. The most ener-

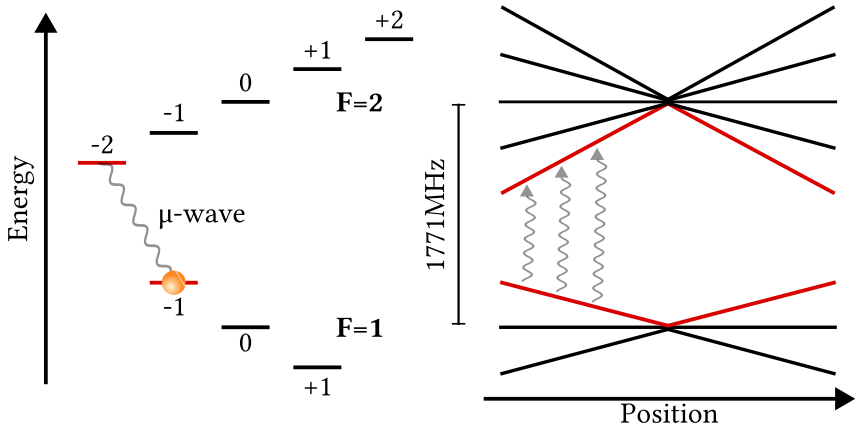

Figure 4.5.: Schematic diagram illustrating the microwave evaporation method for cooling sodium atoms. Within the magnetic trap, the magnetic sub-levels are shifted due to the Zeeman effect. The microwave transitions from $|1, -1\rangle$ to $|2, -2\rangle$ are depicted as grey wiggly arrows. Figure adapted from [163].

getic atoms tend to follow trajectories that take them further away from the magnetic field minimum, leading them into regions with larger magnetic field values. Consequently, a microwave pulse at 1700 MHz can be used to transfer these highly energetic atoms to the anti-trapped $|2,-2\rangle$ state, effectively removing them from the trap. Subsequently, the microwave frequency is linearly increased to 1760 MHz, continuing this evaporation process. During this process, hot atoms are ejected from the trap, while the remaining atoms undergo collisional re-thermalization at a lower temperature.

The microwave signal required for the evaporation procedure is generated using a signal generator[9] capable of delivering frequency sweeps with a bandwidth of 3 GHz. This signal generator is remotely controlled by a PC via a GPIB interface, enabling efficient programming of the ramp parameters. This remote control is particularly advantageous during the optimization procedure. Subsequently, the microwave signal is amplified using a 15 W amplifier[10] before being directed to the microwave antenna. The microwave antenna used in this setup comprises a single winding with a diameter of approximately 4 cm. The antenna is positioned on top of the science chamber in close proximity to the viewport, ensuring an effective and optimal delivery of the microwave signal.

To evaluate the performance of the implemented microwave evaporation, we recorded the atom number and temperature of the atomic cloud for different trap depths, as depicted in figure 4.6. The microwave sweep was performed with a constant starting frequency of 1570 MHz and was ramped to f_{final} within 4 s. For the presented data[11], f_{final} was scanned in the range $1620 - 1760$ MHz in steps of 20 MHz.
Starting with 5×10^6 atom counts at a temperature of 200 µK in the magnetic trap, the evaporative cooling process initially works as expected, decreasing temperature T and atom number N in a power-law fashion. The efficiency of evaporative cooling in this regime can be quantified by the relation:

$$\alpha = \frac{d\log(T)}{d\log(N)} \tag{4.4}$$

with additional details provided in [164].
While we observe a constant $\alpha = 0.70(2)$ above a temperature of approximately 100 µK,

[9] Agilent E4421B
[10] Mini-Circuits ZHL-15W-422-S+
[11] This dataset was recorded using fluorescence imaging, where the absolute atom number calibration is not as reliable.

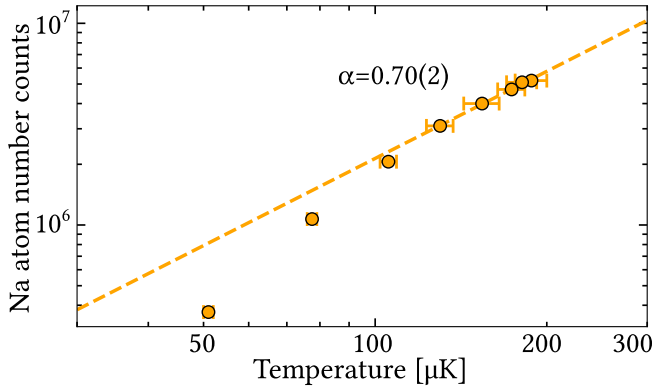

Figure 4.6.: Efficiency of microwave evaporation of sodium in the magnetic trap. The atom number is plotted as a function of the temperature of the cold atomic cloud on a double logarithmic scale. The dashed line represents a power law fit, following equation 4.4, to the first five data points to the right.

deviations arise when attempting further evaporation. In this temperature regime, so-called *Majorana losses* [165] begin to dominate the evaporation process. Herein, cold atoms close to the magnetic field zero of the magnetic quadrupole trap are susceptible to spin flips, leading to their subsequent loss from the trap. These Majorana losses impose limitations on the achievable phase-space densities during the evaporative cooling process [162].

A commonly employed strategy to address this issue involves the implementation of a blue-detuned plug beam. This beam is used to create a repulsive potential at the trap centre, effectively eliminating the magnetic field zero and preventing the detrimental spin flips [2].

Alternatively, a different approach requires the operation of a hybrid trap, as realized in studies such as [166, 167]. In this configuration, a dipole beam is aligned vertically below the centre of the magnetic trap. This alignment ensures that the trap minimum of the combined trap occurs at a finite magnetic field value, overcoming the challenge of Majorana transitions. In our experiment, we start with a pure magnetic quadrupole trap, and once the microwave evaporation is initiated, the dipole beams are introduced to achieve a hybrid configuration.

Experimental sequence

The experimental sequence during the magnetic trap phase is depicted in figure 4.7. After 200 μs of optical pumping, we switch off the MOT light and turn on the magnetic field gradient to an initial current of $B_{\text{init}} = 100\,\text{G/cm}$. This initial magnetic field gradient plays a crucial role in facilitating the atom transfer from the MOT to the

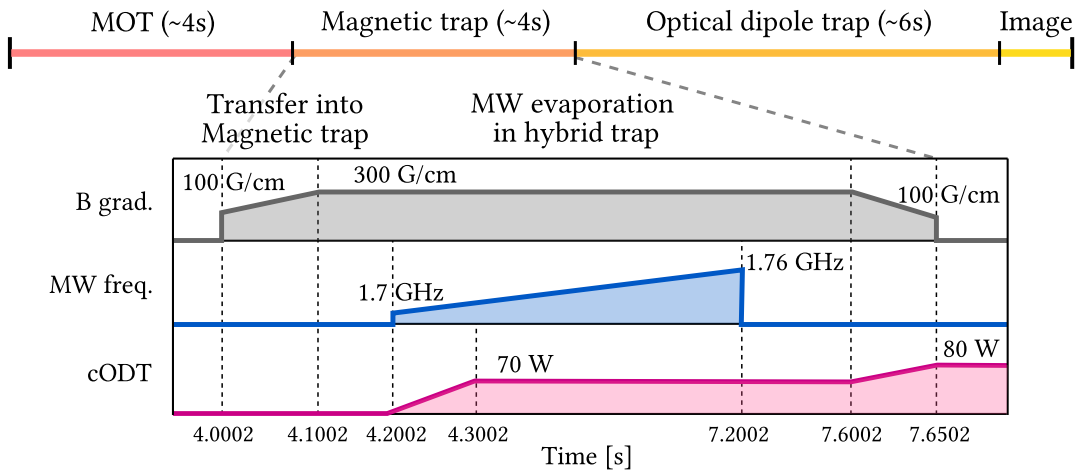

Figure 4.7.: Sketch of the experimental sequence for the magnetic trap stage. After ramping up the magnetic field gradient, the microwave (MW) frequency for evaporation is swept in 3 s from 1.7 GHz to 1.76 GHz. During this evaporation process, the trap is operated in a hybrid configuration with the dipole laser running at 70 W.

magnetic trap. The magnetic field gradient must be strong enough to support the atoms against gravity, while a sudden diabatic change of the magnetic field gradient to a high value can transfer excess energy to the atomic cloud, inducing heating. A spatial mismatch between the two traps will additionally increase the temperature of the atoms. The value for B_{init} was found experimentally by optimizing the phase-space density in the crossed optical dipole trap. The gradient is then adiabatically increased to a value of 300 G/cm within 100 ms.

At this strong magnetic field gradient, we evaporatively cool the atoms by sweeping the microwave (MW) frequency from 1.7 GHz to 1.76 GHz within 3 s. Simultaneously, we ramp up the power of the dipole beams to a total power of 70 W to create the hybrid configuration discussed before. The MW-evaporation is followed by a 400 ms thermalization time. At the end of this stage, the atomic sample comprises approximately 5×10^5 atoms, with a temperature of around 10 µK [12]. Finally, the magnetic field is ramped down, and the atoms are subsequently loaded into an all-optical crossed dipole trap.

[12] The accuracy of the atom number and temperature estimation in the magnetic trap suffers from the finite switch-off times of the magnetic field coils.

4.3. Crossed optical dipole trap

Optical trapping of neutral atoms using strongly focused far-red detuned laser beams has become a standard technique in the field of cold atoms since its first experimental implementation in 1986 [168]. Such far-off resonant beam traps are not limited by light-induced processes compared to traps relying on radiation pressure. Moreover, these optical traps are insensitive to the respective spin states [169] and offer flexibility in trapping geometries [170].
Most importantly, we cannot achieve dual-species condensation for our ^{23}Na-^{39}K mixture in the implemented magnetic trap due to substantial inter-species collisional losses in the absence of a magnetic bias field. In contrast, in a pure optical dipole trap, the magnetic field coils can be switched from anti-Helmholtz to Helmholtz configuration, such that the bias magnetic field becomes a freely adjustable parameter, enabling the access to a more favourable interaction regime. Moreover, this optical trapping method facilitates working with spin configurations that are otherwise untrappable in magnetic traps (high-field seekers).

4.3.1. Theory

The mechanism underlying the optical dipole trap involves the interaction of the electric field of the laser with the induced atomic dipole moment and is known as the *AC-Stark effect*. This interaction leads to an energy shift of the ground state, which can be utilized as a trapping potential for neutral atoms.
Following [170], the trapping potential experienced by neutral atoms within an optical dipole trap formed by a single far-red detuned laser beam is given by:

$$V_{\mathrm{ODT}}(x,y,z) = -\frac{1}{2\epsilon_0 c}\,\mathrm{Re}(\alpha)\,I(x,y,z) \tag{4.5}$$

where $I(x,y,z)$ is the intensity of the focused laser beam, and α is the complex polarizability of the atom, which measures the coupling strength to the laser field. The real part of the polarizability can be calculated by

$$\mathrm{Re}\big[\alpha(\omega)\big] = \frac{3\pi c^3 \epsilon_0}{\omega_0^3}\left(\frac{\Gamma}{\omega_0-\omega}+\frac{\Gamma}{\omega_0+\omega}\right) \tag{4.6}$$

where ω is the laser frequency, and Γ and ω_0 are the linewidth and frequency of the atomic transition, respectively. If the laser is tuned close to the atomic resonance such that the detuning $\Delta = \omega_0 - \omega \ll \omega_0$, the counter-rotating term can be neglected within

the *rotating wave approximation*. In this case, the dipole potential takes the form:

$$V_{\mathrm{ODT}}(x,y,z) = \frac{3\pi c^2}{2\omega_0^3}\,\frac{\Gamma}{\Delta}\,I(x,y,z) \tag{4.7}$$

Consequently, the potential experienced by the atoms is inversely proportional to the laser detuning, resulting in an attractive potential when employing a red-detuned laser beam. Additionally, the trapping potential resembles the intensity profile $I(x,y,z)$ of the detuned beam.

In order to suppress the scattering rate $\Gamma_{\mathrm{sc}} \propto I/\Delta^2$, and prevent additional heating effects, the dipole trap is typically operated in the regime characterized by high intensities and large detunings. Achieving high intensities involves tightly focusing the red-detuned laser beam, causing atoms to be attracted towards the focal point of this Gaussian laser beam. In the vicinity of the laser focus, the trap can be approximated by a harmonic confinement with radial and axial trapping frequencies

$$\omega_r = \sqrt{\frac{4V_0}{mw_0^2}}\ , \quad \omega_x = \sqrt{\frac{2V_0}{mx_R^2}} \tag{4.8}$$

with the trap depth $V_0 = V_{\mathrm{ODT}}(0,0,0)$, the beam waist w_0, and the Rayleigh range $x_R = \pi w_0^2/\lambda$. Compared to the spatial extent of the atomic cloud, the Rayleigh range is typically quite large, resulting in a weak confinement along the beam direction in the order of a few Hertz.

To address this issue of inhomogeneous trapping, an additional perpendicular beam is introduced in what is termed a crossed optical dipole trap (cODT) [171]. This perpendicular beam helps counteract the weak longitudinal confinement. With beam 1 (waist $w_{0,1}$, trap depth $V_{0,1}$) propagating along the x'-axis and beam 2 (waist $w_{0,2}$, trap depth $V_{0,2}$) along the perpendicular y'-direction, one arrives at the modified trapping frequencies:

$$\omega_{x'} = \sqrt{\frac{4V_{0,2}}{mw_{0,2}^2}}\ , \quad \omega_{y'} = \sqrt{\frac{4V_{0,1}}{mw_{0,1}^2}}\ , \quad \omega_z = \sqrt{\omega_{x'}^2 + \omega_{y'}^2} \tag{4.9}$$

Consequently, this setup achieves tight confinement along all three spatial axes.

An essential aspect for the crossed dipole trap is preventing interference between the two intersecting beams, as such interference could alter the trapping potential. This can be accomplished by employing orthogonal polarizations or introducing a frequency detuning between the two intersecting beams.

During forced evaporative cooling in the dipole trap, lower laser intensities are required. In this setting, the gravitational potential also becomes significant. The total potential along the vertical z-direction is then modified to:

$$V_z = V_{\mathrm{ODT}}(0,0,z) + V_{\mathrm{grav}} \approx \frac{1}{2} m\omega_z^2 z^2 + mgz \tag{4.10}$$

where we have used the harmonic approximation for the optical trapping potential along the z-axis. This mass-dependent trapping potential leads to a spatial displacement along the vertical z-direction for atoms trapped in the optical dipole trap:

$$\partial_z V_z = m\left(\omega_z^2 z_0 + g\right) \stackrel{!}{=} 0 \;\rightarrow\; z_0 = -\frac{g}{\omega_z^2} \tag{4.11}$$

where ω_z, according to equation 4.9, depends on the mass m of the atoms and the trapping potential V_0, resulting in a species-dependent displacement of the atoms along z, which is called the *gravitational sag*[13].

4.3.2. Optical layout

The optical arrangement for the crossed optical dipole trap is shown in figure 4.8. The light is supplied from a 100 W fibre laser[14] operating at a wavelength of 1070 nm, possessing a linewidth of 4 nm, and featuring a collimated output beam with a diameter of 5 mm.

At these high laser intensities, thermal lensing can play a significant role. This phenomenon arises from the partial absorption of incident light by each optical element, resulting in non-uniform heating of the element. Given that the index of refraction is temperature-dependent, this effect leads to changes to the focal spot's size and position. Such variations are detrimental to the effective operation of a focused beam dipole trap. Therefore, we use UV-grade fused silica lenses featuring a lower coefficient of thermal expansion compared to the standard N-BK7 material.
To minimize the impact of thermal lensing attributed to the TeO_2 crystal within the AOM, as studied in [172], we keep the input power into the AOM constant. The final trap depth is regulated by adjusting the RF-power supplied to the AOM.

[13] Additional information regarding the magnitude and impact of the gravitational sag of sodium and potassium will be given in section 5.3.
[14] IPG Photonics YLR-100-1070-LP

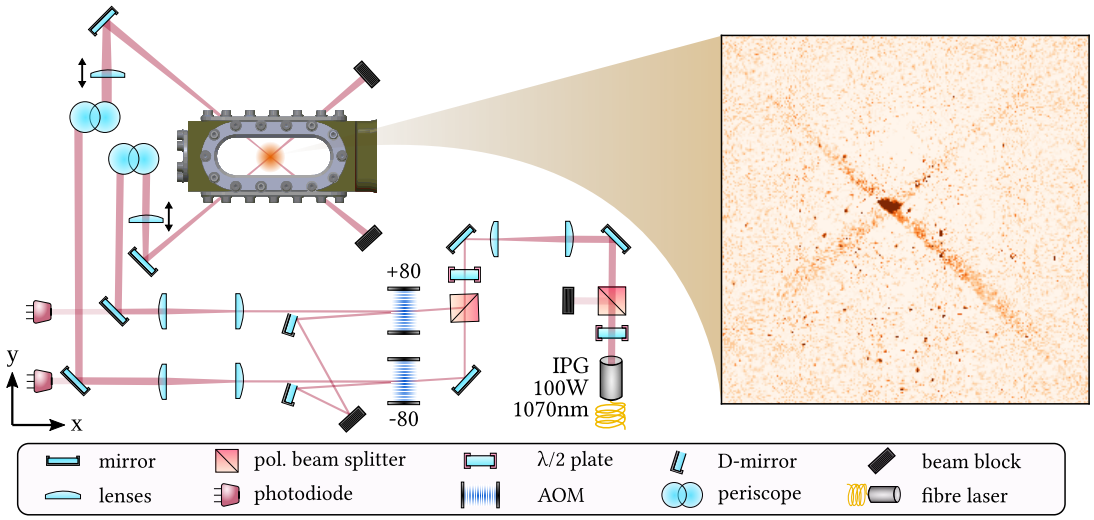

Figure 4.8.: Optical layout of the crossed optical dipole trap (cODT). The light from the dipole laser is intensity-stabilized with AOMs and then focused onto the atoms. The RF-frequencies supplied to the AOMs are given in units of MHz. The 400 mm final focusing lenses are mounted on linear translation stages. The image on the right shows the fluorescence of atoms in the cODT viewed from the top.

Following a polarization cleaning cube, the first 3:1 Keplerian telescope reduces the beam diameter to 1.67 mm. This reduction is necessary to enable the beam to pass through the aperture of the acousto-optical modulator[15]. Subsequently, the beam is divided into two using another polarising beam splitter and guided through the two AOMs that are mounted to four-axis alignment stages[16]. These compact, high-stability stages allow for precise positioning and ease the optimization of the diffraction efficiency. The AOMs operate at frequencies of 80 MHz and −80 MHz, respectively, guaranteeing no adverse interference effects. The un-diffracted order is directed into a water-cooled copper beam dump using a D-shaped mirror. The diffracted beam, which was optimized to 90 % diffraction efficiency, is then expanded back to 5 mm. This specific beam diameter was chosen to ensure that upon passing through the final focusing lens with a focal length of 400 mm, the desired focal waist of 55 µm is achieved.
The mirrors that were used for this setup exhibit a reflectance of approximately 99.8 %, causing a small fraction of incident light to be transmitted. The transmitted light of the two mirrors on the left in figure 4.8 is recorded by two dedicated biased photodiodes. The photodiode signal is fed into a home-built PID controller that adjusts the RF-power of the AOM and, thus, the optical power of the diffracted beam, depending on

[15]Gooch & Housego 3080-199
[16]Newport 9071-M

an external setpoint. Therefore, this feedback loop acts as an intensity stabilization setup for the two dipole beams and enables the precise control over the final trap depth.

Given that these optical components are positioned at the lowest level, directly mounted on the optical table, two periscopes are used to vertically translate the beams to the plane of the trapped atoms. After passing through the final focusing lens, the light is directed into the chamber and subsequently blocked at the output using a beam block.

To initially align the two dipole beams onto the atoms, a 1 mm resonant sodium beam was directed at the last in-coupling mirror[17]. This mirror is coated to reflect light in the range of 1030-1090 nm, allowing the resonant sodium light at 589 nm to be transmitted and consequently reach the sodium magneto-optical trap. The resonant beam was aligned by optimizing the disturbance to the high gradient MOT. Subsequently, the dipole beam was superimposed with the aligned resonant beam using the last two mirrors, and the overlap was checked both before and after passing through the chamber. To make the infra-red (IR) beams visible, we either used an IR viewer or an IR detection glass[18], allowing for continuous tracking of the high-power dipole beam. The alignment procedure was subsequently repeated for the other beam path.

This initial alignment served as a good starting point to make the final adjustments utilizing the atom signal. Approximately 1 s before concluding the microwave evaporation, we turned on the dipole beams and imaged the atoms after evaporation using the coarse imaging system from the side. This resulted in two vertically displaced atomic clouds that were elongated along the less confining beam direction. To compensate for this misalignment, we vertically displaced the beams optimizing their overlap. The crossing point was then shifted to the centre of the magnetic trap using fluorescence imaging from above, as depicted in figure 4.8. Finally, we adjusted the focusing lenses, which are mounted on linear translation stages, such that the two beams cross at their respective focus positions.

With this optical layout, a theoretical beam waist radius of approximately 55 µm is achieved in the focus, resulting in a trap depth of 0.9 mK (2.2 mK) for sodium (potassium). These trap depths are sufficient for trapping the atoms following the magnetic trap, during which microwave evaporation cools them down to a few tens of µK.

[17] LensOptics M1064/1″/0
[18] Precision Laser Scanning HI POWER – IR VIEWER

4.3.3. Evaporation in cODT to degeneracy

In the crossed optical dipole trap, we perform the final cooling stage called forced evaporative cooling. This process involves lowering the trapping potential by reducing the power of the dipole beams. The strategy is to selectively remove the hottest atoms from the trap, leaving the remaining atoms to re-thermalize at a lower temperature. We perform the evaporation using two linear intensity ramps, as displayed in figure 4.9.

The first intensity ramp has a duration of 2 s and lowers the power from an initial value of 80 W to 10 W. Subsequently, a second ramp is executed over 4 s, further reducing the power to reach a final value of 0.15 W. After another 200 ms of holding at this power setting, we turn off the dipole trap and image the cold atomic cloud after a certain time-of-flight using the horizontal high-resolution absorption imaging setup.

The quantum degenerate regime is reached after executing these two evaporation ramps. Figure 4.10 illustrates the atomic density profiles for different evaporation depth. The images were obtained using a time-of-flight of 4 ms, which is why the thermal cloud in the left-most image appears very dilute, as the row of images is plotted on a fixed colour scale. By lowering the final dipole power, the density in the central part of the cloud increases. This feature becomes even more pronounced when observing the integrated column density, where a bimodal structure emerges.

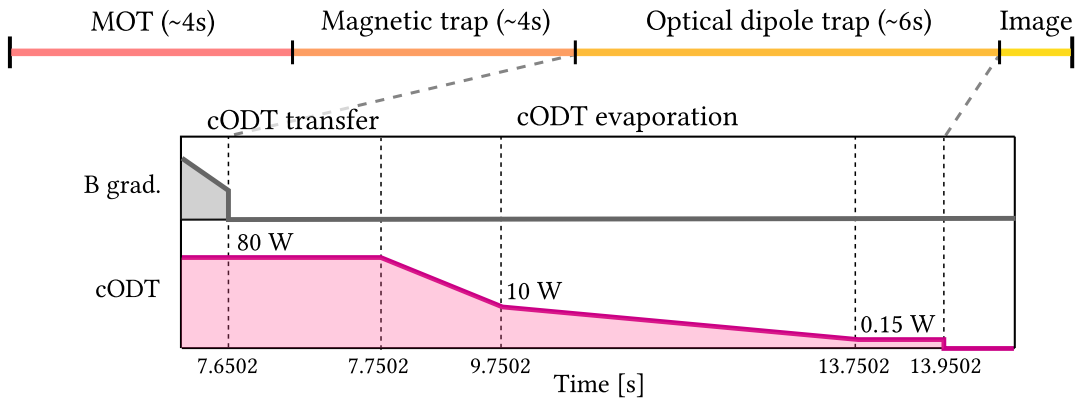

Figure 4.9.: Sketch of the experimental sequence for cooling sodium in the crossed optical dipole trap (cODT). After transferring atoms from the magnetic trap into the cODT, we perform forced evaporative cooling. In this evaporation process, the dipole power is reduced over 6 s with two consecutive ramps from an initial value of 80 W to 0.15 W. The subsequent destructive imaging process marks the end of the experimental sequence.

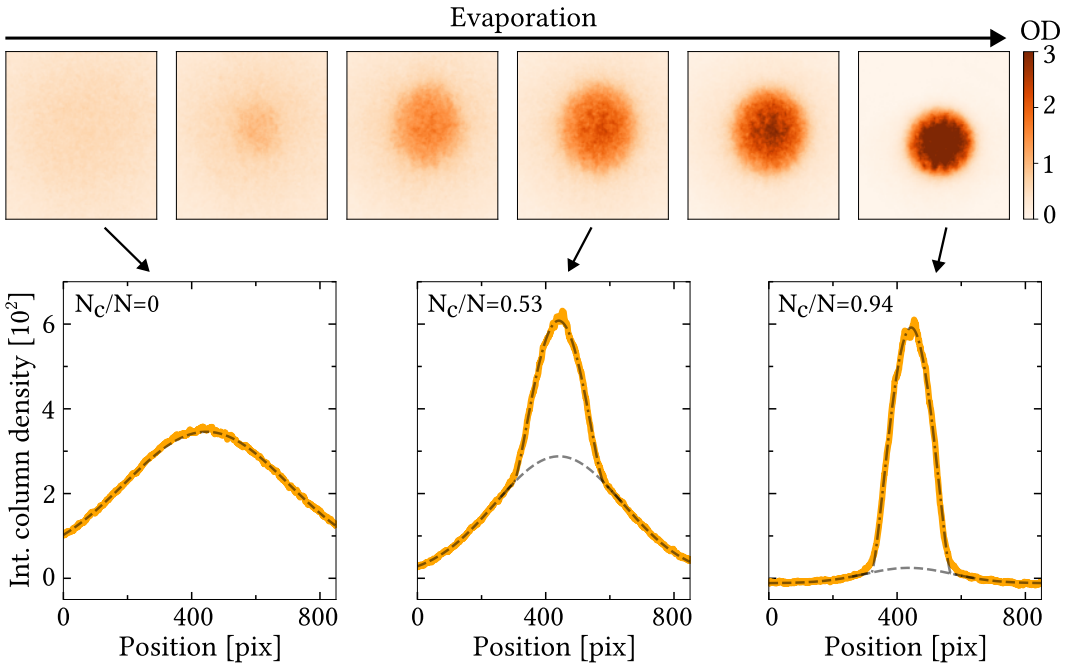

Figure 4.10.: Evolution of the sodium atomic cloud during forced evaporative cooling in the crossed optical dipole trap. The top row of images shows absorption images of the sodium cloud at different time instances along the evaporation ramp for a time-of-flight of 4 ms. To obtain the right-most image, we ramped the dipole power all the way down to 0.15 W, as illustrated in figure 4.9. The bottom row shows three graphs of the column density integrated along the vertical z-axis. The bimodal structure is evident from the fits, represented by the dashed (thermal) and dash-dotted (BEC-contribution) lines.

The observed bimodal density profile, as outlined in appendix B, comprises a Gaussian thermal component n_{th} and a parabolic condensate component n_{BEC}. For a high condensed fraction, the thermal component only survives in the wings, exemplified in the right graph of figure 4.10. In the proximity of the region where the thermal and condensate parts overlap, the density distribution is distorted due to interaction between the two components. Hence, a direct bimodal fit is unlikely to perform well, and the fitting procedure is carried out stepwise, as further detailed in appendix B. The dashed line represents the thermal part, while the condensate component is depicted by the dash-dotted fit.

Due to the fact that a BEC does not conform to a Maxwell-Boltzmann distribution, the expansion of the condensate upon turning off the trap does not yield information about its temperature. However, as the thermal cloud is in thermal equilibrium with the condensate, the thermal wings can be used to obtain the temperature of the ultra-

cold cloud.

In addition to the emergence of a bimodal velocity distribution, another signature indicating Bose-Einstein condensation involves the inversion of the aspect ratio during free expansion, as firstly observed by Anderson et al. [1] and Davis et al. [2]. Starting from an anisotropic trap characterized by differing axial and radial trapping frequencies, the cloud will expand faster in the direction of stronger confinement. This results in an inversion of the atomic cloud's aspect ratio as the parabolic density profile undergoes rescaling [75, 173, 174]. This behaviour is in contrast to the expansion of a thermal cloud, which is isotropic, such that the released cloud takes a spherical shape. However, our observations, as depicted in figure 4.10 for a fixed time-of-flight of 4 ms and figure 3.24 A, where we varied the time-of-flight subsequent to achieving a sodium BEC, did not reveal an anisotropic aspect ratio. The nearly spherical shape of the condensed atom cloud suggests comparable axial and radial trapping frequencies when operating the crossed optical dipole trap at a power of approximately 0.15 W.

Following the initial successful achievement of a sodium Bose-Einstein condensate, we optimized various parameters of the cooling sequence to improve the condensed atom number. Starting with the speed of the evaporation ramps, adjustments were made to the experimental parameters in prior cooling stages, encompassing frequency detunings and laser beam intensities. One crucial optimization parameter is the overlap of the two crossed dipole beams. We are especially sensitive to misalignments in the vertical overlap, which can be caused by temperature fluctuations in the laboratory. Consequently, every few days a slight realignment of the vertical adjustment screw of the last in-coupling mirror is required. Typically, re-optimization is performed for the number of condensed atoms at the end of the evaporation. However, if the overlap significantly degrades, resulting in no atoms remaining after the evaporation in the dipole trap, the atom signal in the hybrid trap is used instead. To guarantee a more stable operation and be less sensitive to external perturbations, we are planning to implement a temperature stabilization system for the entire laboratory.

While we optimized the different parameters in the cooling sequence to achieve a stable and reproducible sodium BEC with approximately 7×10^4 atoms, exhaustive optimization of this sequence was not extensively pursued. The reason for this approach is our intention to set up a mixture experiment, and not a single-species sodium BEC-machine. Such an experiment requires dual-species degeneracy, which will significantly alter the current experimental sequence, requiring certain compromises. There-

fore, a thorough optimization will be pursued once both sodium and potassium can be cooled to form a BEC in a dual-species setup.
However, before moving further with efforts towards dual-species degeneracy, we wanted to use the sodium BEC to characterize the cODT in terms of its trapping frequencies.

4.3.4. Measurement of trapping frequencies

Our crossed optical dipole trap (cODT) comprises two infra-red laser beams operating at a wavelength of 1070 nm. These beams are focused down to a beam waist of 55 µm. The power in each beam is intensity-stabilized using an AOM and can be increased to approximately 40 W per beam.
An essential parameter when characterizing an optical dipole trap is the corresponding trapping frequency in the harmonic approximation. The trapping frequencies along the different spatial dimensions determine the trapping geometry and other vital aspects of the condensate. These frequencies can be extracted using two approaches:

DIPOLE OSCILLATIONS: Trapping frequencies can be extracted by observing the oscillations of the atom cloud in the trap after applying an external force, as described in [175].

PARAMETRIC HEATING: The system is parametrically driven, and heating is anticipated if the drive frequency approaches twice the trapping frequency [176,177].

In the following, we present the results obtained from both approaches for measuring the trapping frequencies in the cODT.

Dipole oscillations

In both approaches, we begin with a sodium BEC within the crossed optical dipole trap and ramp the dipole power to 10 W (5 W per beam). To excite the collective modes of the condensate in this trap, both dipole beams are pulsed off for 500 µs, subsequently turned on again to the initial power of 10 W, and held at this setting for a variable hold time. During this hold time, the condensate exhibits a sloshing-like motion in the trap. The atomic cloud is imaged after a 4 ms time-of-flight using the horizontal fine imaging system, such that the vertical z-axis is along gravity and the x-direction at a particular angle (roughly 45°) with respect to the two perpendicular dipole beams. We denote the dipole beam axes as x' and y'.

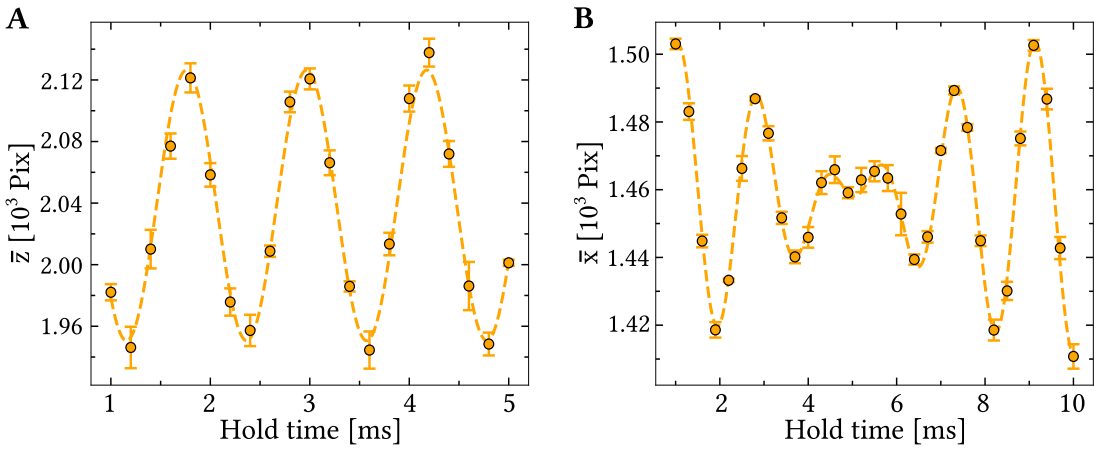

Figure 4.11.: Measurements of dipole oscillations along the two imaging directions to determine the trapping frequencies of the crossed optical dipole trap. A: Dipole oscillations of the mean position of the atomic cloud along gravity direction (z-axis). Using a sinusoidal fit (dashed line), we can extract the trapping frequency $\omega_z = 2\pi\times828(3)$ Hz. B: Dipole oscillations of the mean position of the atomic cloud along the horizontal x-axis. Fitting a beat-like oscillation (see equation 4.12), as indicated by the dashed line, to the experimental data yields the trapping frequencies $\omega_{x'} = 2\pi \times 506(3)$ Hz and $\omega_{y'} = 2\pi \times 604(4)$ Hz.

Figure 4.11 shows the dipole oscillation measurement results, where the hold time was scanned, and the motion of the centre-of-mass was tracked utilizing three averages. Along the vertical axis (see figure 4.11 A), a distinct sinusoidal oscillation of the centre-of-mass of the atomic cloud is observed, characterized by a frequency $\omega_z = 2\pi \times 828(3)$ Hz.

In contrast, the oscillation observed along the x-axis, as depicted in figure 4.11 B, is defined by a beat-like behaviour involving two frequencies. This phenomenon can be attributed to the fact that we are imaging at a specific angle with respect to the dipole beam plane. Therefore, a beating between the trapping frequencies of the two beams emerges. Imbalances in the two trapping beams, such as power imbalances or different focal positions, introduce asymmetry into the trapping potential, resulting in the manifestation of two distinct trapping frequencies.

To analyse this beat-like oscillation, the data was subjected to fitting using the following model function:

$$\overline{x}(t) = \overline{x}_0 + e^{-t/t_0}\left[A_{x'}\sin\left(\omega_{x'}t + \phi_{x'}\right) + A_{y'}\sin\left(\omega_{y'}t + \phi_{y'}\right)\right] \tag{4.12}$$

where a damping term and two frequencies $\omega_{x'}$ and $\omega_{y'}$ are considered. Fitting this model to the experimental data enables the extraction of the two horizontal trapping frequencies, $\omega_{x'} = 2\pi \times 506(3)\,\mathrm{Hz}$ and $\omega_{y'} = 2\pi \times 604(4)\,\mathrm{Hz}$. The discrepancy between the trapping frequencies along x' and y' is likely caused by an imperfect focal alignment, such that the two foci do not overlap at the position of the atoms.

Parametric heating

In the second method, we excite the parametric oscillation of the trapped atomic cloud by modulating the dipole beam power around an average value of $P_0 = 10\,\mathrm{W}$ with a specific drive frequency f_{mod}

$$P(t) = P_0[1 + \epsilon \sin(2\pi f_{\mathrm{mod}} t)] \tag{4.13}$$

where ϵ parametrizes the relative modulation strength.
This sinusoidal modulation of the trap depth imposes forced oscillations on the atoms within the trap. Specifically, when the modulation frequency coincides with a resonance feature at $f_{\mathrm{mod}} = 2f_0/n$, with trapping frequency f_0 and $n = 1, 2, 3, ...$, the kinetic energy of the atoms within the trap increases exponentially, and the atoms are heated out of the trap. The width of these resonances decreases exponentially with n [178]. However, the influence of the gravitational sag when modulating the dipole intensity leads to an effective coupling to the dipole mode. As a consequence, the strongest excitation for our system occurs when the modulation frequency is equal to the trapping frequency [179].
Similar to the previous approach, we increased the dipole power to 10 W following the successful creation of a sodium BEC. Subsequently, the dipole power was sinusoidally modulated with a relative modulation amplitude of $\epsilon = 2\,\%$. Special care was taken to keep the modulation on for integer periods to guarantee the same conditions for different modulation frequencies.

Figure 4.12 presents the results of the parametric heating measurements, where three averages were taken for each drive frequency. Scans of the modulation frequency reveal three loss features (A, B, and C). The excitation is maximized when the drive frequency is at the fundamental or higher harmonics of the trapping frequency, resulting in atom-loss features. The locations of these resonance minima, corresponding to the fundamental trapping frequencies, are extracted through Lorentzian fits.
Table 4.1 provides a summary of the extracted values for the trapping frequencies

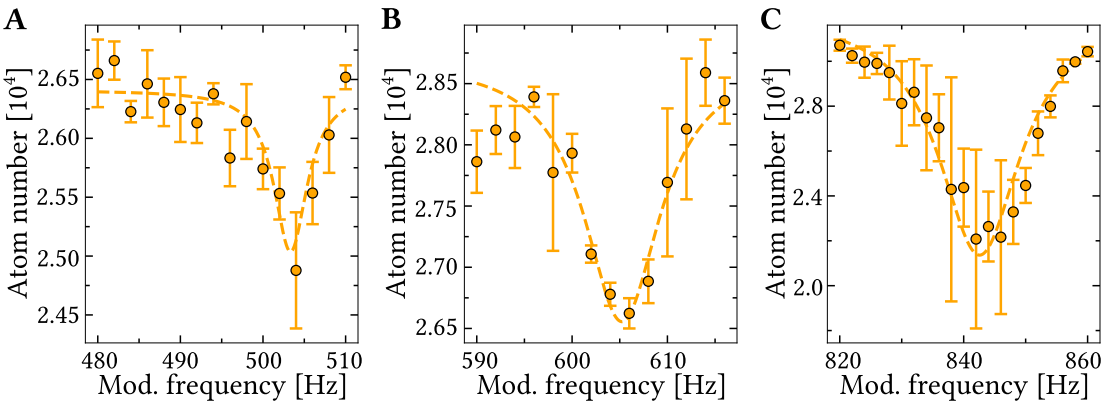

Figure 4.12.: Parametric heating of sodium atoms in the crossed optical dipole trap. The intensity of the dipole beams is modulated at a certain drive frequency, which we scan in three different ranges, resulting in the loss features shown in A, B, and C. The dashed lines represent Lorentzian fits to the experimental data.

Table 4.1.: Summary of the results concerning the trapping frequency measurements in the crossed optical dipole trap carried out at a dipole power of 10 W.

	$\omega_{x'}$	$\omega_{y'}$	ω_z
Dipole oscillations	$2\pi \times 506(3)$	$2\pi \times 604(3)$	$2\pi \times 828(3)$
Parametric heating	$2\pi \times 503(1)$	$2\pi \times 605(1)$	$2\pi \times 843(1)$

obtained using the two methods at a dipole power of 10 W. Notably, the frequencies along x' and y' are in good agreement, but there is a slight discrepancy for ω_z. Probable additional error sources include the strength and duration of the parametric modulation, leading to broadening and shifts of the resonance feature. Furthermore, a minor misalignment of the overlap of the two dipole beams from one measurement to the next could account for the deviations in the trapping frequencies along the z-axis.

Notably, achieving the measured trapping frequencies in a crossed optical dipole trap, with an approximate power of 5 W per beam, requires an expected beam waist of about 65 µm. In contrast, the ideal beam waist radius, obtained by focusing a perfectly collimated laser beam with a diameter of 5 mm through a lens with a focal length of 400 mm, is 55 µm. This discrepancy is likely a result of imperfect alignment of the foci positions and the overlap of the two crossed dipole beams.

Conclusion

The sodium atoms are initially loaded from a two-dimensional magneto-optical trap into a dark-SPOT MOT. This trap exhibits an increased atom density, particularly at the central region, where atoms are maintained in a dark state, mitigating repulsive forces arising from re-scattered photons. At the end of this first cooling stage, we have roughly 2×10^8 atoms at a temperature of approximately 200 µK.
The atoms are subsequently optically pumped to the $|F = 1\rangle$ ground state and transferred into the magnetic trap, where the low-field seekers $|1, -1\rangle$ remain trapped. Microwave-assisted evaporation is then employed to selectively remove hot sodium atoms, consequently reducing the temperature and increasing the phase-space density of the sodium cloud.
Lastly, the atoms are loaded into a crossed optical dipole trap, where a final evaporation stage is initiated by decreasing the dipole potential. Upon completing the 12 s long sequence, the degeneracy threshold is crossed, resulting in the attainment of a Bose-Einstein condensate of sodium, characterized by $N = 7 \times 10^4$ atoms.

CHAPTER 5

Second step: Adding potassium to the mix

Now that sodium atoms have been successfully condensed, the next logical progression is to extend our efforts towards achieving condensation for potassium atoms. Although the task of dual-species condensation might appear straightforward initially - leveraging sodium as a sympathetic coolant and adapting the cooling sequence - complications arise due to inter-species losses resulting from three-body collisions. These losses become particularly prominent in the high-density regime of the crossed optical dipole trap. Additionally, the influence of light-assisted collisions during the dual-species MOT stage must be taken into account.

In this chapter, I will start with a discussion of the first cooling stage for sodium and potassium - the dual-species MOT. This section describes the challenges encountered when loading both species simultaneously (see section 5.1). Subsequently, in section 5.2, I will introduce the grey molasses cooling technique for potassium. This method employs D1 laser light to decrease the temperature of the atomic cloud to approximately 7 μK.
After a magnetic trap stage involving microwave evaporation of sodium, we load both species into the crossed optical dipole trap (see section 5.3). The bias magnetic field is then ramped up to access the tunability of inter- and intra-species interactions via Feshbach resonances, as explained in section 5.4. Finally, in section 5.5, I will provide a detailed account of our current experimental progress concerning dual-species condensation of ^{23}Na and ^{39}K.

5.1. Dual-species MOT

When dealing with two atomic species, a straightforward approach for the magneto-optical trap stage involves loading both species simultaneously in a so-called dual-species MOT. Figure 5.1 presents images of the atomic fluorescence from both the potassium MOT (on the left) and sodium MOT (on the right) in the science chamber.

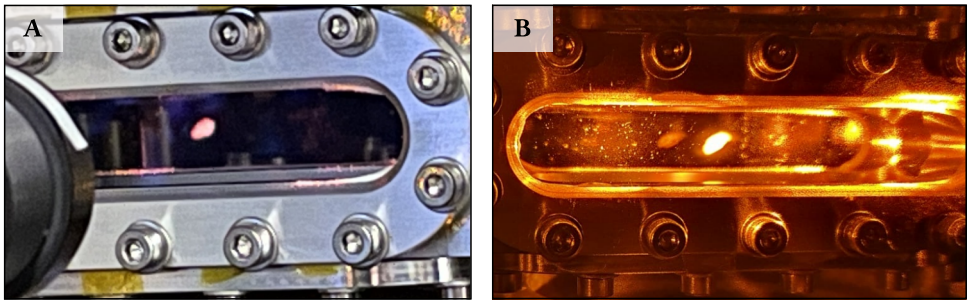

Figure 5.1.: Images of the atomic fluorescence from the potassium MOT (A) and sodium MOT (B) in the science chamber.

However, when loading both species simultaneously, we observed atom losses. This phenomenon can be attributed to light-assisted collisions between ground state and excited state atoms [151, 152, 180, 181]. The underlying principle of these collisions is schematically depicted in figure 5.2 A.
For collisions involving one atom in an excited P-state and another in a ground S-state, two collisional loss processes come into play: radiative escape and fine-structure changing collisions. In radiative escape, two atoms, denoted as A (in P-state) and B (in S-state), combine to form a loosely bound pair (S+P) and approach each other along an attractive potential. The atoms accelerate towards each other, converting their decreasing potential energy to kinetic energy. Subsequent spontaneous emission drives the atoms back to the ground state. If the kinetic energy ΔE gained during this collision process exceeds the trap depth of the magneto-optical trap, the atoms will be lost from the trap. Additionally, collisions can induce fine-structure changing transitions, where the energy difference between the excited state's fine-structure states is converted to kinetic energy, ultimately resulting in atom loss from the trap.

In dual-species operation, the comparably small number of potassium atoms does not significantly influence the sodium cloud. However, we observe a substantial potassium atom loss from the trap when sodium atoms are simultaneously loaded. The loading dynamics in such an imbalanced mixture, where the sodium atom number remains largely unaffected, can be described by the following rate equation [148, 183, 184]:

$$\frac{dN_K}{dt} = L_K - \alpha N_K - \beta_{NaK} n_{Na} N_K \tag{5.1}$$

where L_K describes the loading rate, and α summarizes the potassium loss contributions. The last term characterizes the loss of potassium atoms due to collisions with sodium atoms (density n_{Na}), which is parametrized by the two-body loss rate coeffi-

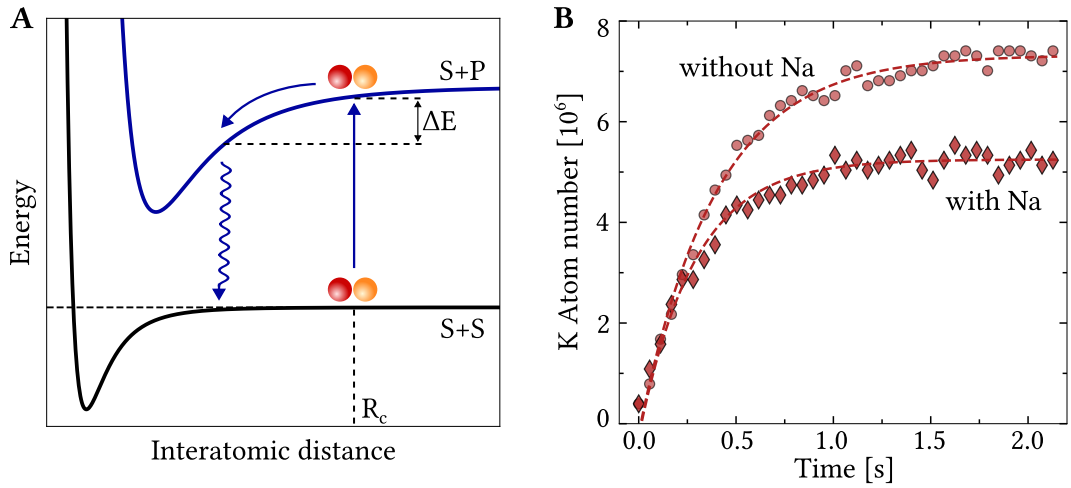

Figure 5.2.: Light-assisted collisions in a dual-species MOT. A: Principle of light-assisted collisions, showing interaction potentials versus the inter-particle separation. Arrows indicate the excitation of an atom pair to an attractive interaction potential. Figure adapted from [182]. B: Potassium MOT loading curve with and without the presence of a sodium MOT. The dashed lines indicate a fit, according to equation 5.2, to the experimental data.

cient β_{NaK}. Note that equation 5.1 can be reduced to the case of single species loading by neglecting the last term.

The solution to the above rate equation is given by

$$N_{\mathrm{K}}(t) = \frac{L_{\mathrm{K}}}{\alpha + \beta_{\mathrm{NaK}} n_{\mathrm{Na}}} \left[1 - e^{-(\alpha + \beta_{\mathrm{NaK}} n_{\mathrm{Na}}) t} \right] \tag{5.2}$$

An exemplary measurement[1] of a potassium MOT loading curve is presented in figure 5.2 B, where we compare the potassium loading scenarios with and without the presence of sodium. In the case of dual-species loading, the sodium MOT is initially loaded until the atom number reaches a steady-state. Subsequently, the potassium MOT loading is initiated. Notably, the number of potassium atoms in the MOT is reduced in the presence of a sodium MOT, ultimately reaching a lower steady state value. The issue of light-assisted collisions for a ^{23}Na-^{39}K mixture was also reported by Castilho et al. [151] and Sutradhar et al. [181].

To mitigate the impact of light-induced losses during the loading dynamics of a dual-species system, the application of a dark SPOT MOT has been investigated in various

[1] The magneto-optical traps for both sodium and potassium were not fully optimized for this measurement.

mixture experiments, including ^{39}K-^{87}Rb [185], ^{7}Li-^{87}Rb [184], and ^{7}Li-^{133}Cs [186]. Within these studies, a dark SPOT MOT for ^{87}Rb or ^{133}Cs, respectively, significantly reduced the impact of light-induced losses, as the excited state population is greatly diminished in a dark SPOT MOT. Collisions between ground state ^{87}Rb or ^{133}Cs atoms and ^{39}K or ^{7}Li, respectively, in their excited state do not lead to trap losses, as their molecular potential curves are repulsive [187].

In our specific case, when the sodium MOT is operated in a dark SPOT configuration, sodium atoms predominantly occupy the $|F = 1\rangle$ ground state (3S). Consequently, light-assisted collisions would primarily occur with potassium atoms in the excited state (4P). The corresponding interaction potential is attractive [187], facilitating these collisional losses in principle. A correlation between the excited state population of potassium and the inter-species collision rate with a bright sodium MOT has also been reported in a study by Sutradhar et al. [181].

Operating potassium in a dark SPOT MOT as well would, therefore, lead to a reduction of light-assisted collisions, as the excited state fraction for potassium would be much lower. However, implementing a dark SPOT MOT configuration for both species would necessitate significant changes to the optical layout on both the laser and experiment table, particularly in terms of separating the cooling and repumping paths for each species. Additionally, the operation of a potassium dark SPOT MOT is complicated by the requirement of high repumping beam powers for ^{39}K laser cooling [188].

Another potential approach involves introducing a slight power imbalance in one of the MOT beam pairs, resulting in a displacement along this beam axis for one of the species [148, 189]. However, this approach may compromise the performance of sub-Doppler cooling and lead to additional heating during the transfer into the magnetic trap due to an imperfect overlap.

An alternative strategy for the dual-species MOT entails loading the two species sequentially using a shelving technique, as introduced in [149, 190] and illustrated in figure 5.3.

In the experimental sequence that is shown in figure 5.3 A, we initiate by loading the sodium MOT. The sodium atoms are then optically pumped for 1 ms to the $|2, 2\rangle$ state using a σ^+-polarized resonant beam that includes cooling and repumping light and a guide magnetic field (generated by offset coils). After the optical pumping stage, the atoms are loaded into a magnetic trap by switching the magnetic field gradient to 100 G/cm. The gradient is subsequently reduced, such that this shallow magnetic trap acts as a spin purification stage. Depending on the value of this shallow trap gradient

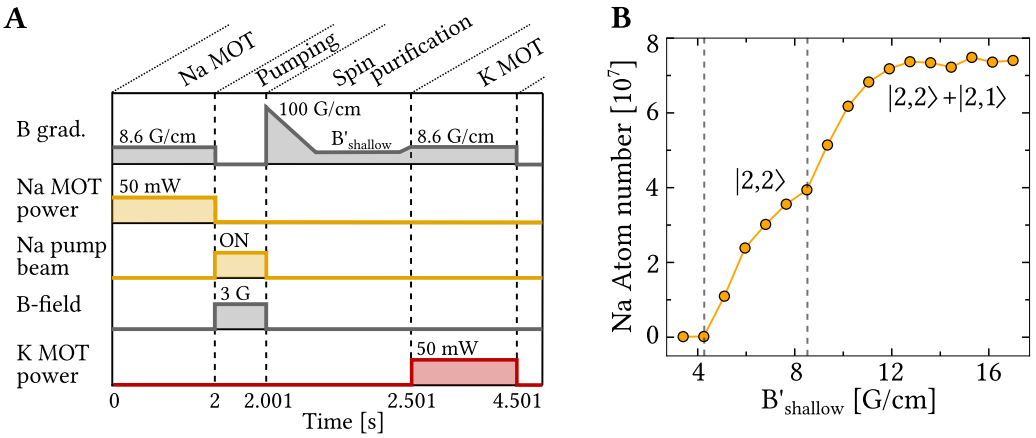

Figure 5.3.: Sequential MOT loading for a sodium potassium mixture. A: Experimental sequence for sequential MOT loading. After the sodium atoms in the MOT are optically pumped to the stretched $|2,2\rangle$ state, they are trapped in a magnetic trap. Following a spin purification stage, the potassium MOT is loaded. B: Sodium atom number after the spin purification stage as a function of the shallow magnetic gradient field B'_{shallow}. For low gradient values in the range 4.25-8.5 G/cm, only the $|2,2\rangle$ state is supported against gravity, while for higher magnetic field gradients, the atoms in the $|2,1\rangle$ state become trappable as well.

B'_{shallow}, only certain spin states remain trapped against gravity. This behaviour is displayed in figure 5.3 B, where we measured the sodium atom number after the 0.5 s long spin purification stage as a function of B'_{shallow}.

Below 4.25 G/cm, no atoms remain as the gradient is too low to compensate gravity. In the range of $4.25 - 8.5$ G/cm, we observe an increase in the number of atoms in the $|2,2\rangle$ state, while above 8.5 G/cm, there is another kink in the atom number as now also the atoms in the $|2,1\rangle$ state become trappable. Consequently, operating at $B'_{\text{shallow}} = 8$ G/cm ensures that atoms in $|2,1\rangle$ are removed from the trap, and one retains a pure spin sample of $|2,2\rangle$ atoms. This step is crucial, as spin imperfections can induce heating and atom loss due to spin relaxation processes. Following this spin purification stage, the potassium 3D-MOT light is switched on, and the potassium MOT is loaded at the MOT gradient of 8.6 G/cm.

While this scheme potentially reduces the impact of light-assisted collisions encountered in a dual-species MOT[2], as reported in [190], we were not able to reliably achieve efficiencies for optical pumping to the $|2,2\rangle$ state exceeding 50 %, as shown in figure 5.3 B. These limitations in optical pumping could be attributed to the high optical den-

[2]As the sodium atoms are shelved in the ground state, primarily light-assisted collisions between excited state sodium and ground state potassium atoms are mitigated.

sities present in the dark-SPOT MOT, with alternative pumping schemes for sodium outlined in [148, 158, 191]. Consequently, the achievement of a sodium BEC in the stretched $|2, 2\rangle$ state using the above-mentioned scheme, even in single-species operation, proved impossible using this promising approach.

In conclusion, the discussed approaches to mitigate the issue of potassium losses in a dual-species MOT each present trade-offs between reducing atom losses and introducing complexities or limitations. To attain dual-species degeneracy, our goal is to cool sodium and utilize it as a sympathetic coolant for potassium. Hence, during the different cooling stages, such as microwave evaporation in the magnetic trap or forced evaporative cooling in the crossed optical dipole trap, primarily sodium atoms are lost from the trap. Consequently, we prioritize ^{23}Na in terms of atom number and temperature and opt for the simple approach of loading both species together, accepting the loss of potassium atoms during the MOT cooling stage.

5.2. Grey molasses cooling

In the magneto-optical trap, the temperatures of both atomic clouds are typically in the order of 250 µK. Utilizing sub-Doppler cooling techniques would be advantageous to further cool down the atomic samples before transferring them into the magnetic trap. Compared to other alkali atoms like rubidium or sodium, potassium has a relatively small energy splitting between its excited states, measuring only 33.8 MHz in total [109]. This characteristic makes cooling below the Doppler temperature difficult and requires the use of alternative cooling techniques such as grey molasses cooling to achieve lower temperatures.

Theory of grey molasses cooling

The grey molasses cooling technique, depicted in figure 5.4 A, combines the principle of Sisyphus cooling with a so-called dark-state $|\psi_D\rangle$ that remains unaddressed by the resonant cooling light. On the other hand, the bright state $|\psi_B\rangle$ is coupled to an excited state through light and experiences a positive light shift. The polarization gradient of the counter-propagating molasses beams creates a spatially modulated potential for the bright state, while the dark state has a flat potential.
In a manner similar to Sisyphus cooling, atoms moving within the sinusoidal potential landscape of the bright state convert their kinetic energy to potential energy by ”climbing” the potential energy maxima. The transition to the excited state becomes most

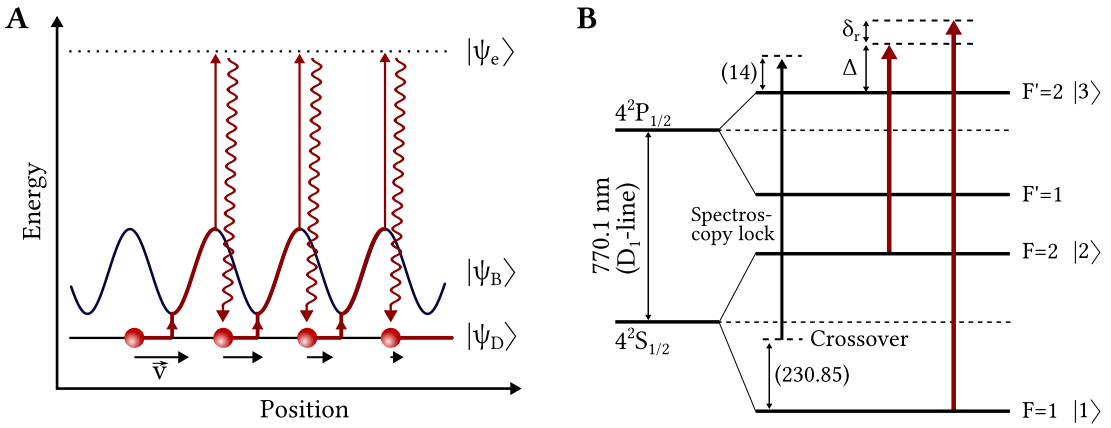

Figure 5.4.: Principle of grey molasses cooling. A: In the dressed three-level system, atoms in the dark state $|\psi_D\rangle$ can motionally couple to the bright state $|\psi_B\rangle$, where they experience a sinusoidally modulated potential. The atoms are pumped back to the dark state after having climbed the potential hill, losing kinetic energy for each cycle. After many such cycles, atoms reach low enough velocities to be trapped in the dark state. Figure adapted from [192]. B: Level scheme for D1 grey molasses cooling of ^{39}K. The lockpoint of the D1 laser is indicated by the vertical black arrow, with AOMs shifting the frequencies to produce a cooling and a repumping beam. The system is operated in a λ-configuration using the two ground states $|1\rangle$, $|2\rangle$ and the excited state $|3\rangle$. The relative detuning between the two beams is denoted by δ_r. When the Raman condition $\delta_r = 0$ is fulfilled, the detuning of both beams with respect to the excited state $|3\rangle$ is given by Δ.

probable once the atom has reached the top of the potential hill. Subsequently, excited atoms can decay back to the dark state via spontaneous emission. Once the atoms are in the dark state, they can either couple to the bright state or remain captured in the dark state. The coupling is controlled via *velocity-selective coherent population trapping* (VSCPT), where the probability of coupling depends on the atom's velocity. The faster the atom, the higher probability is to transition back to the bright state, initiating another cycle of Sisyphus cooling to further reduce their kinetic energy. Consequently, hot and fast atoms will undergo many such cycles of Sisyphus cooling and motional coupling until reaching low enough velocities to be permanently trapped in the dark state [155, 192, 193].

In the context of grey molasses cooling, the emergence of bright and dark states is described using a Λ-system, featuring two ground states $|1\rangle$ and $|2\rangle$, and an excited state $|3\rangle$. The level scheme for potassium, illustrating this Λ-system, is depicted in figure 5.4 B.

The ground states are coupled to the excited state via two laser frequencies in Raman condition, ensuring that the relative detuning of the two beams is zero ($\delta_r = 0$). In the dressed state representation of the atom-light system, the ground state manifold splits into a dark state $|\psi_D\rangle$ and an orthogonal bright state $|\psi_B\rangle$. These states are energy eigenstates of the atom-light system and coherent superpositions of the sub-level states.
It is important to note that achieving a positive light shift, where the bright state is energetically positioned above the dark state, requires blue-detuned light. Conversely, a red-detuning would lead to heating of the atomic cloud.

In practice, the dark state in grey molasses cooling is not completely dark. Due to the complex level structure, it couples slightly to the excited state. However, even with this partial coupling, atoms in the grey state scatter photons with a very low probability. As a result, grey molasses cooling remains an efficient cooling method capable of achieving very low temperatures.
For ^{39}K, the D1-line is utilized for grey molasses cooling. With this approach, temperatures as low as 6 µK have been achieved [132, 194, 195]. Additionally, Colzi et al. [147, 196] successfully implemented this sub-Doppler cooling technique using the D1-line of sodium, cooling the sodium atoms from initial temperatures of 350 µK down to as low as 9 µK.

Microwave spectroscopy

To ensure a slow and isotropic expansion of the atomic cloud during the molasses stage, it is crucial that the zero position of the magnetic field coincides with the position of the atoms. Any residual stray magnetic fields need to be compensated using offset coils placed in the x-, y-, and z-direction around the science chamber.

Figure 5.5 illustrates the implemented microwave spectroscopy technique used to obtain the correct settings for the compensation coils. In this method, sodium atoms are pre-cooled and, after a short magnetic trap stage, transferred into the crossed optical dipole trap. The microwave is set to a specific frequency f_{MW} and turned on. Subsequently, a scan of f_{MW} is conducted just below the $|F = 1\rangle \rightarrow |F = 2\rangle$ zero-field resonance at 1771.63 MHz [108], transferring atoms from the initial $|1, -1\rangle$ state to the states $|2, 0\rangle$, $|2, -1\rangle$, and $|2, -2\rangle$, as shown in figure 5.5 A.
After applying the microwave pulse, we make the transfer visible by blowing away the $|F = 2\rangle$ atoms using resonant cooling light from the imaging path. This enables

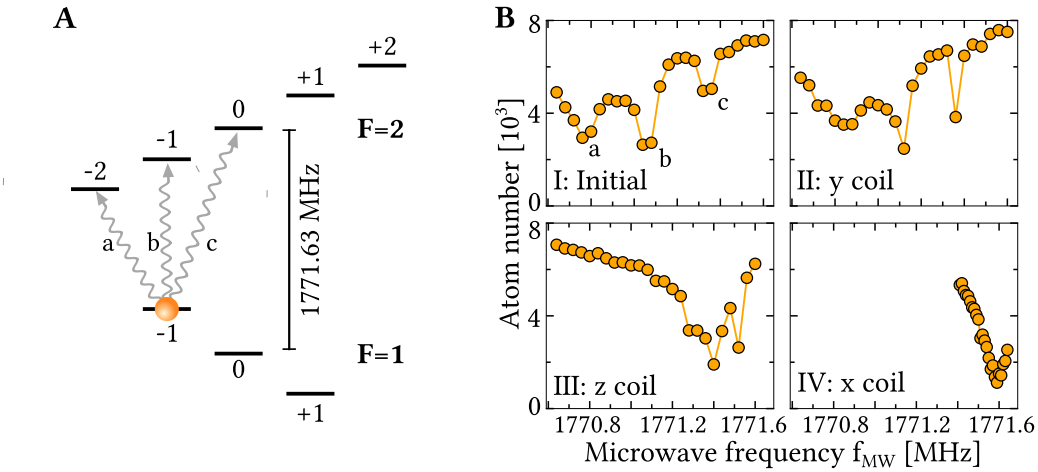

Figure 5.5.: Microwave spectroscopy using offset coils to overlap the magnetic field zero with the position of the sodium atomic cloud. A: Hyperfine level-diagram of the sodium ground state, where the magnetic sub-states are shifted due to the linear Zeeman effect in the presence of magnetic stray fields. Atoms are initially prepared in the $|1,-1\rangle$ state. Microwave pulses, indicated by the wiggly grey arrows, transfer atoms to the $|F=2\rangle$ manifold. B: Sodium atom number as a function of the applied microwave frequency f_{MW}. The top-left graph shows the atom-loss spectrum for the initial offset coil settings. The respective microwave transitions are marked from a to c. While optimizing first the y-coil (plot II), then the z-coil (plot III) and finally the x-coil (plot IV), the resonances move closer together and finally are grouped around the zero-field resonance located at 1771.63 MHz.

the transitions to appear as atom number minima in the subsequent imaging process. Such a microwave frequency scan is presented in the top-left graph of figure 5.5 B.

The distinct frequencies corresponding to the transfer of sodium atoms to the $|2,-2\rangle$, $|2,-1\rangle$, and $|2,0\rangle$ states during microwave spectroscopy, labelled as minima a, b, and c, respectively, were observed at approximately 1770.8 MHz, 1771.1 MHz, and 1771.4 MHz. This separation in frequencies indicates the presence of residual magnetic fields in the vicinity of the atoms during the spectroscopy measurement. Specifically, the initial magnetic bias field at these settings can be estimated to be approximately 0.4 G.

To compensate for this bias field, we first optimized the current running through the y-coil. The objective was to reduce the separation of the atom number minima and align them closer to the theoretical zero-field resonance at 1771.63 MHz. Through systematic adjustments of the three coil pairs, the minima were overlapped, coinciding with the zero-field resonance position, as shown in bottom-right graph of figure 5.5 B. The optimized settings for the three offset coils are summarized in table 5.1.

Table 5.1.: Optimized offset coil settings. The magnetic field values were obtained from the measured calibration factors reported in table 3.3.

	x-coil	y-coil	z-coil
Current [A]	0.05	0.1	0.25
Magnetic field [G]	0.09	0.19	0.41

Implementation and optimization

In the implemented grey molasses cooling method, the cooling and repumping beams operate in a Λ-configuration and are detuned according to the Raman condition. The D1 light for these purposes is coupled into the same fibre that supplies the D2 laser light for the magneto-optical trap, such that the splitting and alignment of the six counter-propagating beams are already taken care of.
The polarization gradient, vital for the Sisyphus cooling technique, is created by these counter-propagating circularly polarized D1 laser beams. Approximately 30 mW of D1 cooling light is utilized, while the D1 repumper carries roughly 13 mW of power.

Figure 5.6 illustrates our implemented experimental sequence for grey molasses cooling of ^{39}K. The process initiates with loading the magneto-optical trap for 4 s using D2 light and a magnetic field gradient of 8.6 G/cm. After this loading period, both the magnetic field gradient and the D2 light are abruptly switched off. The molasses stage, lasting 4.9 ms in total, follows this turn off and is divided into two steps.
The first steps involves a 2.1 ms duration, during which the D1 light is turned on and maintained at a constant intensity and detuning. Following this, a linear frequency ramp is executed over 2.8 ms, shifting towards higher detunings while retaining the Raman condition. Simultaneously, the intensities are linearly reduced to ensure that atoms remain within the capture range of the cooling process, facilitating a decrease in temperature. The parameters of this ramp, including the speed and the initial and final values, were optimized by evaluating the resulting temperature and atom number of the cooled atomic cloud.

To enhance the performance of the grey molasses cooling process, we conducted a series of optimization measurements, the results of which are depicted in figure 5.7. Following the grey molasses cooling stage, we image the atoms using the coarse absorption imaging setup with a 15 ms time-of-flight (TOF) and extract both the atom number N_{at} and the Gaussian width σ of the atomic cloud. The width after a 15 ms

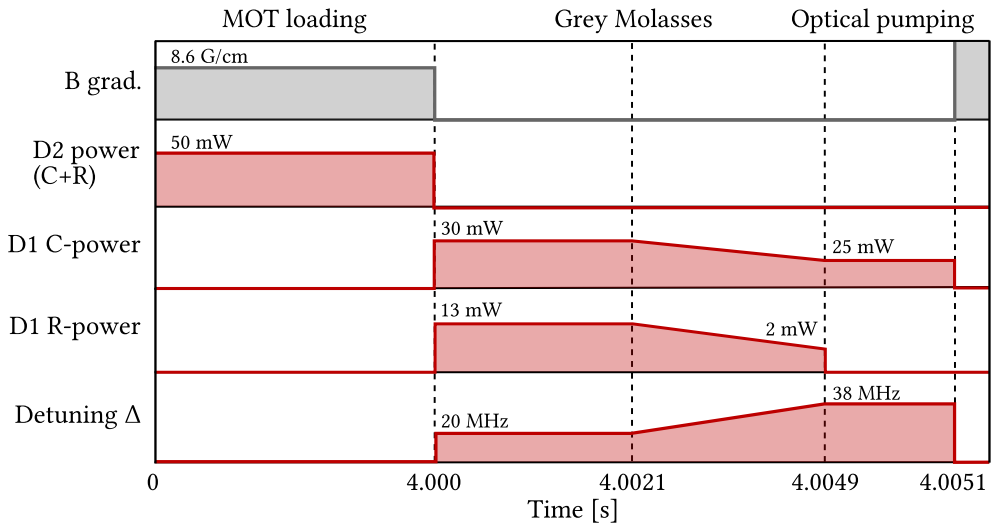

Figure 5.6.: Experimental sequence for grey molasses cooling of ^{39}K atoms. After the MOT has been loaded for 4 s, the magnetic field gradient and D2 laser power are switched off, and the D1 light is turned on. In a two-stage process, the power and detuning are firstly held for 2.1 ms at a constant value. These parameters are then ramped to larger detunings and lower intensities within 2.8 ms. Finally, before initiating the transfer into the magnetic trap, the atoms are pumped to the $|F = 1\rangle$ hyperfine ground state by turning off the repumping light for 200 µs.

TOF serves as a reliable estimator for the cloud's temperature. High phase-space densities, which are the ultimate optimization goal for the grey molasses, require high atom numbers and low temperatures. Thus, with a maximum in the atom number and a minimum in the distribution width, the optimal hold time and sweep time were found to be 2.1 ms and 2.8 ms, respectively.

Moreover, we conducted a scan of the Raman detuning δ_r (depicted in panel C of figure 5.7). This scan revealed a clear minimum in the cloud width at $\delta_r = 0.17$ MHz, indicating an optimal cooling condition, while we observed strong heating effects towards larger blue detuning. For the implemented intensity ratio between cooler and repumper of approximately 3:1, such an asymmetric Fano profile in the temperature for larger detunings results from interferences of different excitation pathways and has been reported in [194, 196].

Additionally, deviations from the Raman condition, i.e. the fact that $\delta_r \neq 0$, might stem from stray magnetic fields following the abrupt turn-off of the magnetic field coils. Furthermore, the calibration of the offset coils to compensate for the stray magnetic fields was carried out utilizing microwave spectroscopy of sodium in the optical dipole trap. A potential misalignment of the position of the dipole trap with respect

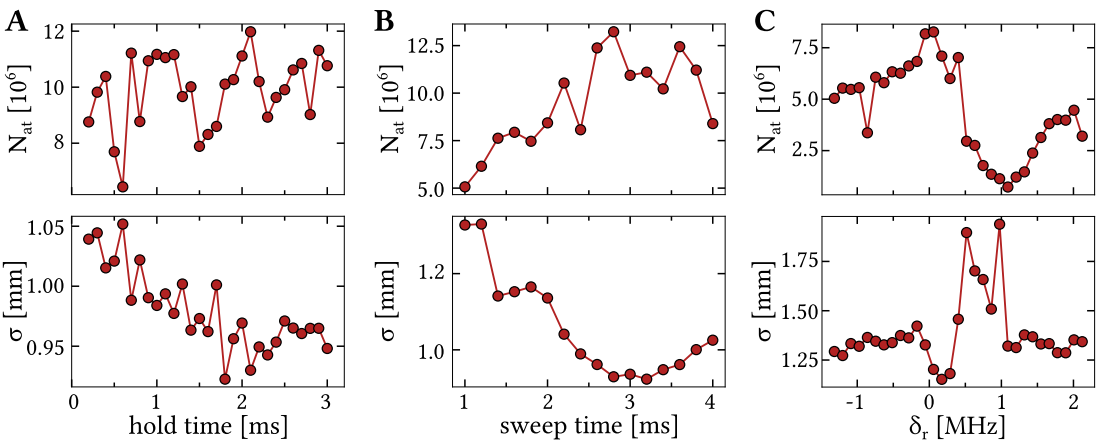

Figure 5.7.: Optimization of grey molasses parameters with respect to atom number N_{at} and width σ after a 15 ms time-of-flight. The graphs show the dependence on the hold time (A), sweep time (B) and Raman detuning δ_r (C).

to the potassium grey molasses might add to the slight deviation from the theoretical Raman condition. Further investigations and adjustments are needed to account for these effects and achieve optimal cooling conditions.

While this cooling method is highly sensitive to changes in the relative detuning between the two beams, which sets the Raman condition, the overall blue-detuning Δ before and after the ramp is less critical. To set the detuning of the two beams, we use two separate analog output ports of the computer-control system that adjust the RF-frequency of the AOMs. During the cooling cycle, these frequencies are tuned and ramped in unison from $\Delta_{start} = 20$ MHz to $\Delta_{end} = 38$ MHz, ensuring that the Raman condition is indirectly satisfied.

However, for precise and active maintenance of the Raman condition throughout the entire ramping process, a different approach would have to be implemented. Using an external reference signal to set the Raman condition has demonstrated long-term stability on a neighbouring potassium experiment with achieved temperatures as low as 8 µK [132, 197]. In this method, the RF-signal from a voltage-controlled oscillator (VCO) drives the cooling AOM, while the RF-signal for the repumping AOM is generated by mixing the VCO-signal with the stable external frequency reference. Since the AOMs are operated in a double-pass configuration and the laser is locked to the ground state crossover, the reference signal would have to be set to 230.85 MHz.

For our implemented grey molasses scheme, we recently experienced difficulties with performance fluctuations. Therefore, this alternative approach presents a simple solution to improve the stability and consistently achieve sub 10 µK temperatures.

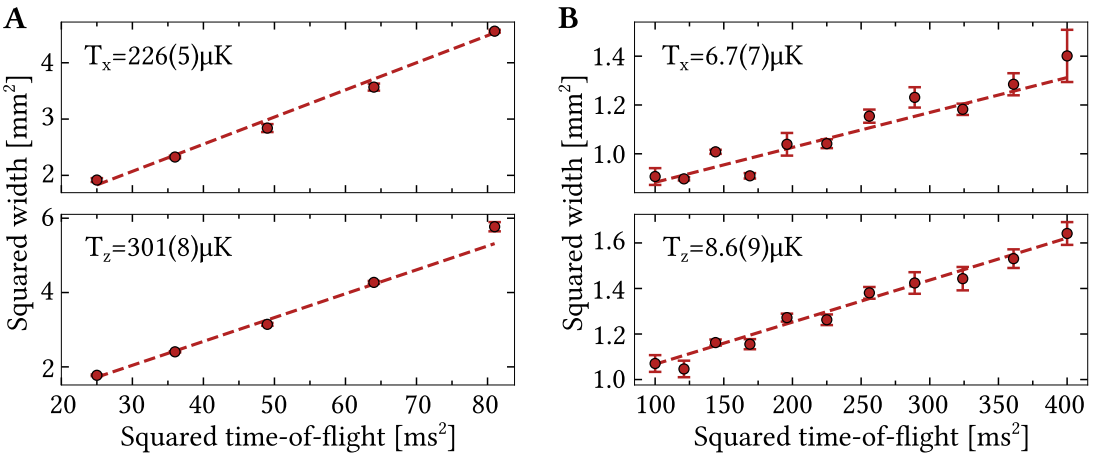

Figure 5.8.: Time-of-flight (TOF) measurements to determine the temperature of the ^{39}K cloud following the MOT (A) and grey molasses (B). Three averages were performed for each TOF setting. The temperature is extracted from the slope of the squared Gaussian width of the atomic cloud versus squared time-of-flight, according to equation 3.4. A: Time-of-flight measurement of the potassium MOT with temperatures in x- (top graph) and z-direction (bottom graph). B: Time-of-flight measurement of the potassium grey molasses with temperatures in x- (top graph) and z-direction (bottom graph).

After optimizing the different parameters of the grey molasses, its cooling performance has to be evaluated. To assess the achieved temperatures of the atomic sample, time-of-flight measurements were conducted, and the results are presented in figure 5.8.

The initial temperature of the potassium magneto-optical trap was determined to be 226(5) μK in the x-direction and 301(8) μK in the z-direction, as illustrated in figure 5.8 A. In contrast, with the implementation of the grey molasses cooling technique, a drastic reduction in temperature was observed, as shown in figure 5.8 B. The achieved temperatures were as low as 6.7(7) μK in the x-direction and 8.6(9) μK in the z-direction.

Up to now, we applied grey molasses cooling exclusively to potassium. Implementing this cooling technique for sodium would necessitate modifications to the existing sodium laser setup. Specifically, an additional 589 nm laser source, frequency-stabilized to the D1-transition, would need to be incorporated to generate the required cooling and repumping light. While grey molasses cooling with sodium has proven to provide a tenfold increase in the phase-space density compared to a regular red-detuned optical molasses [196], its performance in dual-species operation still has to be reviewed.

Following the sub-Doppler cooling stage, the atoms are transferred to the magnetic quadrupole trap. Analogous to single-species operation with sodium, as described in section 4.2, microwave evaporation is performed in the hybrid trap. Hereby, sodium atoms are selectively evaporated, while the potassium atoms are sympathetically cooled through collisional thermalization with the cold sodium atoms [20, 198]. Both species are subsequently loaded into the crossed optical dipole trap by ramping down the magnetic field gradient.

5.3. Two-species optical trapping

In the crossed optical dipole trap, there are some notable differences in the trapping behaviour of the two atomic species.

As outlined in section 4.3, the optical trapping potential experienced by the atoms depends on the real part of the dynamic polarizability $\mathrm{Re}(\alpha)$, which is a function of the atom's transition wavelength. When considering both D1- and D2-transitions [170], the polarizability for the two species is shown in figure 5.9 A, exhibiting resonances at the transition wavelengths of approximately 589 nm and 767 nm. Notably, in the infra-red spectrum, potassium atoms experience a deeper trapping potential compared to sodium.

Additionally, the trapping frequency depends on the mass of the atomic species. Consequently, following equation 4.9, the ratio of the trapping frequencies is given by:

$$\frac{\omega_{\mathrm{K}}}{\omega_{\mathrm{Na}}} = \sqrt{\frac{\mathrm{Re}(\alpha_{\mathrm{K}})}{\mathrm{Re}(\alpha_{\mathrm{Na}})}\frac{m_{\mathrm{Na}}}{m_{\mathrm{K}}}} \tag{5.3}$$

For an optical dipole trap, operated at a wavelength of 1070 nm, the mass imbalance between ^{23}Na and ^{39}K counteracts the difference in the trapping potential. Consequently, this compensation effect leads to a reduced ratio of trapping frequencies, specifically $\omega_{\mathrm{K}}/\omega_{\mathrm{Na}} = 1.23$. The wavelength at which this ratio would equal unity is referred to as a *magic wavelength*. However, as displayed in the bottom graph of figure 5.9 A, the ^{23}Na-^{39}K mixture does not possess such a magic wavelength.

When considering the influence of the gravitational potential, unequal trapping frequencies give rise to a differential gravitational sag, which is depicted in figure 5.9 B. The effect of gravity alters the trapping potentials, tilting them and shifting their respective minima. Consequently, the atomic clouds experience a relative displacement

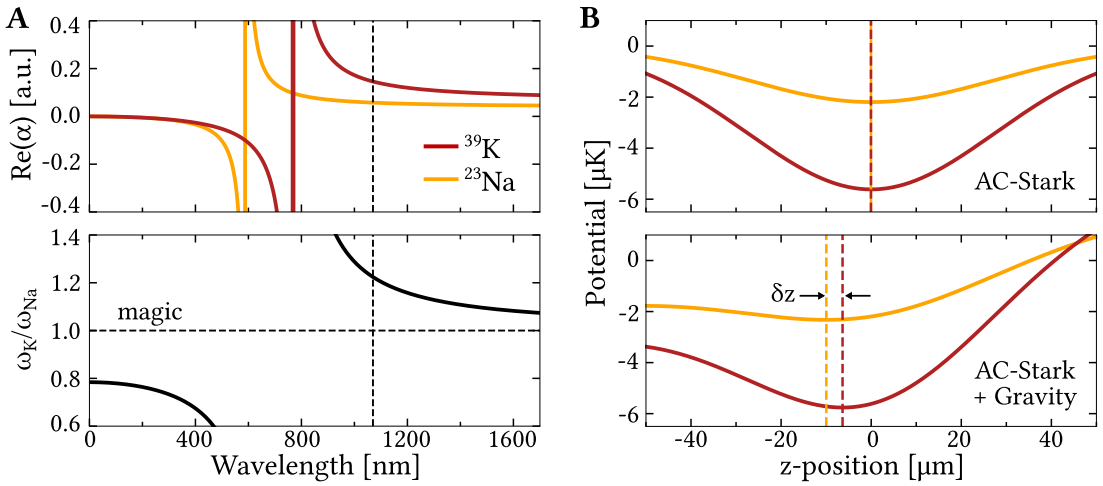

Figure 5.9.: Dual-species optical trapping of sodium and potassium. A: Atomic polarizability for ^{23}Na and ^{39}K, and trapping frequency ratio as a function of the trapping laser wavelength. The vertical dashed line marks the 1070 nm laser that has been chosen for this experiment, while the horizontal line indicates the magic condition, where the trapping frequencies of the two species would be equal. As evident from the plot, this mixture does not possess a magic wavelength. B: Trapping potential both in the absence and presence of the gravitational potential. The disparity in trapping frequencies between the two species induces a differential gravitational sag, denoted as δz. In this example, a sodium trapping frequency of 160 Hz resulted in a differential sag of $\delta z = 3.2\,\mu$m.

along the z-direction by δz. An exemplary sodium trapping frequency of 160 Hz, as shown in the graph, leads to a relative displacement of 3.2 μm.

Notably, as the trapping frequency is increased, leading to enhanced confinement of atoms along the gravity direction, this shift is significantly reduced, as demonstrated in figure 5.10. On the contrary, at lower trapping frequencies, the positional displacement can reach values ranging from $10 - 1000\,\mu$m, which would negatively affect the spatial overlap between the two atomic species.

To assess the significance of the differential gravitational sag, we compare it with the Thomas-Fermi radius R_{TF}, a measure of the condensate size. We plot R_{TF} for 10^5 sodium atoms as a function of the trapping frequency and observe a crossing of the two curves at approximately 90 Hz. Consequently, at low trapping frequencies typical after forced evaporative cooling, the spatial overlap between the two clouds is reduced, strongly diminishing the inter-species rethermalization rate and, thus, ren-

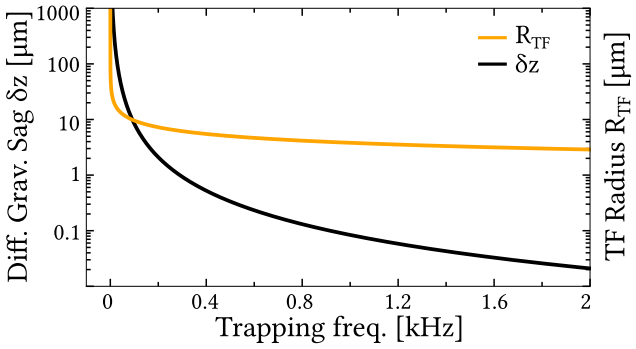

Figure 5.10.: ^{23}Na-^{39}K differential gravitational sag and sodium Thomas-Fermi (TF) radius as a function of the trapping frequency. The Thomas-Fermi radius was calculated with 10^5 sodium atoms.

dering sympathetic cooling between the two components inefficient[3]. Hence, if there is a disparity in temperatures ($T_{Na} \neq T_K$) following evaporative cooling in the dipole trap, the trapping frequency could be subsequently adiabatically increased to ensure rethermalization between the two atomic species.

To mitigate the issues posed by the differential gravitational sag, several strategies can be considered. As discussed earlier, the use of a magic wavelength, where the two trapping frequencies are equal, is not an option for the ^{23}Na-^{39}K mixture. Nevertheless, a magic wavelength could be synthesized through a combination of different wavelengths. In addition to the 1070 nm light (power P_1), introducing a second wavelength that is repulsive for sodium but attractive for potassium would be required. Thus, an additional helium–neon laser at a wavelength of 632.4 nm, with a power of $0.08 \times P_1$, could be used to counteract the displacement [100].

Another approach involves implementing a technique known as *magnetic levitation* [200, 201]. This method utilizes a vertical magnetic field gradient in combination with differing magnetic moments of the two species to cancel the gravitational force, resulting in the levitation of both atomic clouds [202, 203]. The mixture $(|1,-1\rangle_{Na} + |1,-1\rangle_K)$, operated at a bias field of 150 G, would require a levitation gradient of approximately 3 G/cm to compensate the gravitational sag between the two species.

Lastly, adopting a strongly asymmetric trapping potential with strong confinement in the vertical gravity direction can diminish the impact of this differential sag. Such a two-dimensional trapping geometry will be implemented in the near future. An additional attractive infra-red laser beam, shaped into a sheet of light (surfboard ge-

[3]The quantitative impact of spatial overlap on the efficiency of sympathetic cooling has been analysed in [199].

ometry) using a cylindrical lens, will be utilized. Along the z-direction, the beam will be focused down to 20 µm, generating trapping frequencies of approximately 1 kHz, thereby limiting the relative displacement to below 100 nm. Further details regarding the layout and characterization of this optical trap are described in Lilo Höcker's Ph.D. dissertation [126].

5.4. Feshbach spectroscopy

In the crossed optical dipole trap, both inter- and intra-species scattering properties become notably significant due to the high atomic densities. The s-wave scattering length, governing homo- and hetero-nuclear collisions, can be finely adjusted via magnetically tunable Feshbach resonances, as reviewed in section 2.2. In the context of the ^{23}Na-^{39}K atomic mixture, the collisional properties prove advantageous, and Feshbach resonances have been reported to occur at relatively low magnetic bias fields, as detailed in section 2.3.
In order to effectively map out and utilize the intra- and inter-species Feshbach resonances within our experimental apparatus, a magnetic bias field is applied. Our initial numerical simulations have provided us with a preliminary calibration of the magnetic field versus coil current. However, to precisely control the interaction strength using magnetically tunable Feshbach resonances, we require a precise calibration of the magnetic field experienced by the atoms as a function of the supplied electric current to the magnetic field coils.

5.4.1. Magnetic field calibration

In the presence of an external magnetic field, the internal energy levels of the atoms are shifted. When magnetic fields are sufficiently weak, the *Zeeman interaction* can be regarded as a perturbation to the $|F, m_F\rangle$ basis, inducing an energy shift that is linear in the magnetic quantum number m_F. In the case of strong magnetic fields (*Paschen-Back regime*), the coupling between the nuclear spin and the orbital angular momentum is disrupted, such that they couple more strongly to the external magnetic field. Consequently, the basis $|m_I, m_J\rangle$ must be used in this regime. However, in the intermediate regime, the quantitative behaviour is generally more complex and not as straightforward to describe.
For the ground state ($J = 1/2$), the Hamiltonian governing the system can be solved analytically, such that the internal energies are shifted in the presence of an external

magnetic field B according to the *Breit-Rabi formula* [108, 204]:

$$E(B)_{F=I\pm1/2} = -\frac{\Delta E_{\mathrm{hfs}}}{2(2I+1)} + g_I \mu_B m_F B \pm \frac{\Delta E_{\mathrm{hfs}}}{2}\sqrt{1+\frac{4m_F x}{2I+1}+x^2} \tag{5.4}$$

where $\Delta E_{\mathrm{hfs}} = A_{\mathrm{hfs}}(I+1/2)$ is the splitting between the two hyperfine states with the hyperfine structure constant A_{hfs}, and x is determined by

$$x = \frac{(g_J - g_I)\,\mu_B B}{\Delta E_{\mathrm{hfs}}} \tag{5.5}$$

with the nuclear spin I, the total orbital angular momentum $J = 1/2$, and the corresponding g-factors g_I and g_J. The Breit-Rabi diagram for sodium is illustrated in the upper graph of figure 5.12.

We calibrated the magnetic bias field using microwave spectroscopy of sodium atoms, trapped in the crossed optical dipole trap (cODT), employing the transition from $|1,-1\rangle$ to the $|2,0\rangle$ state. The experimental sequence, as illustrated in figure 5.11, involves transferring sodium atoms from the magnetic trap to the cODT. Once the magnetic field gradient is turned off, the coils are switched to Helmholtz configuration using

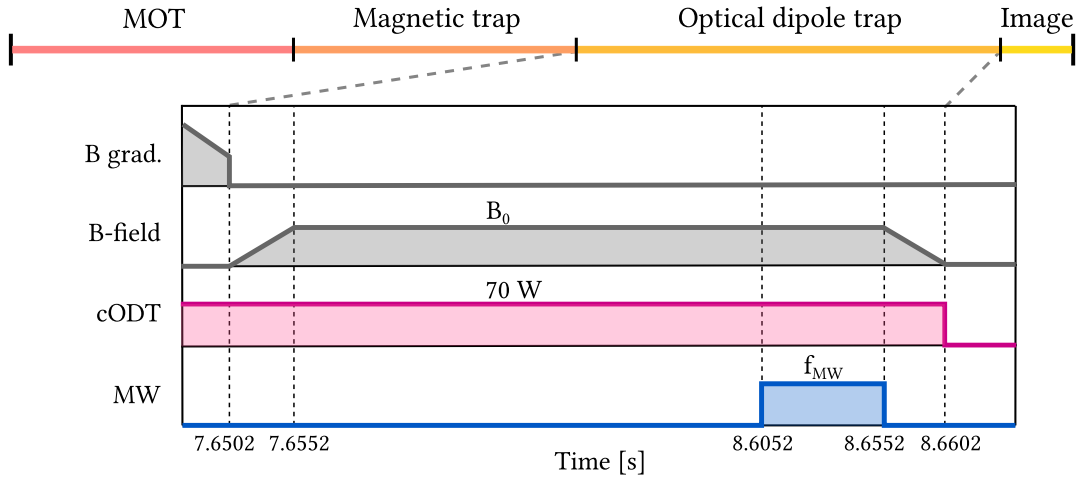

Figure 5.11.: Experimental sequence for microwave spectroscopy of sodium atoms. Following the transfer of sodium atoms from the hybrid trap to the cODT, the bias magnetic field is ramped up to a value B_0 and maintained at this level for 1 s. During the final 50 ms of this period, a microwave (MW) pulse at a fixed frequency f_{MW} is turned on. For the spectroscopy measurement, B_0 is systematically scanned across a particular resonance for each distinct value of f_{MW}.

the H-bridge. The electric current running through the Feshbach coils is rapidly increased within 5 ms to a specific value I_0, corresponding to a bias magnetic field B_0, which is systematically scanned during the measurement. The atoms are held at this bias field B_0 for 1 s, and during the last 50 ms, a microwave pulse with frequency f_{MW} is applied. Following a brief 0.1 ms time-of-flight, the atoms are subsequently imaged using the horizontal high-resolution absorption imaging system.

In the experiment, we record the atom number as a function of the coil current for various microwave frequency settings. Two exemplary measurement results, illustrating this relationship, are presented in the middle graphs in figure 5.12. When the resonance condition is met, atoms undergo a transfer to the $|2, 0\rangle$ state, resulting in rapid inelastic losses in this high density regime [157]. Consequently, we observe a minimum in the atom number when imaging the atomic cloud.

For each microwave frequency setting, we identify the corresponding coil current value at which the transfer is maximized. Using the Breit-Rabi formula (equation 5.4), we can convert the microwave frequency into a magnetic field value. The resulting calibration curve, depicting the magnetic field as a function of coil current, is presented in the lower graph of figure 5.12.

Table 5.2 provides a summary of the calibration parameters, detailing the magnetic field in relation to coil current and control voltage (internal computer control setting). The slope of bias field versus coil current agrees well with the calculated value of 2.0 G/A obtained from the numerical simulations in section 3.3.2, considering that the exact shape of the coil and the respective windings were not taken into account for the simulation. However, the magnetic field offset is not precisely 0 G, but rather at $-0.95(2)$ G. This discrepancy can be attributed to the fact that this measurement was conducted prior to the offset field compensation for the grey molasses cooling method, with the result that the compensation coils introduced some offset field.

Table 5.2.: Summary of microwave calibration results illustrating dependence of magnetic bias field versus coil current and control voltage (internal computer control setting).

	Slope	Offset
B vs current	1.9692(2) G/A	−0.95(2) G
B vs control voltage	64.984(7) G/V	−0.95(2) G

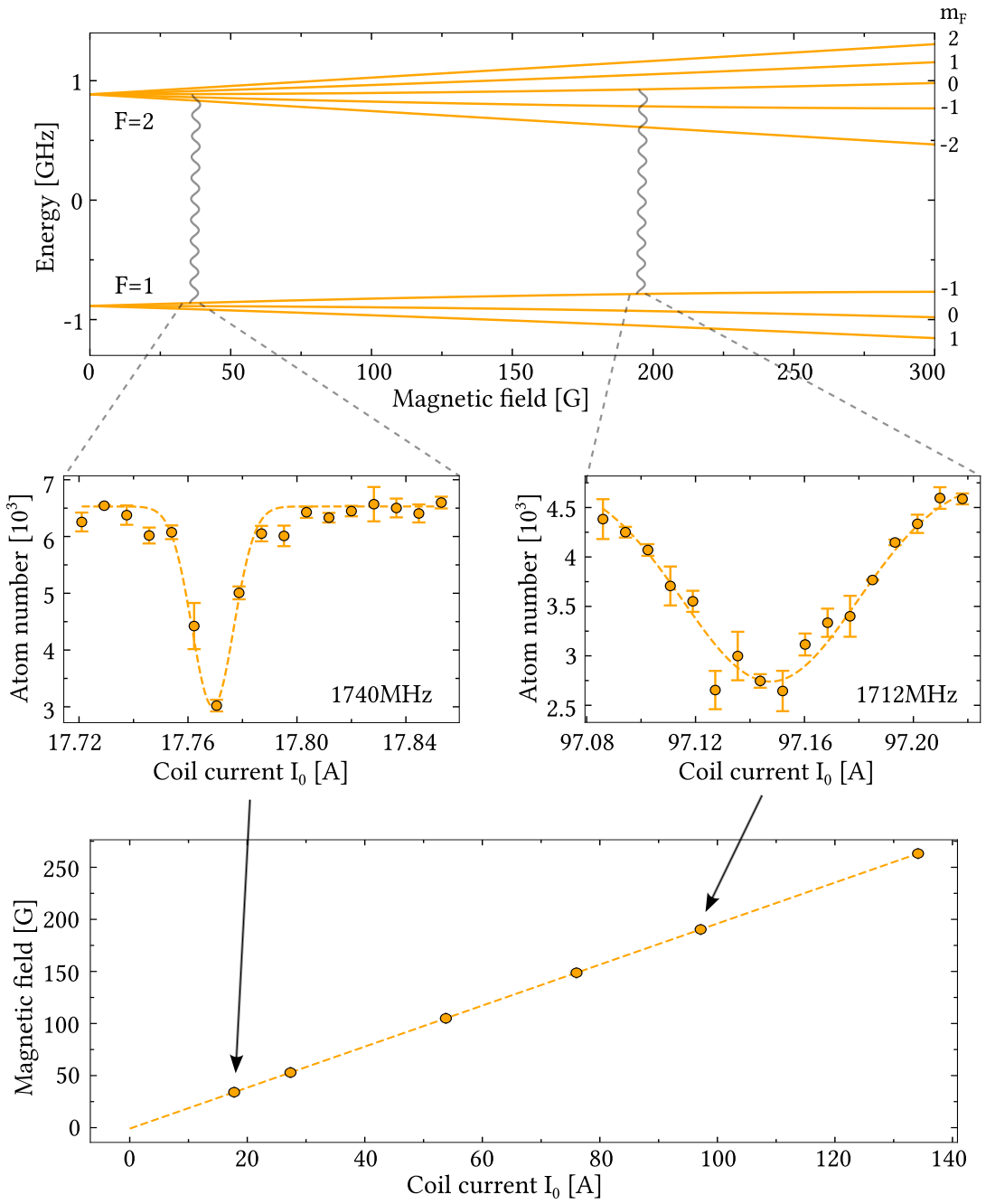

Figure 5.12.: Calibration of the bias magnetic field using microwave spectroscopy of ^{23}Na. The upper graph shows the Breit-Rabi diagram for the hyperfine ground states of sodium within a magnetic field range up to 300 G. In the two middle plots, atom-loss spectroscopy measurements (average atom number over three experimental realizations) are presented. At a fixed microwave frequency, the coil current is scanned across the resonance for the transition from $|1,-1\rangle$ to $|2,0\rangle$, as indicated by wiggly lines in the upper graph. Using the Breit-Rabi formula (upper graph), the microwave frequency for each scan can be translated into a magnetic field value, finally resulting in the lower calibration graph. This graph presents the magnetic field the atoms experience as a function of the supplied coil current.

Having applied this calibration, we can now study the magnetically tunable intra- and inter-species Feshbach resonances. An extensive knowledge of the ^{23}Na-^{39}K homo- and hetero-nuclear scattering properties is essential for achieving dual-species condensation and is fundamental in the study of demixing dynamics, where precise knowledge of the mixture's miscibility is required.

5.4.2. ^{39}K Feshbach spectrum

To gain a comprehensive understanding of the scattering properties of the Na-K mixture, it is essential to study the characteristics of each individual species independently. This will help us to differentiate between effects related to homo-nuclear and hetero-nuclear collisions.

For sodium in the $|1,-1\rangle$ state, there exists a wide intra-species Feshbach resonance at a magnetic field strength of 1195 G [94, 95]. However, at lower magnetic fields, the s-wave scattering length maintains a constant value of $52\,a_0$.

On the other hand, homo-nuclear ^{39}K collisions display several broad s-wave resonances at low magnetic fields [96–98, 205], as illustrated in the upper graph of figure 5.13. The high field resonance at 560.9 G has been omitted, as the magnetic field range of interest for dual-species condensation lies between the two low-field resonances. In this range, the Na-K mixture displays both miscible and immiscible regions, as further elaborated in subsection 5.4.3.

To map out these resonances within our experimental system, we performed atom-loss spectroscopy on potassium. The corresponding experimental sequence involved loading both species into the magnetic trap, where we cooled sodium using microwave evaporation, while potassium was cooled sympathetically. Subsequently, the atoms were loaded into the crossed optical dipole trap, and any remaining sodium atoms were selectively removed using a resonant laser beam. The bias magnetic field was then swiftly ramped up to a specific value, B_0, within 5 ms, and maintained at this level for 2 s. At the end of this sequence, both the magnetic field and the dipole trap were turned off, and the atomic cloud was imaged following a brief time-of-flight of 0.1 ms using the fine absorption imaging system.

The Feshbach spectrum was obtained through a scan of the magnetic field B_0 across the respective resonance. On resonance, the enhancement of inelastic three-body losses results in a dip in the atom number signal. The two lower plots in figure 5.13 illustrate the results of atom-loss measurements for the two low-field resonances, where the

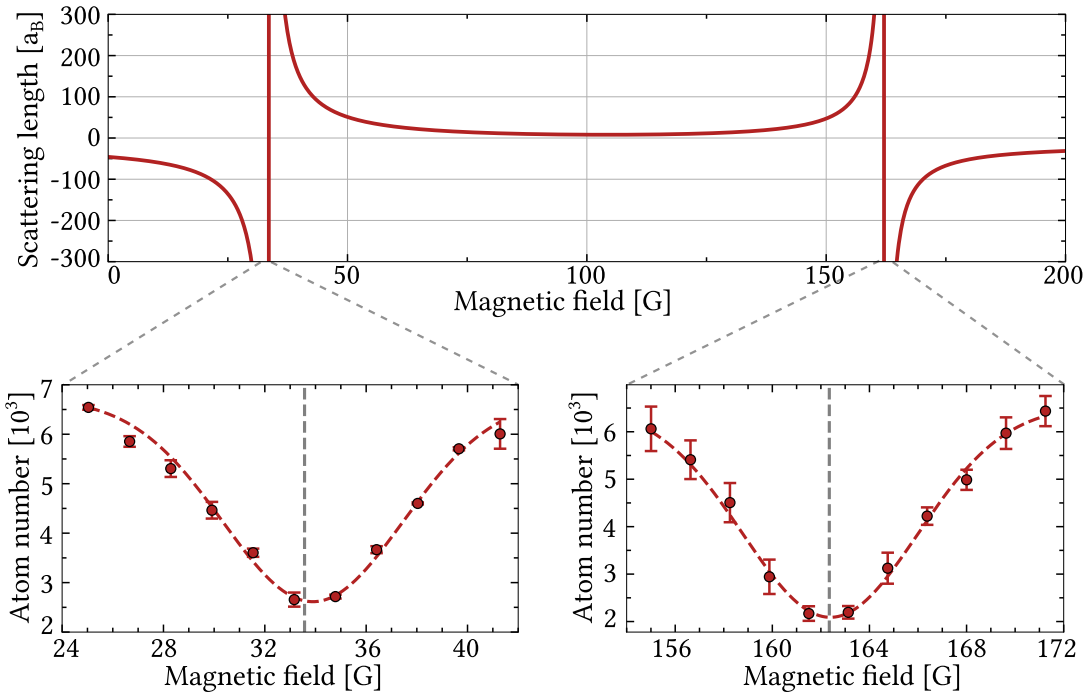

Figure 5.13.: Homonuclear ^{39}K Feshbach spectrum for the $|1,-1\rangle$ state. The upper graph shows the s-wave scattering length for $\left(|1,-1\rangle_K + |1,-1\rangle_K\right)$ collisions as a function of the external magnetic field, revealing the presence of two low-field resonances. Plotted using parameters reported in [96]. Lower graphs: Atom-loss spectroscopy measurements conducted across the two resonances. The red dashed lines are Gaussian fits to the experimental data, providing the locations of the resonances. The grey dashed lines present theoretical predictions [98] for the resonance locations.

atom number is given as an average over three experimental realizations. Gaussian fitting of the data provided the precise magnetic field locations of the two resonances. These results are summarized in table 5.3. The experimental errors combine fit errors with the uncertainties resulting from the magnetic field calibration.

A comparison with results obtained by D'Errico et al. [96] reveals good agreement within the specified error margins. However, slight deviations become apparent when comparing with more recent, high-precision characterization data presented in [98]. These discrepancies can be attributed to additional systematic error sources, such as the high temperatures of the atomic cloud during the conducted measurements, which can shift the resonance locations. Furthermore, the long-term magnetic field stability with respect to the initial calibration necessitates further investigation[4].

[4]Given the potential day-to-day variations in the background magnetic field, it is crucial to regularly recalibrate the magnetic bias field to ensure the accuracy of the measurements.

Table 5.3.: ^{39}K Feshbach resonance locations for $\left(|1,-1\rangle_K + |1,-1\rangle_K\right)$ collisions. We compare our experimentally extracted values from figure 5.13 (left column) to other experimental data [96, 98] and theoretical predictions [98]. The theoretical values are also displayed in figure 5.13 as grey dashed lines.

B_{exp} (G)	B_{exp} (G) [96]	B_{exp} (G) [98]	B_{theo} (G) [98]
33.9(1)	32.6(1.5)	33.5820(14)	33.568
162.4(2)	162.8(9)	162.36(2)	162.347

Additional loss feature

The potassium Feshbach spectrum, as displayed in the upper graph of figure 5.13, does not reveal any further s-wave resonances between the two low-field resonances. However, during a comprehensive magnetic field scan spanning from 0 G to 200 G, where we held the atoms at each magnetic field value for 200 ms, an unexpected loss feature was observed. This distinctive feature is prominently shown in the top graph of figure 5.14, exhibiting a broad and strong loss signal at approximately 110 G[5].

[5]This data set was acquired when operating the dipole trap at 40 W (total power for both beams).

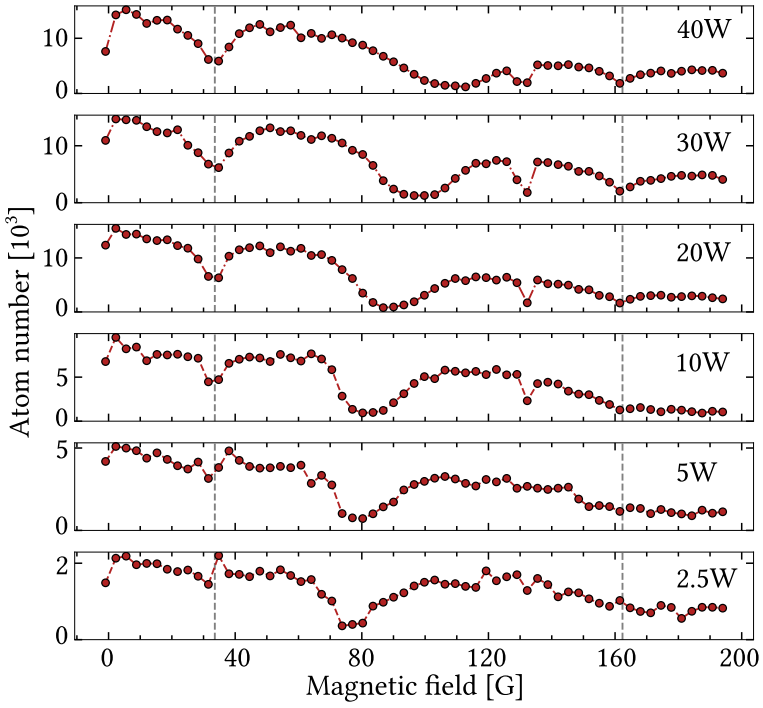

Figure 5.14.: Atom-loss spectroscopy of ^{39}K across a magnetic field range spanning from 0 G to 200 G at various dipole trap powers. The positions of the two Feshbach resonances are indicated by the grey dashed lines.

Subsequent measurements at different dipole trap power settings provided valuable insights. Firstly, reductions in atom losses attributed to the Feshbach resonances, indicated by vertical dashed grey lines in figure 5.14, were observed, correlating with a decreased atom density as the dipole trap confinement was reduced. Secondly, a significant shift of the central loss feature towards lower magnetic fields was detected. Based on these two observations, we can exclude any connection with higher-order Feshbach resonances.

To investigate this phenomenon further, we set the dipole power to a constant value of 30 W. Once again, a magnetic field scan was conducted, but this time with a hold time of 60 ms, and employing a state-selective imaging process. The two hyperfine ground states, $|F = 1\rangle$ and $|F = 2\rangle$, were selectively imaged by utilizing either cooling or repumping light for the imaging process. The corresponding spectrum for the two states is shown in figure 5.15 A. Notably, the initial expectation was a complete absence of atoms in the $|F = 2\rangle$ state, as the atoms were pumped to the $|F = 1\rangle$ state before being loaded into the magnetic trap. However, contrary to this expectation, we observed a discernible population transfer to the $|F = 2\rangle$ state at the position of the atom-loss resonance.

This transfer is further illustrated in figure 5.15 B, where we fixed the magnetic bias field to the location of the loss feature (100 G at 30 W dipole power) and subsequently scanned the hold time. The rapid initial increase of the $|F = 2\rangle$ population is followed

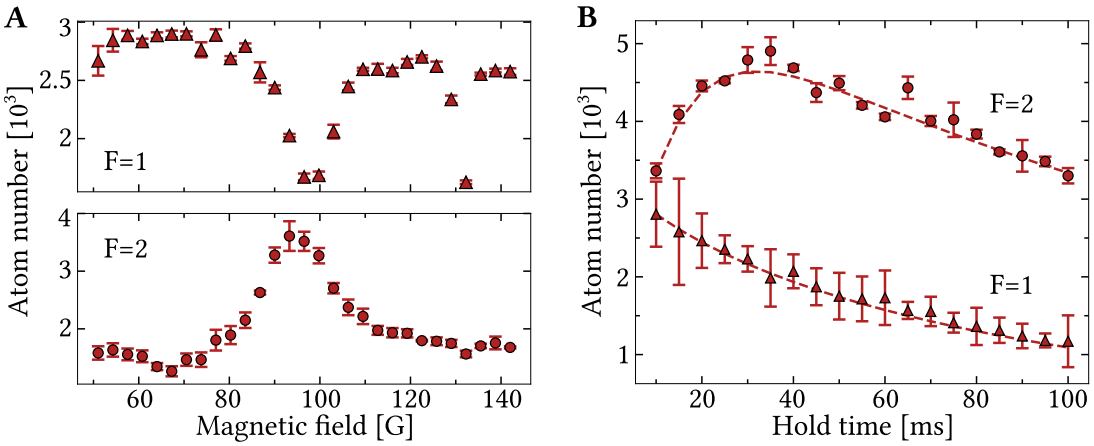

Figure 5.15.: Evolution of ground state populations at the magnetic field location of the additional loss feature. A: Hyperfine populations as a function of the bias magnetic field for a fixed hold time of 60 ms. B: Temporal evolution of the population in the $|F = 1\rangle$ and $|F = 2\rangle$ hyperfine ground states, operated at a fixed bias field of 100 G.

by a decay, attributed to two-body collisions involving $|F = 2\rangle$ atoms. The dashed lines represent fits to the experimental data using solutions to a simplified rate equation model [206].
In conclusion, our observations indicate that atoms undergo a transfer to the $|F = 2\rangle$ state, where they subsequently experience increased two-body collisions, leading to atom loss from the trap. However, these findings still do not provide insights into the underlying cause of this transfer.

Interestingly, similar effects have been documented in other experiments [206–210] utilizing a similar multi-frequency dipole laser[6]. These studies identified two-photon Raman transitions induced by different modes of the multi-frequency laser as the primary cause of atom transfer to the $|F = 2\rangle$ state, where a higher two-body loss rate resulted in a fast decay in atom number.
Consequently, we conducted a closer examination of our dipole laser, measuring its power spectrum using a fast photodiode, as depicted in figure 5.16. The multi-frequency character of the laser is revealed by the equidistant peak structure, with a mode-spacing of 5.8 MHz.
In an attempt to find out whether the multi-mode spectrum of our dipole laser was causing the observed atom losses, we introduced a single-frequency laser[7] and repeated the atom-loss spectroscopy scans. However, the loss feature persisted despite the introduction of this single-frequency laser, ruling out the multi-frequency laser as the cause for the unexpected atom loss. Since the single-frequency laser, supplying only 50 W, did not mitigate the additional atom loss, we reverted back to working with the 100 W fibre laser.

[6] IPG Photonics YLR-100-1070-LP
[7] Azurlight ALS-IR-1064-50-I-CC-SF

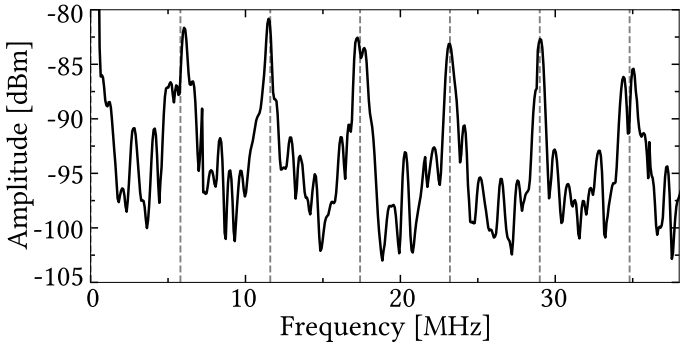

Figure 5.16.: Power spectrum of the multi-frequency IPG fibre laser. Peaks every 5.8 MHz (grey dashed lines) reveal the mode-spacing of the laser.

Ultimately, we traced the cause of the additional atom losses to an unexpected source of interference: extremely faint stray light present in our MOT beams throughout the entire experimental sequence. As this light was not discernible by the naked eye, its presence was revealed during an atom loss scan where we manually blocked the fibre output, leading to a noticeable difference in results. Despite turning off the 3D MOT acousto-optic modulators and closing the shutter in front of the fibre in-coupler after the molasses stage, a small fraction of cooling light (a few μW) from the undiffracted order of the AOM evaded complete blockage by the shutter. Since this light was not tuned close to the atomic resonance, it did not significantly affect the magnetic trap until the bias magnetic field was ramped up in the crossed optical dipole trap, shifting the energy levels into resonance.

Specifically, the light is frequency-stabilized to the ground state crossover, approximately 220.5 MHz detuned from the transition $|F = 1\rangle \rightarrow |F' = 1\rangle$. As shown in the bottom graph of figure 5.14 A, the loss feature is centred around 75 G, when (almost) no dipole light is present. In the presence of a magnetic field, the $S_{1/2}$ ground state and $P_{3/2}$ excited state energy levels are shifted, as illustrated in figure 5.17 A.

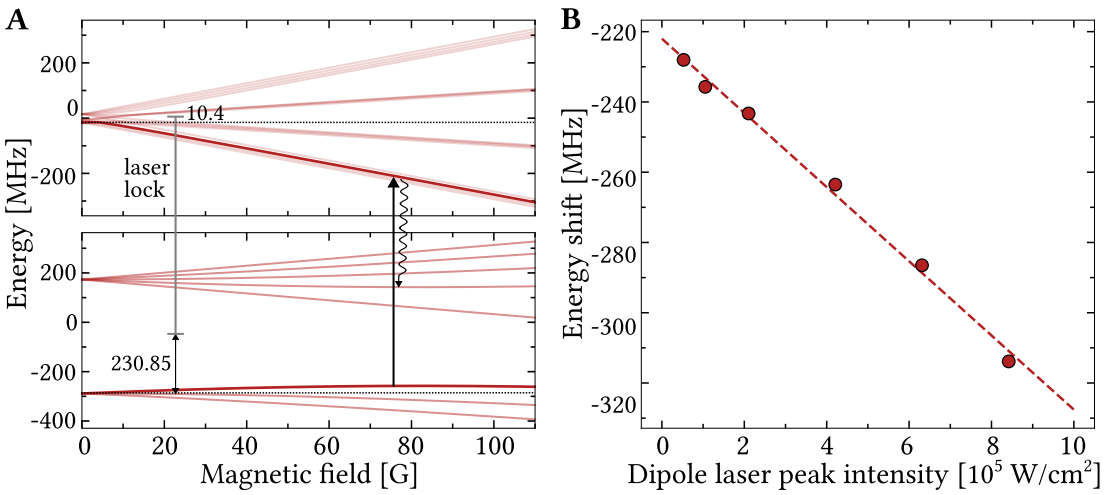

Figure 5.17.: Potassium Breit-Rabi diagram and energy shift as a function of dipole laser power. A: Breit-Rabi diagram for the $S_{1/2}$ ground state and $P_{3/2}$ excited state. The two hyperfine states that are involved in the loss process are marked by dark red lines. The laser locking point is indicated by the grey line, while the driven transition is illustrated by the black arrow. The decay, removing atoms from the cycling transition, is shown as a black wiggly arrow. B: AC-Stark energy shift of the resonance feature as a function of the dipole laser peak intensity (focused beam waist radius $w_0 = 55\,\mu m$). The dashed line indicates a linear fit to the experimental data, characterized by a slope of $-106(4)\,Hz/(W/cm^2)$.

In our specific case, similar to high-field imaging detailed in [131, 140], the stray light is driving the transition $|g_-\rangle \sim |m_J, m_I\rangle \rightarrow |e\rangle$, marked by the black arrow, with:

$$|g_-\rangle = \sqrt{p}\,|-1/2, -1/2\rangle + \sqrt{1-p}\,|1/2, -3/2\rangle \tag{5.6}$$

$$|g_+\rangle = \sqrt{p}\,|1/2, -3/2\rangle + \sqrt{1-p}\,|-1/2, -1/2\rangle \tag{5.7}$$

$$|e\rangle \approx |-3/2, -1/2\rangle \tag{5.8}$$

As both ground states, $|g_-\rangle$ and $|g_+\rangle$, possess an admixture of the $|-1/2, -1/2\rangle$ state, the excited atoms in the $|-3/2, -1/2\rangle$ state can decay back to either ground state. Therefore, the driven transition is not closed at these intermediate magnetic fields, and atoms can decay to states with a higher two-body loss rate.

Using the Breit-Rabi diagram, we can convert the resonance locations recorded for different dipole laser intensities to an energy shift. Figure 5.17 B illustrates the dependence of this energy shift on the peak intensity of the dipole laser (focused beam waist radius $w_0 = 55\,\mu\text{m}$). The linear behaviour is confirmed by a linear fit, indicated by the dashed red line. The energy shift at 0 W, marked by the intercept and with a value of $-222(2)$ MHz, agrees well with our previous assumption that the light, detuned by 220.5 MHz at zero magnetic field, is now shifted into resonance due to the presence of a magnetic field. Furthermore, the observed linear shift of the resonance with respect to the maximum dipole beam intensity in the crossed region, amounting to $-106(4)\,\text{Hz}/(\text{W}/\text{cm}^2)$, can be attributed to the differential AC-Stark shift between the ground and excited states involved in the transition [211].

To permanently address this issue, we incorporated an additional shutter in front of the 3D-MOT fibre coupler to ensure that no light gets through any more.

Atom loss at 130 G

In addition to the observed atom loss induced by stray light, we identified another unexpected loss signal at an approximate magnetic field strength of 130 G, as depicted in figures 5.14 and 5.15 A. A finer scan, illustrating the appearance of this loss feature, is presented in figure 5.18 A, demonstrating its precise location at 131.6(2) G through a Gaussian fit. This fit further highlights a slightly asymmetric shape of the loss feature. Note that while this measurement was conducted in dual-species operation, this feature does not originate due to the interaction with sodium atoms, as it is also present in the previously discussed single-species scans. The loss in the potassium atom number is accompanied by an increase in the sodium atom number, as hetero-nuclear collisional losses are suppressed due to the absence of potassium.

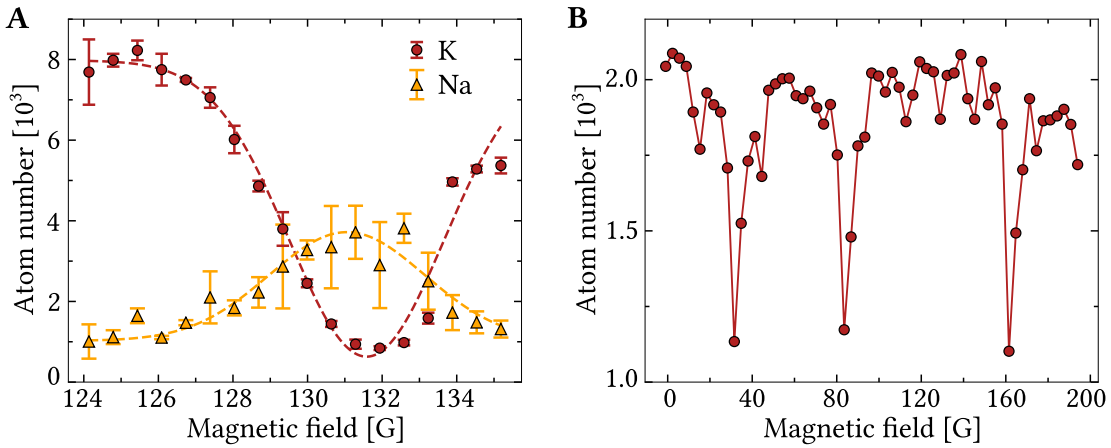

Figure 5.18.: Atom-loss feature of ^{39}K at 131.6(2) G. A: Feshbach spectroscopy for the Na-K mixture in the magnetic field range 124 − 135 G. Dashed lines represent Gaussian fits to the experimental data. B: Potassium Feshbach spectrum at a lower temperature of approximately 1 µK.

Taking a closer look at figure 5.14, we can discern that, similar to the intra-species atom-loss features (indicated by grey dashed lines), the loss signal at 131.6(2) G also weakens with lower dipole powers. As the atomic density decreases, collisional losses diminish, indicating that this new feature arises from collisions between potassium atoms. Further examination of figure 5.15 A and the persistence of the loss feature, even after mitigating the stray light issue, suggests the involvement of ^{39}K atoms specifically in the $|1,-1\rangle$ spin state in these undesired collisions.

Additionally, we recorded a Feshbach spectrum at a lower temperature of approximately 1 µK, as depicted in figure 5.18 B. This dataset was acquired by evaporatively cooling the Na-K mixture in the cODT, followed by removing the sodium atoms from the trap and subsequent holding of cold potassium atoms at a dipole power of 10 W for 200 ms. Both s-wave Feshbach resonances and the stray light loss feature are evident, whereas the additional loss signal close to 130 G cannot be resolved. The width of the resonance likely reduced with decreasing temperature, making it indiscernible in this coarse scan. Hence, further investigations, including a finer magnetic field scan at different temperature settings, are required to confirm this hypothesis.

In summary, our preliminary observations suggest the presence of a high partial-wave ($l \geq 2$) Feshbach resonance for the ^{39}K $|1,-1\rangle$ spin state at approximately 131.6(2) G. However, a comprehensive analysis of the temperature dependence of this loss feature, as conducted in other experiments [212–214], along with rigorous multichannel calculations, are essential to draw definitive conclusions and improve our understanding of the underlying physics.

Having successfully identified and mitigated the stray light issue, and equipped with a quantitative understanding of the potassium Feshbach spectrum, our focus now shifts to investigating hetero-nuclear collisions.

5.4.3. Inter-species ^{23}Na-^{39}K Feshbach resonances

Besides homo-nuclear collisions, the interactions between the different species need to be considered. The ^{23}Na-^{39}K Feshbach spectrum for the incident spin channel $\left(|1,-1\rangle_{\mathrm{Na}} + |1,-1\rangle_{\mathrm{K}}\right)$ is shown in figure 5.19.

On the homo-nuclear side for ^{39}K, there are three s-wave Feshbach resonances: one at 32.6 G, another at 162.8 G - both of which were investigated in the previous subsection - and a high-field resonance at 562.2 G. In contrast, sodium exhibits a constant scattering length of $52\,a_0$. The inter-species Feshbach resonances are reported to be situated at 34.2 G, 248.1 G, and 651.5 G, with a zero-crossing at 117.0 G [71, 215].

In the context of dual-species condensation, achieving miscibility is a key requirement. The degree of miscibility is governed by the parameter δg, as defined in equation 2.3. The inset in figure 5.19 displays the magnetic field dependence of the miscibility parameter for the ^{23}Na-^{39}K mixture in the range of 100 G to 160 G. Successful sympathetic cooling necessitates substantial spatial overlap between the two species, a condition ensured only in the miscible region where $\delta g < 0$. A comprehensive analysis of the different interactions regimes can be found in [71, 100].

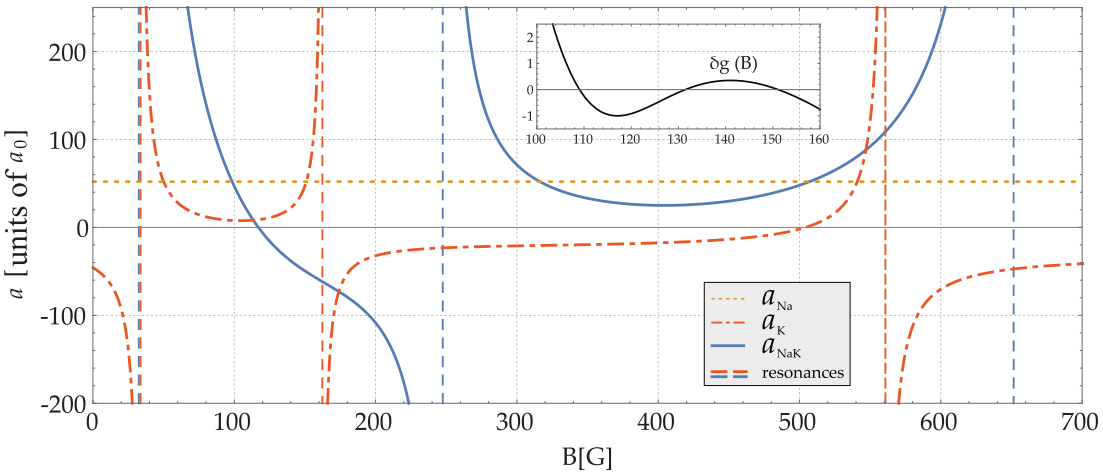

Figure 5.19.: Spectrum of inter- and intra-species Feshbach resonances for a ^{23}Na-^{39}K mixture in spin states $|1,-1\rangle$. The inset shows the dependence of the miscibility parameter δg on the bias magnetic field B. Figure taken from [71].

Similar to the homo-nuclear case, we conducted measurements of the inter-species Feshbach resonances for the ^{23}Na-^{39}K $|1,-1\rangle$ mixture using atom-loss spectroscopy. After the dual-species MOT and subsequent microwave evaporation in the magnetic trap, the two atomic clouds were loaded into the crossed optical dipole trap. Here, we subject the atoms to a magnetic bias field. The potassium cloud, constituting the minority species with $N_{\mathrm{Na}}/N_{\mathrm{K}} \approx 10$, was used to probe the Feshbach spectrum. Close to the resonances, the interaction strength diverges, leading to atom loss from the trap, which is more pronounced for the minority species.

In the cODT, we rapidly ramped the magnetic bias field to the desired value within 5 ms and held the atoms at this constant bias field for 200 ms. Following this holding period, both the magnetic field and the trapping potential were turned off, and the two atom clouds were imaged following a short time-of-flight of 0.1 ms.

A scan of the magnetic field in a range between 230 G and 260 G yielded the data presented in figure 5.20. Employing a Gaussian fit to the experimental data, we determined the resonance location at $B_0 = 247.8(8)$ G, demonstrating good agreement with the experimentally and theoretically extracted values presented in [71], which are $B_{\mathrm{exp}} = 247.1(2)$ G and $B_{\mathrm{theo}} = 248.1$ G.

Due to its close proximity to the low-field potassium Feshbach resonance at 33.5820(14) G [98], we were not able to precisely map out the low-field inter-species resonance.

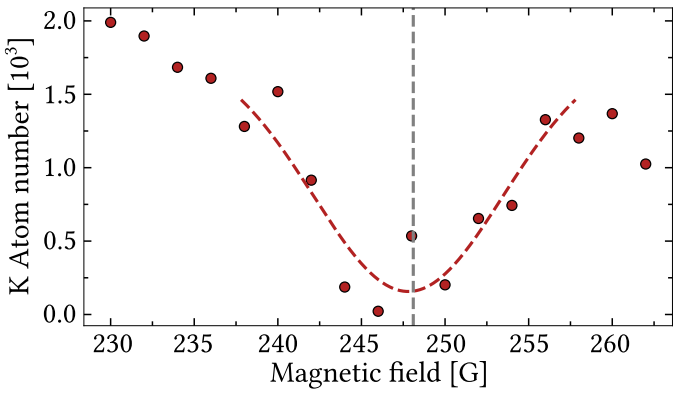

Figure 5.20.: Atom-loss spectroscopy of an inter-species ^{23}Na-^{39}K Feshbach resonance. The resonance position was determined through a Gaussian fit (red dashed line). The experimental data show good agreement with the theoretical prediction [71], depicted as a grey dashed line.

5.5. Towards dual-species condensation

At zero magnetic field, the inter-species interaction is very strong, as evident from figure 5.19, with Schulze et al. [71] reporting an inter-species scattering length of $a_{\mathrm{NaK}}(B = 0) = -416\,a_0$.

To further analyse inter-species interactions at zero magnetic field, we conducted lifetime measurements of the potassium cloud under two conditions: with and without the presence of sodium. The atoms were initially cooled in the MOT and magnetic trap, loaded into the cODT, held for a variable duration t_{hold} at zero magnetic bias field, and the potassium atom number was recorded. In one scenario, both species were loaded, while in the other, a resonant light pulse selectively removed the sodium atoms before loading into the cODT. The temporal evolution of the potassium atom number as a function of t_{hold} for both settings is depicted in figure 5.21.

In the absence of sodium, the lifetime of potassium atoms was measured to be 1.8(2) s. This relatively low lifetime observed without the influence of inter-species losses may be attributed to free evaporation resulting from too high potassium temperatures following the transfer into the cODT. In dual-species operation, the presence of sodium significantly reduced the $1/e$-lifetime in the cODT to 0.41(2) s, a reduction attributed to inter-species three-body losses.

In conclusion, at zero magnetic field, the mixture of sodium and potassium experiences a large amount of undesirable losses. This is especially prevalent in the high-density regime of the crossed optical dipole trap. At these high atomic densities, three-body

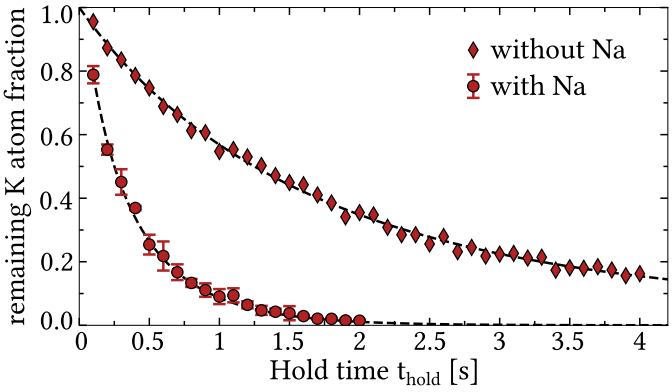

Figure 5.21.: Potassium lifetime in the crossed optical dipole trap at zero magnetic field with and without the presence of sodium. Atom-loss curves were fitted to both data sets (indicated by black dashed lines), resulting in a potassium trap lifetime of 1.8(2) s and 0.41(2) s, in the absence and presence of sodium, respectively.

losses, resulting from the large inter-species scattering length at zero magnetic field, are dominant, preventing dual-species operation at these low fields. However, Feshbach resonances are an efficient tool for tuning the inter- and intra-species scattering lengths into a regime where dual-species condensation becomes feasible.

In particular, for a magnetic bias field around 153 G, all three scattering lengths, a_{Na}, a_K, and a_{NaK}, become comparable in magnitude, rendering the atomic mixture miscible. Consequently, following microwave evaporation in the hybrid trap, we transferred the atoms to a pure dipole trap and ramped the bias field up to 153 G within 10 ms. Following the evaporation ramps, we imaged both atomic clouds using the high-resolution horizontal absorption imaging system. An exemplary measurement is presented in figure 5.22, where a time-of-flight of 0.5 ms was chosen.

In this measurement, both the sodium (labelled as A) and the potassium (labelled as B) cloud are still thermal, as demonstrated by the Gaussian fits to the integrated column

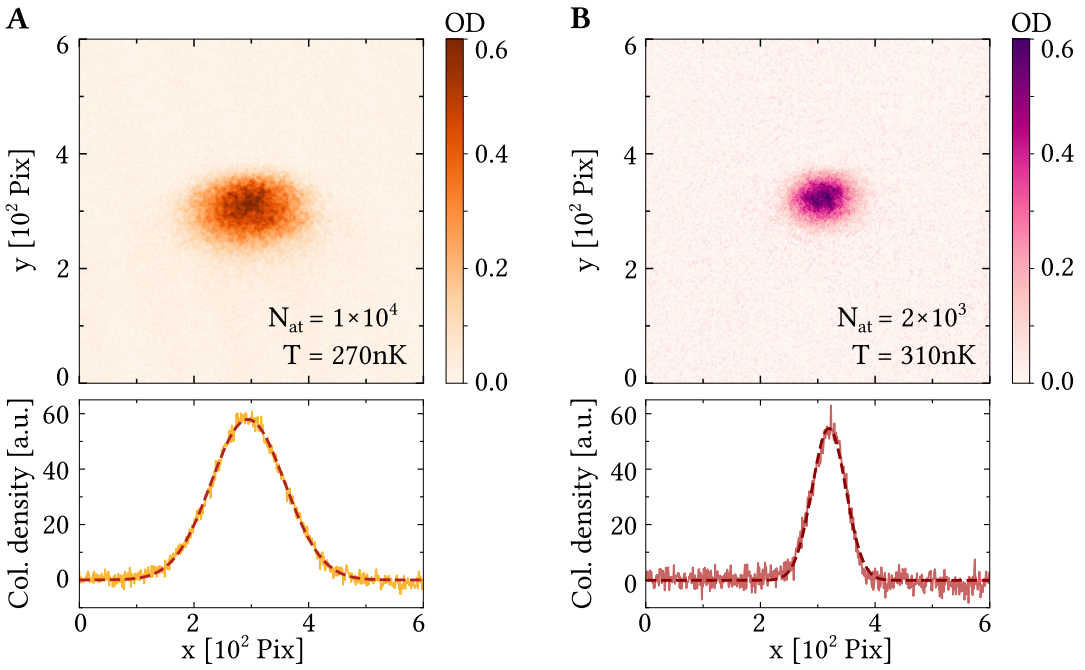

Figure 5.22.: Absorption images of sodium (A) and potassium (B) close to dual-species degeneracy following evaporation at 153 G. The top row shows absorption images of the sodium and potassium cloud, captured simultaneously on two dedicated cameras, with a time-of-flight of 0.5 ms. The accompanying graphs below showcase the column densities integrated along the y-axis, with the dashed lines indicating Gaussian fits applied to the respective datasets.

densities (dashed lines). Following the final evaporative cooling stage, we are left with approximately 1×10^4 sodium atoms at a temperature of around 270 nK and roughly 2×10^3 potassium atoms at approximately 310 nK. As the temperature of the potassium cloud has approached the sodium temperature quite well, we can infer a significant degree of overlap and successful sympathetic cooling. The existence of a sufficiently high elastic inter-species collision rate ensures thermalization between sodium and potassium atoms. Nevertheless, despite the achieved temperature reduction through the current evaporative cooling process at 153 G, dual-species condensation has not been reached.

In an effort to condense both sodium and potassium, we made the following observations:

1. Light-assisted collisions resulted in minor disruptions to the dual-species MOT loading process. In a population-imbalanced configuration, the sodium loading dynamics remained largely unaffected, while potassium, as the minority species, experienced a 25% reduction in atom number.

2. In the dipole trap, prior to evaporation, the temperature of the sodium atoms measured approximately 20 µK, while the potassium cloud's temperature was around 50 µK. During single-species operation, we were able to achieve a lower temperature of 8 µK for sodium.

3. The overlap between the magnetic trap and dipole trap is not ideal, potentially heating up the atoms during the transfer process.

4. For the imaging process, we have to ramp the magnetic field to zero, such that the imaging light remains resonant. However, this approach is sub-optimal, because of unfavourable scattering properties at 0 G. Furthermore, ramping across inter- and intra-species Feshbach resonances during this process introduces additional losses.

5. We observed an anti-correlation in the atom numbers of sodium and potassium within the dipole trap. Extended MOT loading times for potassium resulted in decreased sodium atom numbers, and conversely. By reducing the potassium MOT loading time to 0.1 s, we successfully generated a sodium BEC. However, this came at the expense of almost completely depleting the potassium population.

6. Changing the dipole trap power in the hybrid trap had contrasting effects on sodium and potassium atom numbers. Increasing the dipole power improved the final sodium atom number but decreased the potassium atom number, while reducing the dipole power had the opposite effect.

Based on the first observation, we can conclude that the dual-species MOT of ^{23}Na-^{39}K suffers from light-assisted collisions, impeding a substantial increase in the potassium atom number. While alternative approaches were discussed in section 5.1, the current strategy entails maintaining the dual-species MOT configuration and accepting the associated collisional losses.
With regard to points two and three, a more detailed analysis of the temperatures of the atomic clouds both before and after the transfer between various traps is warranted. To enhance the transfer of atoms from the magnetic trap to the crossed optical dipole trap, we either have to adjust the alignment of the dipole beams for improved overlap with the magnetic trap or gradually adjust the offset magnetic fields during the magnetic trap phase.
The issue raised in point four concerning the imaging process could be resolved by adopting a high-field imaging system. Implementing an offset lock to freely adjust the frequency of the imaging light would enable us to directly image the atoms at the Feshbach field.
The observations highlighted in points five and six, concerning the anti-correlation in the sodium-potassium atom numbers, can be attributed to three-body losses arising from hetero-nuclear collisions. These losses are likely enhanced by the high atomic densities within the hybrid trap during the 3 s-long microwave (MW) evaporation stage.

The current experimental sequence relies on MW evaporation as a crucial step to attain a single-species sodium BEC. Consequently, shortening or removing the MW evaporation altogether should only be attempted in conjunction with an adapted cooling sequence for sodium. Following a strategy similar to that employed for potassium, we propose implementing a sodium D1 grey molasses, as detailed in [196], to significantly enhance the phase-space density. Following this sub-Doppler cooling process, a brief magnetic trapping phase would serve as a spin-cleaning stage, and facilitate an efficient transfer into the all-optical dipole trap. Within this trap, the bias magnetic field becomes an independent parameter and can be adjusted to achieve a miscible mixture of the two species. Subsequent forced evaporative cooling ramps would ideally result in dual-species degeneracy, with sodium acting as a sympathetic coolant for the

potassium atoms.
By adopting this modified experimental cooling sequence, our objective is to avoid the application of strong magnetic field gradients necessary for an efficient microwave evaporation stage. Consequently, the regime of high atomic densities would not be accessed until the inter-species scattering length becomes a tunable parameter.

Conclusion

Loading two distinct atomic species into a shared trap and successfully cooling them down to dual-species degeneracy poses notable challenges. In the dual-species MOT, light-assisted collisions resulted in considerable atom loss for potassium, while the large sodium MOT stayed largely unaffected.
A particular difficulty arises for the ^{23}Na-^{39}K mixture, due to the inter-species scattering characteristics at zero magnetic field. A notably high three-body loss rate significantly reduces the trap lifetime within the high-density regime. Consequently, once the atoms are loaded into the crossed optical dipole trap, a Feshbach field at around 153 G is turned on to access a regime of diminished losses.
While we were able to conduct thorough investigations into homo- and hetero-nuclear Feshbach resonances, achieving dual-species degeneracy has remained elusive. We attribute this challenge to atom losses resulting from three-body collisions within the hybrid trap, yielding insufficient atom numbers for the final evaporation process. We proposed to overcome these limitations by removing the microwave evaporation stage in the hybrid trap and implementing a grey molasses scheme for sodium to enhance the phase-space density prior to loading into the magnetic trap.

CHAPTER 6

Concluding remarks

In this thesis, I introduced the setup of a new ultracold ^{23}Na-^{39}K mixture experiment aimed at studying domain formation within an immiscible atomic mixture. This chapter summarizes the discussed aspects of the experiment and offers an outlook for future experimental developments, highlighting the next steps towards the investigation of demixing dynamics.

6.1. Summary

The initial chapters provided a comprehensive overview of the critical tools and techniques employed in the process of cooling and trapping two distinct atomic species. Specifically, the optical layout of the newly established laser systems was discussed, outlining the production of the necessary laser frequencies for cooling, transportation, and imaging of cold sodium and potassium atoms.

Spatial confinement was accomplished via the application of magnetic field gradients, facilitated by a pair of magnetic field coils. We closely examined aspects concerning design, fabrication, and integration of these new coils, wound from hollow-core copper wire. An H-bridge was employed to control current flow through the coils, allowing the creation of either bias fields calibrated at 1.97(1) G/A or magnetic field gradients that scale approximately with 1.02 G/cm/A. During the magnetic trapping phase, the coil can be set to produce large magnetic field gradients. Conversely, once the atoms are loaded into the optical dipole trap, the electric current direction can be reversed to generate a magnetic bias field, enabling the use of inter- and intra-species Feshbach resonances to tune the interactions.

To image the atoms following the cooling sequence and subsequent experiments, an intricate absorption imaging scheme was implemented for each atomic species. This scheme incorporated a high field-of-view setup with a magnification of $M_{\text{coarse}} = 0.445(2)$, essential for characterizing and optimizing early cooling stages such as the magneto-optical trap (MOT) or the optical molasses. Additionally, a high-resolution imaging system, featuring an enhanced magnification of $M_{\text{fine}} = 20.36(3)$, was employed to image the Bose-Einstein Condensate (BEC). Both configurations facilitate

simultaneous absorption imaging of sodium and potassium atomic clouds in the horizontal plane, with dedicated cameras for each species.

The subsequent chapters of this thesis focused on the application of the previously introduced experimental tools, starting with an in-depth examination of the sodium cooling sequence culminating in the achievement of Bose-Einstein condensation. Attaining a BEC with these dilute atomic clouds necessitates cooling the atoms to extremely low temperatures. As laser cooling efforts are limited by the recoil limit, the atoms were transferred from the MOT into a conservative magnetic trap potential, where microwave evaporation enhanced the phase-space density. Following this stage, the atoms were loaded into a crossed optical dipole trap (cODT), where the critical temperature was crossed during a final forced evaporative cooling phase, resulting in a sodium BEC comprising approximately 7×10^4 atoms.

The second part introduced the second atomic species, namely potassium 39. While each species poses distinct challenges when trying to achieve ultracold temperatures, the combination of two atomic species involves additional complexities related to inter-species interactions and collisional losses. During the MOT stage, light-assisted collisions caused atom loss that proved to be particularly detrimental for the minority species, potassium. Given that sodium, as the majority species, was largely unaffected, we decided to maintain this simple dual-species loading approach and accept the atom loss for potassium.

To reduce the temperature and increase the phase-space density of the potassium cloud after the MOT stage, we implemented a D1 grey molasses scheme, achieving temperatures in the order of 8 μK. Following this sub-Doppler cooling stage, the atoms were transferred to the magnetic trap, where sodium was selectively cooled using microwave evaporation. Through collisional thermalization, the potassium cloud was sympathetically cooled. Upon transfer to a crossed optical dipole trap, where high atomic densities prevail, inter-species interactions significantly influenced the system. Severe three-body losses were observed at zero magnetic field, prompting the ramping of the bias field to a constant value of 153 G. At this field strength, the intra- and inter-species scattering lengths are of similar magnitude, rendering the mixture miscible and theoretically enabling dual-species condensation. However, the current atom numbers for both sodium and potassium prior to evaporation fall short of achieving the required critical phase-space densities following the intensity ramps. As a result, dual-species degeneracy has remained elusive so far.

We attribute these issues to the presence of excessively high atomic densities in the hybrid trap, resulting in increased hetero-nuclear collisional losses. Consequently, the different parameters of the current experimental sequence should be inspected more closely and optimized in a dual-species setting.

6.2. Outlook

The logical next step in the experiment involves refining the cooling sequence to achieve dual-species Bose-Einstein condensation with our ^{23}Na-^{39}K mixture. In response to the observed anti-correlation in sodium-potassium atom numbers, we are planning to eliminate the microwave evaporation stage in the hybrid trap and reduce the duration of the magnetic trapping stage. The goal is to load the atomic mixture as fast as possible into the crossed optical dipole trap, where we can freely tune the interaction using the magnetic bias field. Additionally, to further enhance the phase-space density of sodium before loading the mixture into a magnetic trap, we are considering implementing a D1 grey molasses scheme for sodium in conjunction with the already implemented potassium grey molasses approach.

Following the eventual achievement of dual-species condensation, we plan to confine the ultra-cold mixture in a two-dimensional optical trap. Our objective is to realize tight confinement along the vertical gravity direction, attaining a trapping frequency in the order of 1 kHz, while maintaining weak confinement in the horizontal plane. This specific trapping configuration will be realized utilizing a red-detuned light sheet [216, 217]. By employing a cylindrical lens, the light eminating from a 1064 nm single-frequency laser will be tightly focused along the z-direction while maintaining collimation along the perpendicular axis. This approach is anticipated to result in horizontal trapping frequencies in the order of 30 Hz[1].

Additionally, as the two-dimensional atomic cloud will be distributed in the horizontal plane, we require a vertical imaging scheme. At the core of this imaging system will be a high-resolution imaging objective[2], possessing a numerical aperture of NA = 0.5 and featuring a chromatic focal correction tailored for both sodium and potassium light. To leverage the vertical axis both for the imaging beam and the MOT beam, we intend

[1] It is worth noting that the trapping frequencies for sodium and potassium atoms differ slightly due to their distinct masses and polarizability characteristics.

[2] custom-fabricated by Special Optics.

to exploit the temporal separation of the MOT stage and the imaging phase. During MOT loading, a mirror mounted to a pneumatic stage will guide the vertical MOT beam onto the atoms. The focusing of the MOT light due to the objective will be compensated with an additional lens, forming a telescope in conjunction with the objective lens. Subsequent to the MOT loading phase, this mirror will be translated out of the imaging path, allowing the absorption beam to pass through and be focused onto the camera.
Similar to the horizontal imaging, the imaging process in the vertical plane will feature a dichroic mirror to separate the sodium and potassium light. A secondary lens will then project the atomic signal onto a dedicated camera for each species. This arrangement will yield a roughly 33-times magnified absorption image of the two-dimensional atomic cloud, providing the necessary details for a comprehensive analysis and characterization. Further information regarding this additional imaging scheme, as well as a thorough description and characterization of the two-dimensional optical trap can be found in [126].

Once the two atomic species are condensed, loaded into the two-dimensional trap, and can be imaged from above via the vertical imaging system, we can start addressing some fundamental physics questions. Specifically, by quenching the inter-species interaction strength from a miscible to an immiscible state, we aim to observe and study the formation of domains resulting from demixing dynamics. In addition to varying the interaction strength, we can also investigate the influence of population imbalances on the size and growth of the emergent domains in an immiscible mixture. Consequently, our experimental machine, including the future updates, will serve as a highly tunable platform for exploring demixing dynamics. Furthermore, its versatility extends to facilitating quantum simulation applications, particularly in the investigation of Bose polarons, offering a rich spectrum of research opportunities in the field of quantum many-body physics.

APPENDIX A

Magnetic field coils supplementary

A.1. H-bridge driver circuit

The H-bridge is used to reverse the current direction through one of the coils. The corresponding driver circuit is depicted in figure A.1. Additionally, an image of the assembled circuit is shown in figure A.3 B.

Depending on the state of the two inputs - SWITCH and DISABLE - the logic circuit sets the state of the four drive outputs according to the truth table 3.4. The input stage features an opto-isolator ensuring the decoupling of the ground (with respect to the ground of the experimental control system), while four totem pole outputs connect to the four MOSFET banks of the H-bridge.

The switching coil is connected across the middle banks of this H-bridge, such that the coil operates in an anti-Helmholtz configuration if both signals 1 and 3 are active, while the others have to be inactive. For Helmholtz configuration, the reverse scenario

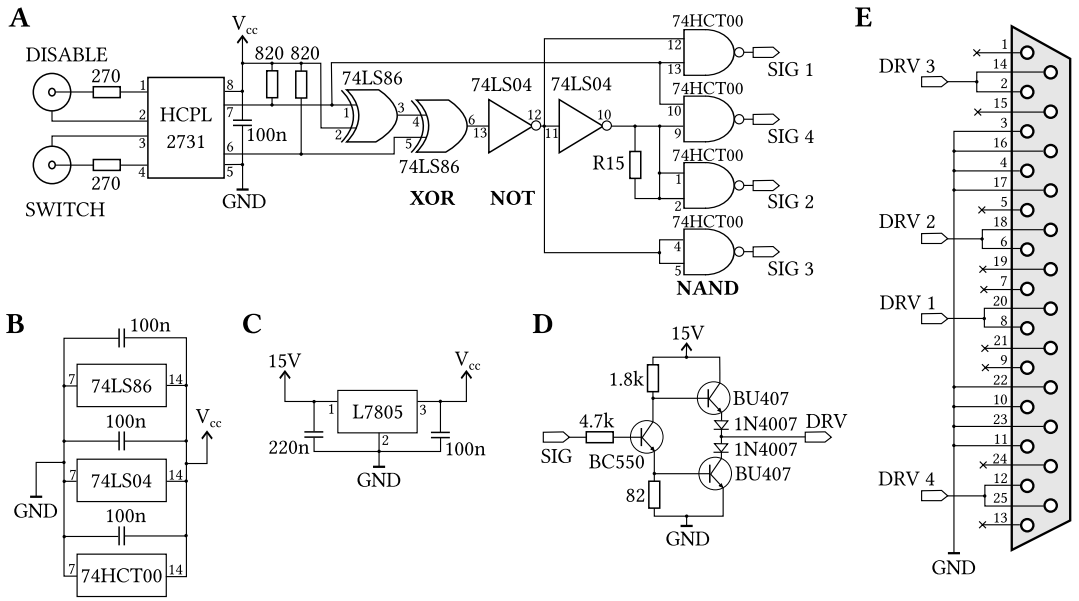

Figure A.1.: H-bridge driver circuit. A: Input stage with logic components. B and C: Supply voltage circuits. D: For each signal line, the output stage features a totem pole driver. E: 25-pin sub-D connector for the drive outputs.

is required. More details on this driver circuit can be found in [131].

A.2. Passbank driver circuit

The passbank regulates the current running through the coils using a current transducer (LEM-sensor[1]) as feedback. This feedback loop is implemented with a driver circuit, as illustrated in figures A.2 and A.3 A.

The passbank driver takes the signal from the LEM-sensor and compares it with an external setpoint. The difference between these two signals is minimized using a subsequent PI-controller, which drives the transistors of the passbank, thereby regulating the electric current running through the connected coils.

To set the range and linearity of the drive voltage with respect to the external set

[1]LEM IT 400-S Ultrastab

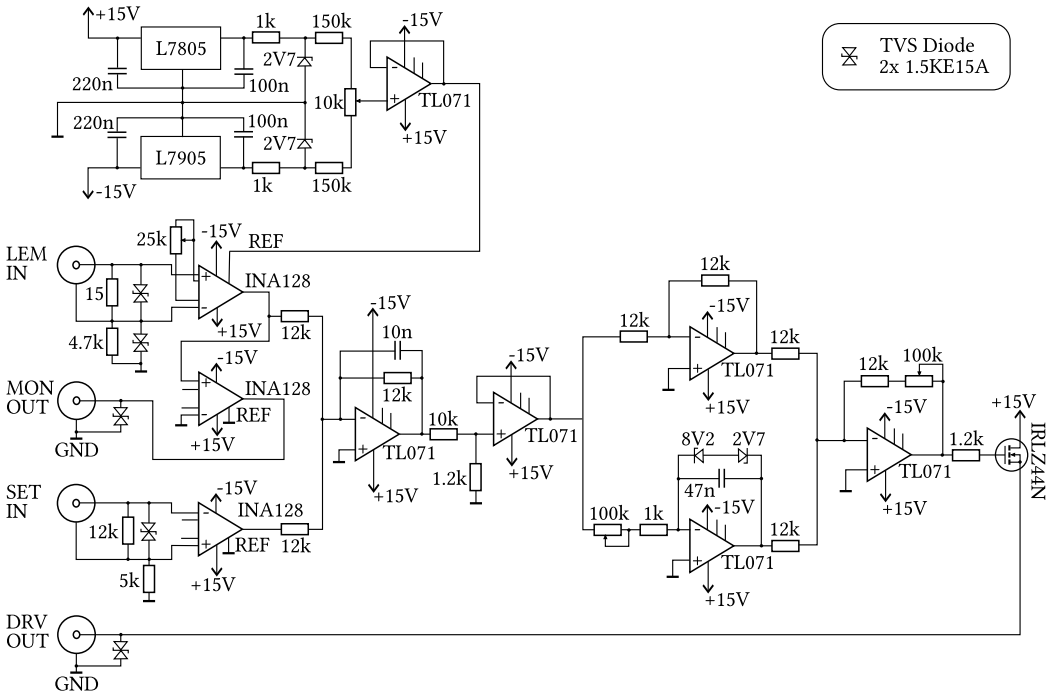

Figure A.2.: Passbank driver circuit. The current signal from the LEM sensor (LEM IN) is converted to a voltage and amplified with an instrumentation amplifier. This voltage signal is coupled out for external monitoring (MON OUT). The LEM-signal is subtracted from the external setpoint (SET IN) and this error signal is fed into a PI-controller, that controls (through DRV OUT) the passbank transistors. The integral component and the total gain can be adjusted through two potentiometers.

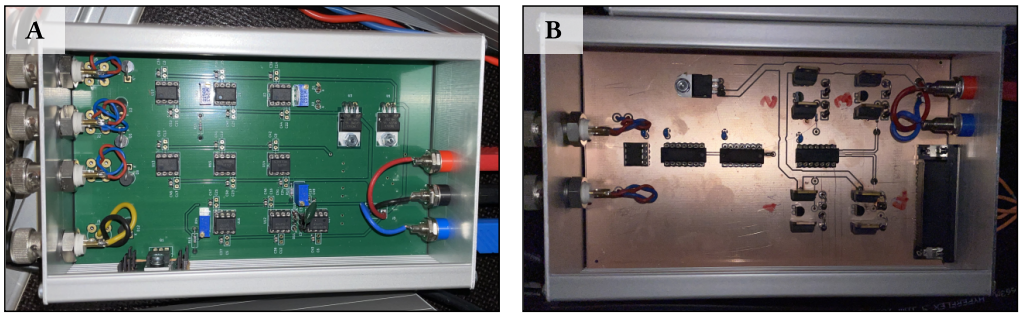

Figure A.3.: Images of the Passbank (A) and H-bridge (B) driver circuits.

voltage from the computer control, several resistors, attached in parallel, are connected to the drive output. For both passbanks, we chose sixteen 390 Ω resistors, resulting in a total resistance of 24.4 Ω in parallel operation.
Additional details concerning the passbank, including technical drawings, can be found in [133], while [131] offers further information on the design of the passbank driver.

A.3. Interlock circuit

When an electric current flows through the magnetic field coil, the resultant dissipated power causes heating in the coil. The main coils, carrying up to 300 A of current, require an efficient water cooling system. Conversely, the offset coils, responsible for generating a few Gauss of a homogeneous field, do not require active cooling.
However, both coil configurations are equipped with a dedicated interlock circuit designed to deactivate the current supply if the coil temperature surpasses predefined limits. NTC thermistors, attached to the coils (one per coil stack for the main coils), function as temperature sensors.

For each NTC input (ten in total), a limit comparator checks if the measured temperature falls within the lower and upper limits. For the given resistor values, the limits are set at approximately 5.5 V and 6.5 V, respectively. However, for the main coil, we increased the upper boundary to 8 V by replacing the lower 3.3 kΩ resistors that connect to ground with 5.6 kΩ resistors. The thermistor voltage calibration can be fine-tuned using a potentiometer.
Depending on whether the temperature reading is within the specified limits, the subsequent output stage, featuring a MOSFET and a self-hold relay, either connects the outputs interlock A and B or C and B. In the initial state, where the temperature has not exceeded the limits, the LED will continuously flash, and the interlock A-B is con-

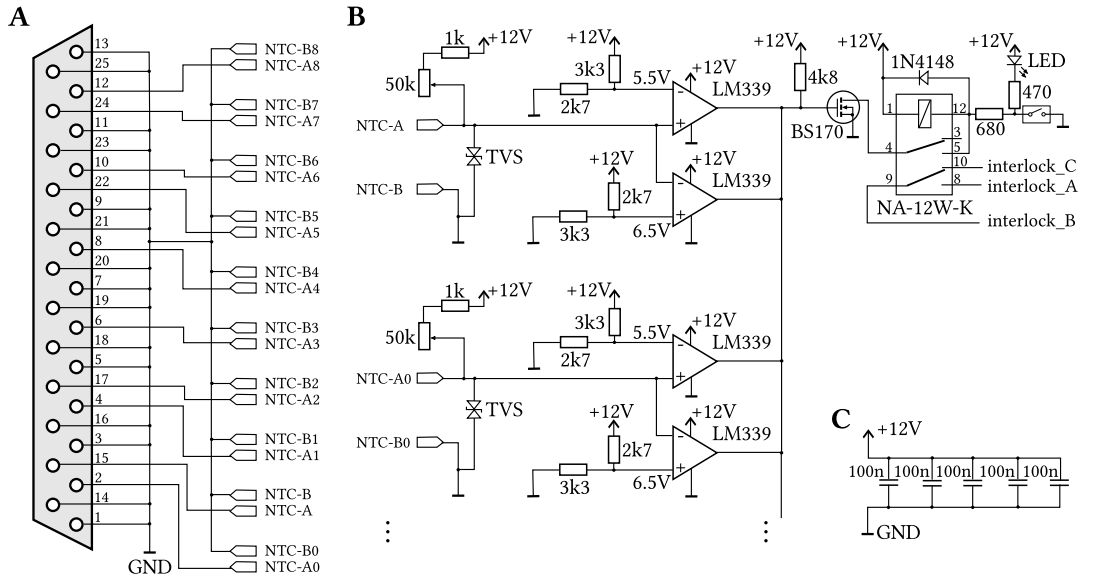

Figure A.4.: Circuit diagram of the coil-interlock. A: 25-pin sub-D connector for the NTC-inputs. B: Output stage featuring a limit comparator for each NTC. A self-hold relay connects the outputs interlock A-B or B-C, depending on the whether the measured temperatures are within the set limits. C: Power supply circuit.

nected. If the temperature surpasses the limits, the interlock activates by opening the connection A-B and connecting A-C. The LED is subsequently turned off. The interlock can be reset, once the temperature has settled again, by pressing the push button below the LED.

A.4. Technical drawings

Main coil stacks

The magnetic field coils were externally manufactured[2], according to the technical drawing depicted in figure A.5. This technical drawing outlines the dimensions of one of the six coil stacks for the main coils, used to generate both strong magnetic field gradients up to 300 G/cm and bias magnetic fields reaching 600 G. To produce these field strengths, three of these stacks are interconnected to form the lower coil, and another three for the upper coil. The provided dimensions already account for the extra space required for the casting epoxy and glass fibre reinforcements.
For each coil stack, the two connection wires are positioned next to each other, exiting

[2]Krämer Energietechnik GmbH

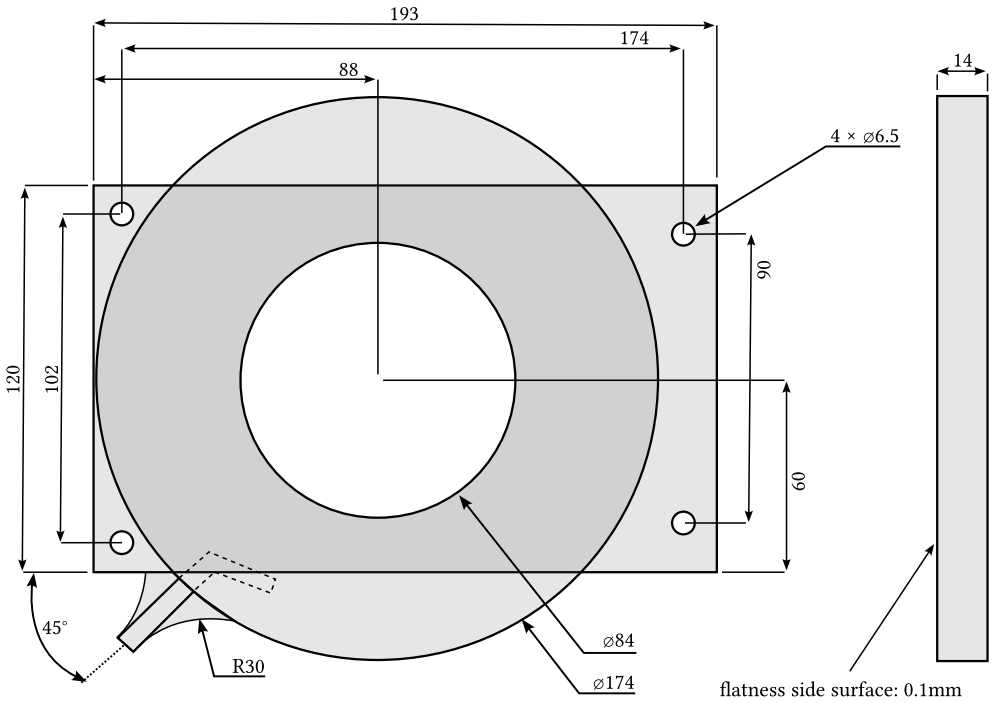

Figure A.5.: Technical drawing of a coil stack with 8 × 2 windings of hollow-core Kapton-insulated copper wire, cast in epoxy. The four through-holes are used for mounting. In the final magnetic field coil design, we utilize three of these stacks for the bottom coil, and another three for the top one. The two connection wires extend another 400 mm, such that we are able to place the connectors for water and current supply at an appropriate distance.

the coil at a 45° angle, as shown in figure A.5. The wires extend another 40 cm, such that the connections for water and current can be implemented without disturbing any optical access to the chamber.

Furthermore, the coils feature four mounting holes that are used to fix the coil stacks together and mount them to brass posts that support the entire structure. The positioning of these holes has been carefully chosen to minimize any obstruction of optical access by the connecting posts between the top and bottom coil.

Water distributor

Each coil stack is equipped with one inlet and one outlet for the cooling water, such that there are twelve water connections in total. To parallelize the cooling for the six coil stacks, a brass water distributor was fabricated. The technical drawing is shown in figure A.6.

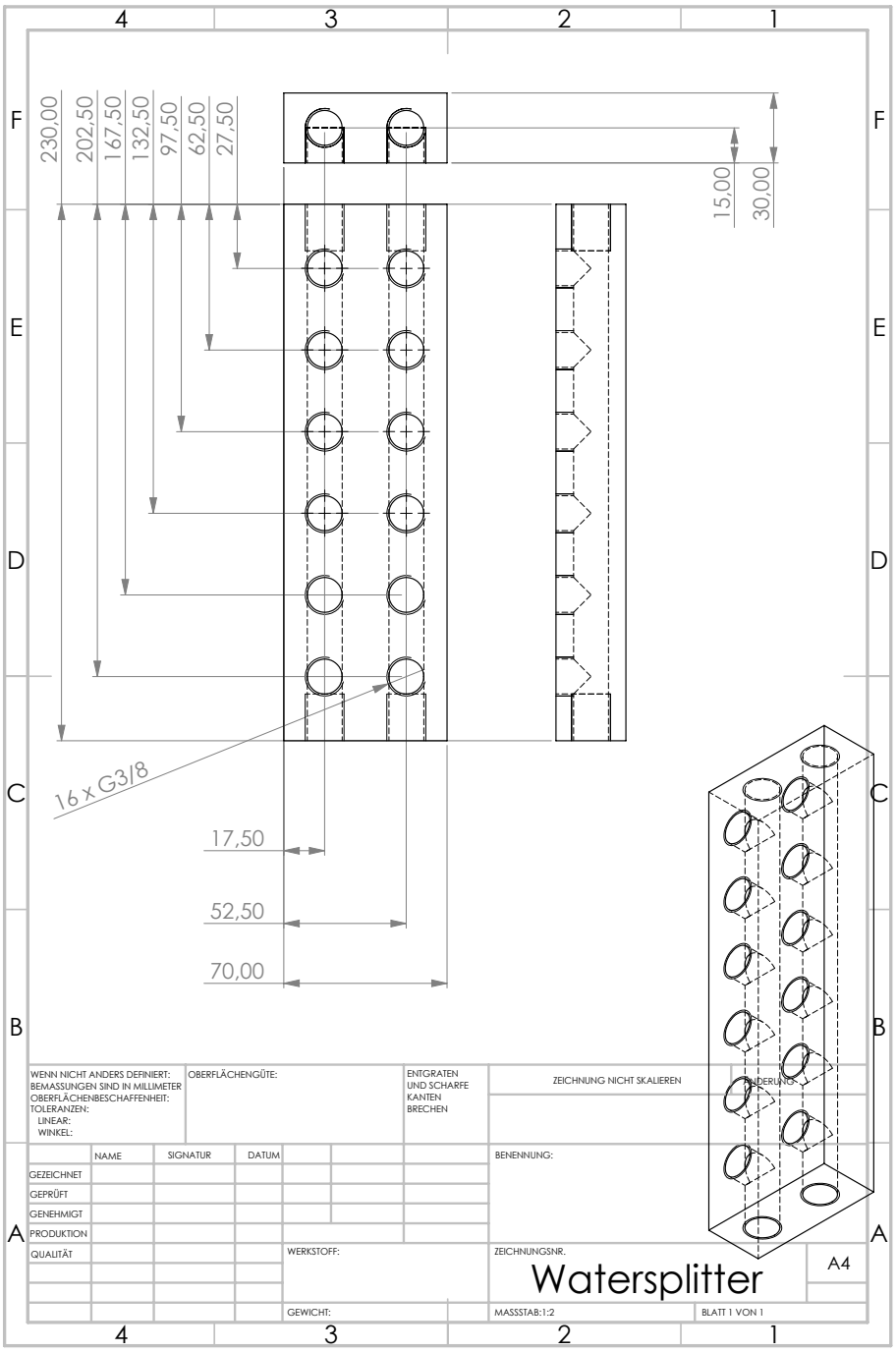

Figure A.6.: Technical drawing of the water distributor for the main coils. The water distributor, made of brass, divides the in- and outlet into six threaded connections each.

A.5. Coil assembly details

The assembly process of the main coils, depicted in the image sequence in figure A.7, comprises the following steps:

1. **Mounting the Bottom Three Coil Stacks:** The bottom three coil stacks are affixed onto four brass posts, which serve as the foundational support for the entire coil structure.

2. **Attaching Support Posts for Top Coil Stacks:** Four comparatively thinner brass posts are connected to the bottom coil to provide support for the upper coil stacks. A top-down perspective is shown in view A.

3. **Fixing the Top Coil Stacks:** The three top coil stacks are secured onto the

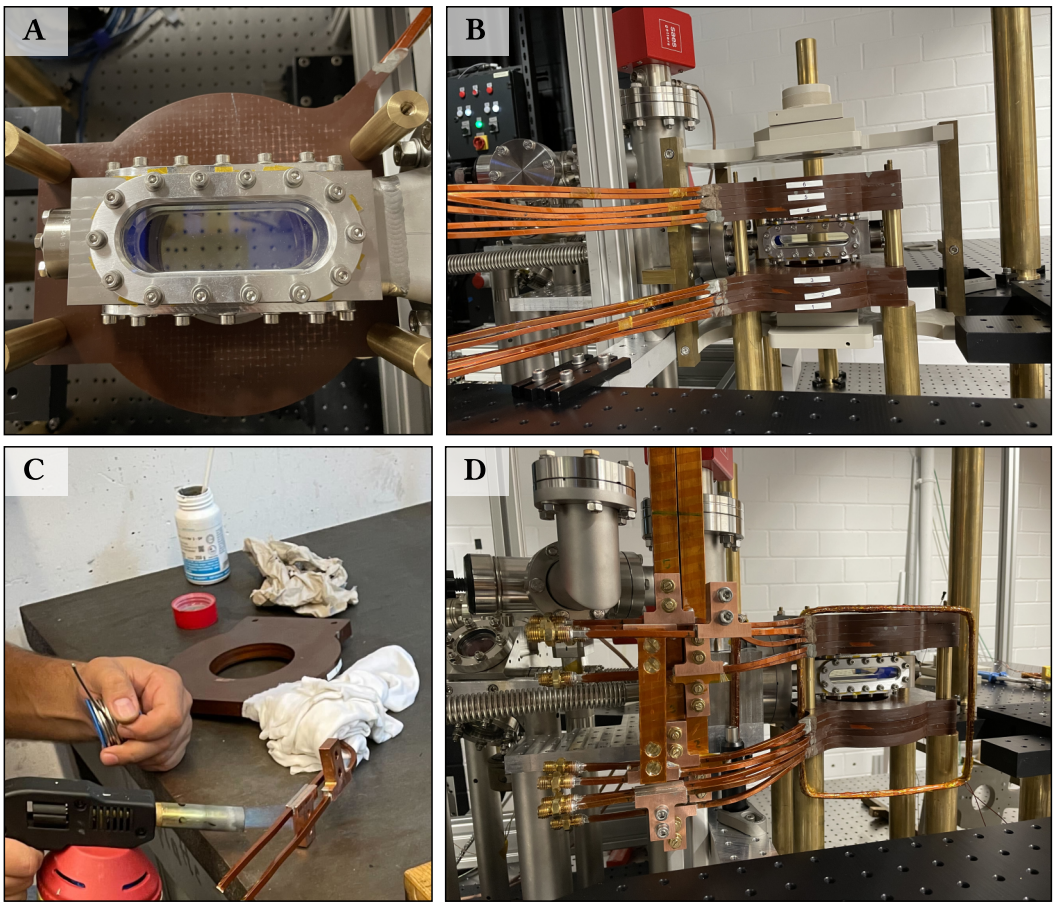

Figure A.7.: Images of the coil assembly process. A: Top view of science chamber with the bottom coil beneath. B: Side view of the main coils with 400 mm long, straight connection wires. C: Soldering copper T-pieces to connection wire. D: Finalized coil assembly.

connecting thin brass posts, as indicated in image B.

4. **Preparing Connection Wires:** The 400 mm long, straight connection wires are bent to their final positions, depending on the connection points to the copper bars. These connection points for attaching the current connectors are marked. The wires are then cut to the required lengths.

5. **Soldering the Current Connectors:** The coil configuration is disassembled for the soldering process. Copper T-pieces, featuring ridges accommodating the coil wire and two M6 through holes for mounting, are employed. At the marked positions along the wire, the Kapton insulation tape is removed, and the joints are cleansed with emery paper. The coil wire is placed into the T-piece ridge; solder flux is applied to the joints, and a blowtorch is used to heat up the copper pieces until the flux achieves a metallic state and starts flowing (see image C). Precautions are taken using a wet towel wrapped around the coil body to prevent damage resulting from high soldering temperatures.

6. **Soldering the Water Connectors:** The water connectors are soldered to the wire ends, following a similar procedure outlined in the previous step. Special care must be taken to avoid blocking the 3 mm wide hole in the hollow-core copper wire.

7. **Final Assembly of the Coil Configuration:** The final assembly involves repeating steps 1-3 and fixing the coil wires via the T-pieces either to each other or to the copper bars responsible for carrying current to the control circuitry. Image D shows the final coil configuration.

APPENDIX B

Bimodal density distribution

For partially-condensed samples, the condensed part and the thermal component contribute to the density distribution via different functional forms. This leads to a bimodal density distribution [218, 219]:

$$n_{\text{bimodal}} = n_{\text{th}} + n_{\text{BEC}} \tag{B.1}$$

In the experiment, we probe the integrated column densities, as we integrate the signal along the line-of-sight, which we define as the y-axis.

Condensed part

We can describe the condensed part as a BEC in the Thomas-Fermi limit, resulting (for a harmonic trap) in a parabolic density profile

$$n_{\text{BEC,2D}}(x,z) = \frac{5}{2\pi}\frac{N_0}{R_x R_z}\left(1-\frac{x^2}{R_x^2}-\frac{z^2}{R_z^2}\right)^{3/2}\Theta\left(1-\frac{x^2}{R_x^2}-\frac{z^2}{R_z^2}\right) \tag{B.2}$$

with the Heaviside function Θ and the Thomas-Fermi radii R_x and R_z. When integrating the two-dimensional column density distribution along one direction one obtains:

$$n_{\text{BEC,1D}}(x) = \frac{15}{16}\frac{N_0}{R_x}\left(1-\frac{x^2}{R_x^2}\right)^2\Theta\left(1-\frac{x^2}{R_x^2}\right) \tag{B.3}$$

Thermal part

A thermal gas well above the transition temperature can be described by a classical Boltzmann distribution. The density profile is then expressed as a Gaussian distribution:

$$n_{\text{th,2D}}^{\text{Boltz}}(x,z) = \frac{N_{\text{th}}}{2\pi\sigma_x\sigma_z}\exp\left\{-\frac{x^2}{2\sigma_x^2}-\frac{z^2}{2\sigma_z^2}\right\} \tag{B.4}$$

and integrating along the z-axis:

$$n_{\text{th,1D}}^{\text{Boltz}}(x) = \frac{N_{\text{th}}}{\sqrt{2\pi}\sigma_x}\exp\left\{-\frac{x^2}{2\sigma_x^2}\right\} \tag{B.5}$$

Below the critical transition temperature, the Bose distribution becomes more important, such that the density follows a Bose-enhanced Gaussian distribution:

$$n_{\mathrm{th,2D}}(x,z) = \frac{N_{\mathrm{th}}}{2\pi\sigma_x\sigma_z g_3(1)}\, g_2\left(\exp\left\{-\frac{x^2}{2\sigma_x^2} - \frac{z^2}{2\sigma_z^2}\right\}\right) \tag{B.6}$$

After integration along z, the line density is given by

$$n_{\mathrm{th,1D}}(x) = \frac{N_{\mathrm{th}}}{\sqrt{2\pi}\sigma_x g_3(1)}\, g_{5/2}\left(\exp\left\{-\frac{x^2}{2\sigma_x^2}\right\}\right) \tag{B.7}$$

with $g_m(t) = \sum_{n=1}^{\infty} t^n/n^m$.

Fitting procedure

Fitting the bimodal density distribution directly to the experimental data is unlikely to perform well, as interactions distort the density distribution in the region where the two components overlap. Consequently, a stepwise fitting procedure, inspired by [218, 220], is carried out. This fitting routine entails:

1. Extracting parameters such as amplitude, centre position, and width from the data. These values serve as initial guesses for the subsequent fit.

2. Determining the region occupied by the condensate by fitting the sum of a Gaussian distribution (equation B.5) and a condensate component (equation B.3) with some offset. This fit gives an estimate for the Thomas-Fermi radius R_{TF}.

3. Subtracting the BEC contribution from the image in a certain region around the maximum, which is dependent on the Thomas-Fermi radius.

4. Fitting the remaining thermal fraction with a Bose-enhanced Gaussian distribution (equation B.7), where we restrict the series expansion to the first three terms. In figure 4.10, the thermal fit is indicated by the dashed line.

5. Removing the thermal contribution and the background, and fitting a parabolic density distribution (equation B.3) to the remaining data. This step yields the condensate atom number and the size of the BEC determined by the Thomas-Fermi radius. This fit is shown in figure 4.10 as a dash-dotted line.

List of Figures

List of Tables

Bibliography

[1] M. H. Anderson, J. R. Ensher, M. R. Matthews, C. E. Wieman, and E. A. Cornell, "Observation of Bose-Einstein condensation in a dilute atomic vapor," *Science*, vol. 269, no. 5221, pp. 198–201, 1995. (cited on pages 1 and 81)

[2] K. B. Davis, M. O. Mewes, M. R. Andrews, N. J. van Druten, D. S. Durfee, D. M. Kurn, and W. Ketterle, "Bose-Einstein condensation in a gas of sodium atoms," *Phys. Rev. Lett.*, vol. 75, pp. 3969–3973, Nov 1995. (cited on pages 1, 3, 72, and 81)

[3] M. R. Andrews, C. G. Townsend, H.-J. Miesner, D. S. Durfee, D. M. Kurn, and W. Ketterle, "Observation of interference between two Bose condensates," *Science*, vol. 275, no. 5300, pp. 637–641, 1997. (cited on page 1)

[4] K. W. Madison, F. Chevy, W. Wohlleben, and J. Dalibard, "Vortex formation in a stirred Bose-Einstein condensate," *Phys. Rev. Lett.*, vol. 84, pp. 806–809, Jan 2000. (cited on page 1)

[5] S. Inouye, M. R. Andrews, J. Stenger, H.-J. Miesner, D. M. Stamper-Kurn, and W. Ketterle, "Observation of Feshbach resonances in a Bose-Einstein condensate," *Nature*, vol. 392, no. 6672, pp. 151–154, 1998. (cited on pages 1 and 9)

[6] S. L. Cornish, N. R. Claussen, J. L. Roberts, E. A. Cornell, and C. E. Wieman, "Stable ^{85}Rb Bose-Einstein condensates with widely tunable interactions," *Phys. Rev. Lett.*, vol. 85, pp. 1795–1798, Aug 2000. (cited on page 1)

[7] C. Chin, R. Grimm, P. Julienne, and E. Tiesinga, "Feshbach resonances in ultracold gases," *Rev. Mod. Phys.*, vol. 82, pp. 1225–1286, Apr 2010. (cited on pages 1 and 8)

[8] M. Greiner, O. Mandel, T. Esslinger, T. Haensch, and I. Bloch, "Quantum phase transition from a superfluid to a Mott insulator in a gas of ultracold atoms," *Nature*, vol. 415, pp. 39–44, 02 2002. (cited on page 1)

[9] R. P. Feynman, "Simulating physics with computers," *International Journal of Theoretical Physics*, vol. 21, no. 6, pp. 467–488, 1982. (cited on page 1)

[10] I. M. Georgescu, S. Ashhab, and F. Nori, "Quantum simulation," *Rev. Mod. Phys.*, vol. 86, pp. 153–185, Mar 2014. (cited on page 1)

[11] M. Prüfer, P. Kunkel, H. Strobel, S. Lannig, D. Linnemann, C.-M. Schmied, J. Berges, T. Gasenzer, and M. K. Oberthaler, "Observation of universal dynamics in a spinor Bose gas far from equilibrium," *Nature*, vol. 563, no. 7730, pp. 217–220, 2018. (cited on page 1)

[12] S. Erne, R. Bücker, T. Gasenzer, J. Berges, and J. Schmiedmayer, "Universal dynamics in an isolated one-dimensional Bose gas far from equilibrium," *Nature*, vol. 563, no. 7730, pp. 225–229, 2018. (cited on page 1)

[13] C. Viermann, M. Sparn, N. Liebster, M. Hans, E. Kath, A. Parra-Lopez, M. Tolosa-Simeón, N. Sánchez-Kuntz, T. Haas, H. Strobel, S. Floerchinger, and M. K. Oberthaler, "Quantum field simulator for dynamics in curved spacetime," *Nature*, vol. 611, no. 7935, pp. 260–264, 2022. (cited on page 1)

[14] M. Tolosa-Simeón, A. Parra-López, N. Sánchez-Kuntz, T. Haas, C. Viermann, M. Sparn, N. Liebster, M. Hans, E. Kath, H. Strobel, M. K. Oberthaler, and S. Floerchinger, "Curved and expanding spacetime geometries in Bose-Einstein condensates," *Phys. Rev. A*, vol. 106, p. 033313, Sep 2022. (cited on page 1)

[15] I. Bloch, J. Dalibard, and W. Zwerger, "Many-body physics with ultracold gases," *Rev. Mod. Phys.*, vol. 80, pp. 885–964, Jul 2008. (cited on page 1)

[16] I. Bloch, J. Dalibard, and S. Nascimbène, "Quantum simulations with ultracold quantum gases," *Nature Physics*, vol. 8, no. 4, pp. 267–276, 2012. (cited on page 1)

[17] P. A. Lee, N. Nagaosa, and X.-G. Wen, "Doping a Mott insulator: Physics of high-temperature superconductivity," *Rev. Mod. Phys.*, vol. 78, pp. 17–85, Jan 2006. (cited on page 1)

[18] S. Hirthe, T. Chalopin, D. Bourgund, P. Bojović, A. Bohrdt, E. Demler, F. Grusdt, I. Bloch, and T. A. Hilker, "Magnetically mediated hole pairing in fermionic ladders of ultracold atoms," *Nature*, vol. 613, no. 7944, pp. 463–467, 2023. (cited on page 1)

[19] D. M. Weld and W. Ketterle, "Towards quantum magnetism with ultracold atoms," *Journal of Physics: Conference Series*, vol. 264, no. 1, p. 012017, jan 2011. (cited on page 1)

[20] C. J. Myatt, E. A. Burt, R. W. Ghrist, E. A. Cornell, and C. E. Wieman, "Production of two overlapping Bose-Einstein condensates by sympathetic cooling," *Phys. Rev. Lett.*, vol. 78, pp. 586–589, Jan 1997. (cited on pages 1 and 100)

[21] P. Maddaloni, M. Modugno, C. Fort, F. Minardi, and M. Inguscio, "Collective oscillations of two colliding Bose-Einstein condensates," *Phys. Rev. Lett.*, vol. 85, pp. 2413–2417, Sep 2000. (cited on pages 1 and 2)

[22] F. Schreck, L. Khaykovich, K. L. Corwin, G. Ferrari, T. Bourdel, J. Cubizolles, and C. Salomon, "Quasipure Bose-Einstein condensate immersed in a Fermi sea," *Phys. Rev. Lett.*, vol. 87, p. 080403, Aug 2001. (cited on page 1)

[23] A. G. Truscott, K. E. Strecker, W. I. McAlexander, G. B. Partridge, and R. G. Hulet, "Observation of Fermi pressure in a gas of trapped atoms," *Science*, vol. 291, no. 5513, pp. 2570–2572, 2001. (cited on page 1)

[24] Z. Hadzibabic, C. A. Stan, K. Dieckmann, S. Gupta, M. W. Zwierlein, A. Görlitz, and W. Ketterle, "Two-species mixture of quantum degenerate Bose and Fermi gases," *Phys. Rev. Lett.*, vol. 88, p. 160401, Apr 2002. (cited on page 1)

[25] G. Modugno, M. Modugno, F. Riboli, G. Roati, and M. Inguscio, "Two atomic species superfluid," *Phys. Rev. Lett.*, vol. 89, p. 190404, Oct 2002. (cited on page 1)

[26] A. Onuki, *Phase Transition Dynamics*. Cambridge: Cambridge University Press, 2002. (cited on page 1)

[27] H. Tanaka, "Viscoelastic phase separation," *Journal of Physics: Condensed Matter*, vol. 12, p. R207, Mar. 2000. (cited on page 1)

[28] H. Tanaka, "Phase separation in soft matter: the concept of dynamic asymmetry," in *Soft Interfaces: Lecture Notes of the Les Houches Summer School: Volume 98, July 2012*. Oxford University Press, 07 2017. (cited on page 1)

[29] J. Fan, T. Han, and M. Haataja, "Hydrodynamic effects on spinodal decomposition kinetics in planar lipid bilayer membranes," *The Journal of Chemical Physics*, vol. 133, no. 23, p. 235101, Dec. 2010. (cited on page 1)

[30] M. Tateno and H. Tanaka, "Power-law coarsening in network-forming phase separation governed by mechanical relaxation," *Nature Communications*, vol. 12, no. 1, p. 912, 2021. (cited on page 1)

[31] J. K. Hoffer and D. N. Sinha, "Dynamics of binary phase separation in liquid ^{3}–^{4}he mixtures," *Phys. Rev. A*, vol. 33, pp. 1918–1939, Mar 1986. (cited on page 2)

[32] D. S. Hall, M. R. Matthews, J. R. Ensher, C. E. Wieman, and E. A. Cornell, "Dynamics of component separation in a binary mixture of Bose-Einstein condensates," *Phys. Rev. Lett.*, vol. 81, pp. 1539–1542, Aug 1998. (cited on page 2)

[33] S. B. Papp, J. M. Pino, and C. E. Wieman, "Tunable miscibility in a dual-species Bose-Einstein condensate," *Phys. Rev. Lett.*, vol. 101, p. 040402, Jul 2008. (cited on page 2)

[34] S. Tojo, Y. Taguchi, Y. Masuyama, T. Hayashi, H. Saito, and T. Hirano, "Controlling phase separation of binary Bose-Einstein condensates via mixed-spin-channel Feshbach resonance," *Phys. Rev. A*, vol. 82, p. 033609, Sep 2010. (cited on page 2)

[35] E. Nicklas, H. Strobel, T. Zibold, C. Gross, B. A. Malomed, P. G. Kevrekidis, and M. K. Oberthaler, "Rabi flopping induces spatial demixing dynamics," *Phys. Rev. Lett.*, vol. 107, p. 193001, Nov 2011. (cited on page 2)

[36] E. Nicklas, "A new tool for miscibility control: Linear coupling," Ph.D. dissertation, University Heidelberg, 2013. (cited on pages 2, 12, and 13)

[37] E. Nicklas, W. Muessel, H. Strobel, P. G. Kevrekidis, and M. K. Oberthaler, "Nonlinear dressed states at the miscibility-immiscibility threshold," *Phys. Rev. A*, vol. 92, p. 053614, Nov 2015. (cited on page 2)

[38] D. J. McCarron, H. W. Cho, D. L. Jenkin, M. P. Köppinger, and S. L. Cornish, "Dual-species Bose-Einstein condensate of ^{87}Rb and ^{133}Cs," *Phys. Rev. A*, vol. 84, p. 011603, Jul 2011. (cited on page 2)

[39] K. M. Mertes, J. W. Merrill, R. Carretero-González, D. J. Frantzeskakis, P. G. Kevrekidis, and D. S. Hall, "Nonequilibrium dynamics and superfluid ring excitations in binary Bose-Einstein condensates," *Phys. Rev. Lett.*, vol. 99, p. 190402, Nov 2007. (cited on page 2)

[40] Y. Eto, M. Takahashi, K. Nabeta, R. Okada, M. Kunimi, H. Saito, and T. Hirano, "Bouncing motion and penetration dynamics in multicomponent Bose-Einstein condensates," *Phys. Rev. A*, vol. 93, p. 033615, Mar 2016. (cited on page 2)

[41] R. Saint-Jalm, "Exploring two-dimensional physics with Bose gases in box potentials: phase ordering and dynamical symmetry," Theses, Université Paris Sciences et Lettres, Oct. 2019. (cited on page 2)

[42] E. L. Cerf, "Demixing phenomena in 2D Bose gases," Ph.D. dissertation, Sorbonne Université, 2020. (cited on pages 2 and 11)

[43] S. De, D. L. Campbell, R. M. Price, A. Putra, B. M. Anderson, and I. B. Spielman, "Quenched binary Bose-Einstein condensates: Spin-domain formation and coarsening," *Phys. Rev. A*, vol. 89, p. 033631, Mar 2014. (cited on page 2)

[44] A. J. Bray, "Theory of phase-ordering kinetics," *Advances in Physics*, vol. 43, no. 3, pp. 357–459, Jun. 1994. (cited on page 2)

[45] J. Hofmann, S. S. Natu, and S. Das Sarma, "Coarsening dynamics of binary Bose condensates," *Phys. Rev. Lett.*, vol. 113, p. 095702, Aug 2014. (cited on page 2)

[46] V. P. Singh, L. Amico, and L. Mathey, "Thermal suppression of demixing dynamics in a binary condensate," *Phys. Rev. Res.*, vol. 5, p. 043042, Oct 2023. (cited on pages 2 and 11)

[47] J. Kondo, "Resistance Minimum in Dilute Magnetic Alloys," *Progress of Theoretical Physics*, vol. 32, no. 1, pp. 37–49, 07 1964. (cited on page 3)

[48] J. T. Devreese and A. S. Alexandrov, "Fröhlich polaron and bipolaron: recent developments," *Reports on Progress in Physics*, vol. 72, no. 6, p. 066501, may 2009. (cited on page 3)

[49] N. B. Jørgensen, L. Wacker, K. T. Skalmstang, M. M. Parish, J. Levinsen, R. S. Christensen, G. M. Bruun, and J. J. Arlt, "Observation of attractive and repulsive polarons in a Bose-Einstein condensate," *Phys. Rev. Lett.*, vol. 117, p. 055302, Jul 2016. (cited on page 3)

[50] M.-G. Hu, M. J. Van de Graaff, D. Kedar, J. P. Corson, E. A. Cornell, and D. S. Jin, "Bose polarons in the strongly interacting regime," *Phys. Rev. Lett.*, vol. 117, p. 055301, Jul 2016. (cited on page 3)

[51] Z. Z. Yan, Y. Ni, C. Robens, and M. W. Zwierlein, "Bose polarons near quantum criticality," *Science*, vol. 368, no. 6487, pp. 190–194, 2020. (cited on page 3)

[52] G. E. Astrakharchik and L. P. Pitaevskii, "Motion of a heavy impurity through a Bose-Einstein condensate," *Phys. Rev. A*, vol. 70, p. 013608, Jul 2004. (cited on page 3)

[53] F. M. Cucchietti and E. Timmermans, "Strong-coupling polarons in dilute gas Bose-Einstein condensates," *Phys. Rev. Lett.*, vol. 96, p. 210401, Jun 2006. (cited on page 3)

[54] R. M. Kalas and D. Blume, "Interaction-induced localization of an impurity in a trapped Bose-Einstein condensate," *Phys. Rev. A*, vol. 73, p. 043608, Apr 2006. (cited on page 3)

[55] J. Tempere, W. Casteels, M. K. Oberthaler, S. Knoop, E. Timmermans, and J. T. Devreese, "Feynman path-integral treatment of the BEC-impurity polaron," *Phys. Rev. B*, vol. 80, p. 184504, Nov 2009. (cited on page 3)

[56] S. P. Rath and R. Schmidt, "Field-theoretical study of the Bose polaron," *Phys. Rev. A*, vol. 88, p. 053632, Nov 2013. (cited on page 3)

[57] F. Grusdt and E. Demler, "New theoretical approaches to Bose polarons," *Proceedings of the International School of Physics "Enrico Fermi", volume 191: Quantum Matter at Ultralow Temperatures*, pp. 325 – 411, 2015. (cited on page 3)

[58] F. Scazza, M. Zaccanti, P. Massignan, M. M. Parish, and J. Levinsen, "Repulsive Fermi and Bose polarons in quantum gases," *Atoms*, vol. 10, no. 2, 2022. (cited on page 3)

[59] R. Schmidt and T. Enss, "Self-stabilized Bose polarons," *SciPost Phys.*, vol. 13, p. 054, 2022. (cited on page 3)

[60] M. Schecter and A. Kamenev, "Phonon-mediated Casimir interaction between mobile impurities in one-dimensional quantum liquids," *Phys. Rev. Lett.*, vol. 112, p. 155301, Apr 2014. (cited on pages 3 and 14)

[61] P. Naidon, "Two impurities in a Bose–Einstein condensate: From Yukawa to Efimov attracted polarons," *Journal of the Physical Society of Japan*, vol. 87, no. 4, p. 043002, 2018. (cited on pages 3 and 14)

[62] B. Reichert, Z. Ristivojevic, and A. Petković, "The Casimir-like effect in a one-dimensional Bose gas," *New Journal of Physics*, vol. 21, no. 5, p. 053024, May 2019. (cited on pages 3 and 14)

[63] M. Will, G. E. Astrakharchik, and M. Fleischhauer, "Polaron interactions and bipolarons in one-dimensional Bose gases in the strong coupling regime," *Phys. Rev. Lett.*, vol. 127, p. 103401, Aug 2021. (cited on pages 3 and 14)

[64] K. Fujii, M. Hongo, and T. Enss, "Universal van der Waals force between heavy polarons in superfluids," *Phys. Rev. Lett.*, vol. 129, p. 233401, Nov 2022. (cited on pages 3 and 14)

[65] H. B. G. Casimir, "On the attraction between two perfectly conducting plates," *Indag. Math.*, vol. 10, no. 4, pp. 261–263, 1948. (cited on page 3)

[66] H. B. G. Casimir and D. Polder, "The influence of retardation on the London-van der Waals forces," *Phys. Rev.*, vol. 73, pp. 360–372, Feb 1948. (cited on page 3)

[67] M. Sparnaay, "Measurements of attractive forces between flat plates," *Physica*, vol. 24, no. 6, pp. 751–764, 1958. (cited on page 3)

[68] G. Plunien, B. Müller, and W. Greiner, "The Casimir effect," *Physics Reports*, vol. 134, no. 2, pp. 87–193, 1986. (cited on page 3)

[69] S. K. Lamoreaux, "The Casimir force: background, experiments, and applications," *Reports on Progress in Physics*, vol. 68, no. 1, p. 201, nov 2004. (cited on page 3)

[70] A. Schirotzek, C.-H. Wu, A. Sommer, and M. W. Zwierlein, "Observation of Fermi polarons in a tunable Fermi liquid of ultracold atoms," *Phys. Rev. Lett.*, vol. 102, p. 230402, Jun 2009. (cited on page 3)

[71] T. A. Schulze, T. Hartmann, K. K. Voges, M. W. Gempel, E. Tiemann, A. Zenesini, and S. Ospelkaus, "Feshbach spectroscopy and dual-species Bose-Einstein condensation of ^{23}Na–^{39}K mixtures," *Phys. Rev. A*, vol. 97, p. 023623, Feb 2018. (cited on pages 3, 17, 39, 115, 116, and 117)

[72] T. Hartmann, T. A. Schulze, K. K. Voges, P. Gersema, M. W. Gempel, E. Tiemann, A. Zenesini, and S. Ospelkaus, "Feshbach resonances in ^{23}Na +^{39} K mixtures and refined molecular potentials for the NaK molecule," *Phys. Rev. A*, vol. 99, p. 032711, Mar 2019. (cited on pages 3 and 17)

[73] L. Pitaevskii and S. Stringari, *Bose-Einstein Condensation*, ser. International Series of Monographs on Physics. Clarendon Press, 2003. (cited on pages 5, 8, and 10)

[74] C. Pethick and H. Smith, *Bose-Einstein Condensation in Dilute Gases*. Cambridge University Press, 2002. (cited on pages 5 and 11)

[75] W. Ketterle, D. Durfee, and D. M. Stamper-Kurn, "Making, probing and understanding Bose-Einstein condensates," *arXiv: Condensed Matter*, 1999. (cited on pages 5, 48, and 81)

[76] F. Dalfovo, S. Giorgini, L. P. Pitaevskii, and S. Stringari, "Theory of Bose-Einstein condensation in trapped gases," *Rev. Mod. Phys.*, vol. 71, pp. 463–512, Apr 1999. (cited on page 5)

[77] E. P. Gross, "Structure of a quantized vortex in boson systems," *Il Nuovo Cimento (1955-1965)*, vol. 20, no. 3, pp. 454–477, 1961. (cited on page 6)

[78] L. P. Pitaevskii, "Vortex lines in an imperfect Bose gas," *Sov. Phys. JETP*, vol. 13, no. 2, p. 451, Aug. 1961. (cited on page 6)

[79] N. N. Bogolyubov, "On the theory of superfluidity," *J. Phys. (USSR)*, vol. 11, pp. 23–32, 1947. (cited on page 7)

[80] T. G. Tiecke, "Feshbach resonances in ultracold mixtures of the fermionic quantum gases 6Li and 40K," Ph.D. dissertation, University of Amsterdam, 2009. (cited on page 9)

[81] T.-L. Ho and V. B. Shenoy, "Binary mixtures of Bose condensates of alkali atoms," *Phys. Rev. Lett.*, vol. 77, pp. 3276–3279, Oct 1996. (cited on pages 10 and 14)

[82] P. Ao and S. T. Chui, "Binary Bose-Einstein condensate mixtures in weakly and strongly segregated phases," *Phys. Rev. A*, vol. 58, pp. 4836–4840, Dec 1998. (cited on page 10)

[83] G. Lamporesi, "Two-component spin mixtures," 2023. (cited on page 10)

[84] D. S. Petrov, "Quantum mechanical stabilization of a collapsing Bose-Bose mixture," *Phys. Rev. Lett.*, vol. 115, p. 155302, Oct 2015. (cited on page 11)

[85] C. R. Cabrera, L. Tanzi, J. Sanz, B. Naylor, P. Thomas, P. Cheiney, and L. Tarruell, "Quantum liquid droplets in a mixture of Bose-Einstein condensates," *Science*, vol. 359, no. 6373, pp. 301–304, 2018. (cited on page 11)

[86] G. Semeghini, G. Ferioli, L. Masi, C. Mazzinghi, L. Wolswijk, F. Minardi, M. Modugno, G. Modugno, M. Inguscio, and M. Fattori, "Self-bound quantum droplets of atomic mixtures in free space," *Phys. Rev. Lett.*, vol. 120, p. 235301, Jun 2018. (cited on page 11)

[87] L. Chomaz, S. Baier, D. Petter, M. J. Mark, F. Wächtler, L. Santos, and F. Ferlaino, "Quantum-fluctuation-driven crossover from a dilute Bose-Einstein condensate to a macrodroplet in a dipolar quantum fluid," *Phys. Rev. X*, vol. 6, p. 041039, Nov 2016. (cited on page 11)

[88] E. Timmermans, "Phase separation of Bose-Einstein condensates," *Phys. Rev. Lett.*, vol. 81, pp. 5718–5721, Dec 1998. (cited on pages 11 and 14)

[89] B. Bakkali-Hassani, C. Maury, Y.-Q. Zou, E. Le Cerf, R. Saint-Jalm, P. C. M. Castilho, S. Nascimbene, J. Dalibard, and J. Beugnon, "Realization of a Townes soliton in a two-component planar Bose gas," *Phys. Rev. Lett.*, vol. 127, p. 023603, Jul 2021. (cited on page 14)

[90] B. Bakkali-Hassani and J. Dalibard, "Townes soliton and beyond: Non-miscible Bose mixtures in 2D," 2022. (cited on page 14)

[91] H. Pu and N. P. Bigelow, "Properties of two-species Bose condensates," *Phys. Rev. Lett.*, vol. 80, pp. 1130–1133, Feb 1998. (cited on page 14)

[92] E. M. Gutierrez, G. A. de Oliveira, K. M. Farias, V. S. Bagnato, and P. C. M. Castilho, "Miscibility regimes in a 23Na–39K quantum mixture," *Applied Sciences*, vol. 11, no. 19, 2021. (cited on pages 15 and 16)

[93] K. L. Lee, N. B. Jørgensen, I.-K. Liu, L. Wacker, J. J. Arlt, and N. P. Proukakis, "Phase separation and dynamics of two-component Bose-Einstein condensates," *Phys. Rev. A*, vol. 94, p. 013602, Jul 2016. (cited on page 16)

[94] J. Stenger, S. Inouye, M. R. Andrews, H.-J. Miesner, D. M. Stamper-Kurn, and W. Ketterle, "Strongly enhanced inelastic collisions in a Bose-Einstein condensate near Feshbach resonances," *Phys. Rev. Lett.*, vol. 82, pp. 2422–2425, Mar 1999. (cited on pages 16 and 107)

[95] S. Knoop, T. Schuster, R. Scelle, A. Trautmann, J. Appmeier, M. K. Oberthaler, E. Tiesinga, and E. Tiemann, "Feshbach spectroscopy and analysis of the interaction potentials of ultracold sodium," *Phys. Rev. A*, vol. 83, p. 042704, Apr 2011. (cited on pages 16 and 107)

[96] C. D'Errico, M. Zaccanti, M. Fattori, G. Roati, M. Inguscio, G. Modugno, and A. Simoni, "Feshbach resonances in ultracold 39K," *New Journal of Physics*, vol. 9, no. 7, p. 223, Jul. 2007. (cited on pages 16, 107, 108, and 109)

[97] L. Tanzi, C. R. Cabrera, J. Sanz, P. Cheiney, M. Tomza, and L. Tarruell, "Feshbach resonances in potassium Bose-Bose mixtures," *Phys. Rev. A*, vol. 98, p. 062712, Dec 2018. (cited on pages 16 and 107)

[98] J. c. v. Etrych, G. Martirosyan, A. Cao, J. A. P. Glidden, L. H. Dogra, J. M. Hutson, Z. Hadzibabic, and C. Eigen, "Pinpointing Feshbach resonances and testing Efimov universalities in ^{39}K," *Phys. Rev. Res.*, vol. 5, p. 013174, Mar 2023. (cited on pages 16, 39, 107, 108, 109, and 116)

[99] A. Viel and A. Simoni, "Feshbach resonances and weakly bound molecular states of boson-boson and boson-fermion NaK pairs," *Phys. Rev. A*, vol. 93, p. 042701, Apr 2016. (cited on page 17)

[100] T. A. Schulze, "Quantum degenerate mixtures of 23Na - 39K and coherent transfer paths in NaK molecules," Ph.D. dissertation, Gottfried Wilhelm Leibniz Universität Hannover, 2018. (cited on pages 17, 102, and 115)

[101] T. Hartmann, "An experiment apparatus for the production of ultracold bosonic dipolar ground state 23Na39K molecules and Feshbach spectroscopy in a cold mixture of 23Na and 39K," Ph.D. dissertation, Gottfried Wilhelm Leibniz Universität Hannover, 2019. (cited on page 17)

[102] A. Mil, T. V. Zache, A. Hegde, A. Xia, R. P. Bhatt, M. K. Oberthaler, P. Hauke, J. Berges, and F. Jendrzejewski, "A scalable realization of local U(1) gauge invariance in cold atomic mixtures," *Science*, vol. 367, no. 6482, pp. 1128–1130, 2020. (cited on page 20)

[103] A. Mil, "Experimental realization of U(1) gauge invariance in ultracold atomic mixtures," Ph.D. dissertation, University Heidelberg, 2020. (cited on page 20)

[104] A. A. Hegde, "Noisy dynamics of U(1) lattice gauge theory in ultracold atomic mixtures," Ph.D. dissertation, University Heidelberg, 2022. (cited on page 20)

[105] X. Xia, "Towards a more reliable ultracold mixture platform," Ph.D. dissertation, University Heidelberg, 2022. (cited on pages 20 and 28)

[106] R. P. Bhatt, J. Kilinc, L. Höcker, and F. Jendrzejewski, "Stochastic dynamics of a few sodium atoms in presence of a cold potassium cloud," *Scientific Reports*, vol. 12, no. 1, p. 2422, 2022. (cited on page 20)

[107] R. P. Bhatt, "Developing tools for cold atom research : an ultracold Na-K experiment, proposals for unitary k-designs, and a web interface," Ph.D. dissertation, University Heidelberg, 2022. (cited on page 20)

[108] D. Steck, "Sodium D line data," 2003. (cited on pages 22, 94, and 104)

[109] T. G. Tiecke, "Properties of potassium," 2011. (cited on pages 22 and 92)

[110] D. W. Preston, "Doppler-free saturated absorption: Laser spectroscopy," *American Journal of Physics*, vol. 64, no. 11, pp. 1432–1436, 11 1996. (cited on page 23)

[111] J. Kilinc, "Starting a Na-K experiment for simulating quantum many-body phenomena," Master's thesis, University Heidelberg, 2019. (cited on pages 23 and 31)

[112] U. Schünemann, H. Engler, R. Grimm, M. Weidemüller, and M. Zielonkowski, "Simple scheme for tunable frequency offset locking of two lasers," *Review of Scientific Instruments*, vol. 70, no. 1, pp. 242–243, Jan. 1999. (cited on page 23)

[113] A. Weis and S. Derler, "Doppler modulation and Zeeman modulation: laser frequency stabilization without direct frequency modulation," *Appl. Opt.*, vol. 27, no. 13, pp. 2662–2665, Jul 1988. (cited on page 23)

[114] J. Hoffmann, "Implementation of a Zeeman-slower beam and an absorption imaging system for an ultracold mixture experiment," Bachelor's Thesis, University Heidelberg, 2023. (cited on page 24)

[115] E. A. Donley, T. P. Heavner, F. Levi, M. O. Tataw, and S. R. Jefferts, "Double-pass acousto-optic modulator system," *Review of Scientific Instruments*, vol. 76, no. 6, p. 063112, Jun 2005. (cited on page 24)

[116] N. Liebster, "Fast shutter design," GitHub repository, 2021. (cited on page 27)

[117] G. H. Zhang, B. Braverman, A. Kawasaki, and V. Vuletić, "Note: Fast compact laser shutter using a direct current motor and three-dimensional printing," *Review of Scientific Instruments*, vol. 86, no. 12, p. 126105, Dec. 2015. (cited on page 27)

[118] F. B. J. Buchkremer, R. Dumke, C. Buggle, G. Birkl, and W. Ertmer, "Low-cost setup for generation of 3 GHz frequency difference phase-locked laser light," *Review of Scientific Instruments*, vol. 71, no. 9, pp. 3306–3308, Sep. 2000. (cited on page 28)

[119] E. de Carlos-López, J. M. López, S. López, M. G. Espinosa, and L. A. Lizama, "Note: Laser frequency shifting by using two novel triple-pass acousto-optic modulator configurations," *Review of Scientific Instruments*, vol. 83, no. 11, p. 116102, Nov. 2012. (cited on page 28)

[120] C. Zhou, C. He, S.-T. Yan, Y.-H. Ji, L. Zhou, J. Wang, and M.-S. Zhan, "Laser frequency shift up to 5 GHz with a high-efficiency 12-pass 350-MHz acousto-optic modulator," *Review of Scientific Instruments*, vol. 91, no. 3, p. 033201, Mar 2020. (cited on page 28)

[121] B. Lu and D. Wang, "Note: A four-pass acousto-optic modulator system for laser cooling of sodium atoms," *Review of Scientific Instruments*, vol. 88, no. 7, p. 076105, Jul. 2017. (cited on page 28)

[122] F. V. Nicolai, "Design and construction of a fiber-coupled tapered amplifier system," Master's thesis, University Heidelberg, 2017. (cited on page 31)

[123] L. Hahn, "Setup of a tapered amplifier unit for application in an ultracold mixture experiment," Bachelor's Thesis, University Heidelberg, 2023. (cited on page 31)

[124] L. Ricci, C. Zimmermann, V. Vuletić, and T. W. Hänsch, "Generation of cylindrically symmetric magnetic fields with permanent magnets and μ-metal," *Applied Physics B*, vol. 59, no. 2, pp. 195–201, 1994. (cited on page 36)

[125] J. Tollett, C. Bradley, C. Sackett, and R. Hulet, "A permanent magnet trap for cold atoms," *Physical review. A*, vol. 51, pp. R22–R25, 02 1995. (cited on page 36)

[126] L. Höcker, Ph.D. dissertation, University Heidelberg, 2024. (cited on pages 37, 66, 103, and 126)

[127] T. G. Tiecke, S. D. Gensemer, A. Ludewig, and J. T. M. Walraven, "High-flux two-dimensional magneto-optical-trap source for cold lithium atoms," *Phys. Rev. A*, vol. 80, p. 013409, Jul 2009. (cited on page 37)

[128] G. Lamporesi, S. Donadello, S. Serafini, and G. Ferrari, "Compact high-flux source of cold sodium atoms," *Review of Scientific Instruments*, vol. 84, no. 6, p. 063102, Jun. 2013. (cited on page 37)

[129] M. Sparn, "Magnetic fields for cooling and trapping of potassium atoms," Bachelor's Thesis, University Heidelberg, 2017. (cited on page 38)

[130] K. Roux, B. Cilenti, V. Helson, H. Konishi, and J.-P. Brantut, "Compact bulk-machined electromagnets for quantum gas experiments," *SciPost Phys.*, vol. 6, p. 048, 2019. (cited on page 41)

[131] M. Hans, "Physical computing on a versatile setup for ultra-cold potassium," Ph.D. dissertation, University Heidelberg, 2022. (cited on pages 41, 47, 113, 128, and 129)

[132] C. Viermann, "Cosmological particle production and curved spaces in an ultracold quantum gas," Ph.D. dissertation, University Heidelberg, 2022. (cited on pages 41, 94, and 98)

[133] M. Hans, "An experimental setup for a potassium Bose-Einstein condensate with tunable interactions," Master's thesis, University Heidelberg, 2017. (cited on pages 45 and 129)

[134] L. R. F.R.S., "XXXI. Investigations in optics, with special reference to the spectroscope," *The London, Edinburgh, and Dublin Philosophical Magazine and Journal of Science*, vol. 8, no. 49, pp. 261–274, 1879. (cited on page 50)

[135] C. J. Picken, R. Legaie, and J. D. Pritchard, "Single atom imaging with an sCMOS camera," *Applied Physics Letters*, vol. 111, no. 16, p. 164102, Oct. 2017. (cited on page 51)

[136] T. B. Ottenstein, "A new objective for high resolution imaging of Bose-Einstein condensates," Diploma thesis, University Heidelberg, 2006. (cited on page 52)

[137] H. Talbot, "LXXVI. Facts relating to optical science. No. IV," *The London, Edinburgh, and Dublin Philosophical Magazine and Journal of Science*, vol. 9, no. 56, pp. 401–407, 1836. (cited on page 52)

[138] A. Mil, "Design and implementation of a versatile imaging objective for imaging of ultracold mixtures of sodium and lithium," Master's thesis, University Heidelberg, 2016. (cited on pages 52 and 53)

[139] G. Reinaudi, T. Lahaye, Z. Wang, and D. Guéry-Odelin, "Strong saturation absorption imaging of dense clouds of ultracold atoms," *Opt. Lett.*, vol. 32, no. 21, pp. 3143–3145, Nov 2007. (cited on page 58)

[140] M. Hans, F. Schmutte, C. Viermann, N. Liebster, M. Sparn, M. K. Oberthaler, and H. Strobel, "High signal to noise absorption imaging of alkali atoms at moderate

magnetic fields," *Review of Scientific Instruments*, vol. 92, no. 2, p. 023203, Feb. 2021. (cited on pages 59 and 113)

[141] E. L. Raab, M. Prentiss, A. Cable, S. Chu, and D. E. Pritchard, "Trapping of neutral sodium atoms with radiation pressure," *Phys. Rev. Lett.*, vol. 59, pp. 2631–2634, Dec 1987. (cited on page 62)

[142] C. Foot, *Atomic Physics*, ser. Oxford Master Series in Physics. OUP Oxford, 2005. (cited on page 62)

[143] H. Metcalf and P. Van der Straten, *Laser Cooling and Trapping*, ser. Graduate texts in contemporary physics. Springer, 1999. (cited on pages 62 and 67)

[144] M. Prentiss, A. Cable, J. E. Bjorkholm, S. Chu, E. L. Raab, and D. E. Pritchard, "Atomic-density-dependent losses in an optical trap," *Opt. Lett.*, vol. 13, no. 6, pp. 452–454, Jun 1988. (cited on page 63)

[145] T. Walker, D. Sesko, and C. Wieman, "Collective behavior of optically trapped neutral atoms," *Phys. Rev. Lett.*, vol. 64, pp. 408–411, Jan 1990. (cited on page 63)

[146] W. Ketterle, K. B. Davis, M. A. Joffe, A. Martin, and D. E. Pritchard, "High densities of cold atoms in a dark spontaneous-force optical trap," *Phys. Rev. Lett.*, vol. 70, pp. 2253–2256, Apr 1993. (cited on page 64)

[147] G. Colzi, "A new apparatus to simulate fundamental interactions with ultracold atoms," Ph.D. dissertation, Università degli Studi di Trento, 2018. (cited on pages 64 and 94)

[148] Z. Hadzibabic, "Studies of a quantum degenerate fermionic lithium gas," Ph.D. dissertation, Massachusetts Institute of Technology, 2003. (cited on pages 64, 88, 90, and 92)

[149] C.-H. Wu, "Strongly interacting quantum mixtures of ultracold atoms," Ph.D. dissertation, Massachusetts Institute of Technology, Dept. of Physics, 2013. (cited on pages 64 and 90)

[150] P. C. M. Castilho, "New experimental system to study coupled vortices in a two-species Bose-Einstein condensate 23Na-41K with tunable interactions," Ph.D. dissertation, Instituto de Física de São Carlos, University of São Paulo, São Carlos, 2017. (cited on page 64)

[151] P. C. M. Castilho, E. Pedrozo-Peñafiel, E. M. Gutierrez, P. L. Mazo, G. Roati, K. M. Farias, and V. S. Bagnato, "A compact experimental machine for studying tunable Bose–Bose superfluid mixtures," *Laser Physics Letters*, vol. 16, no. 3, p. 035501, Feb. 2019. (cited on pages 64, 88, and 89)

[152] J. Weiner, V. S. Bagnato, S. Zilio, and P. S. Julienne, "Experiments and theory in cold and ultracold collisions," *Rev. Mod. Phys.*, vol. 71, pp. 1–85, Jan 1999. (cited on pages 65 and 88)

[153] E. van Ooijen, "Realization and illumination of Bose-condensed sodium atoms," Ph.D. dissertation, Universiteit Utrecht, 2005. (cited on page 65)

[154] P. J. Ungar, D. S. Weiss, E. Riis, and S. Chu, "Optical molasses and multilevel atoms: theory," *J. Opt. Soc. Am. B*, vol. 6, no. 11, pp. 2058–2071, Nov 1989. (cited on page 67)

[155] J. Dalibard and C. Cohen-Tannoudji, "Laser cooling below the Doppler limit by polarization gradients: simple theoretical models," *J. Opt. Soc. Am. B*, vol. 6, no. 11, pp. 2023–2045, Nov 1989. (cited on pages 67 and 93)

[156] A. L. Migdall, J. V. Prodan, W. D. Phillips, T. H. Bergeman, and H. J. Metcalf, "First observation of magnetically trapped neutral atoms," *Phys. Rev. Lett.*, vol. 54, pp. 2596–2599, Jun 1985. (cited on page 67)

[157] A. Görlitz, T. L. Gustavson, A. E. Leanhardt, R. Löw, A. P. Chikkatur, S. Gupta, S. Inouye, D. E. Pritchard, and W. Ketterle, "Sodium Bose-Einstein condensates in the $F = 2$ state in a large-volume optical trap," *Phys. Rev. Lett.*, vol. 90, p. 090401, Mar 2003. (cited on pages 68 and 105)

[158] Z. Hadzibabic, S. Gupta, C. A. Stan, C. H. Schunck, M. W. Zwierlein, K. Dieckmann, and W. Ketterle, "Fiftyfold improvement in the number of quantum degenerate fermionic atoms," *Phys. Rev. Lett.*, vol. 91, p. 160401, Oct 2003. (cited on pages 68 and 92)

[159] K. M. R. van der Stam, A. Kuijk, R. Meppelink, J. M. Vogels, and P. van der Straten, "Spin-polarizing cold sodium atoms in a strong magnetic field," *Phys. Rev. A*, vol. 73, p. 063412, Jun 2006. (cited on page 68)

[160] K. M. R. van der Stam, E. D. van Ooijen, R. Meppelink, J. M. Vogels, and P. van der Straten, "Large atom number Bose-Einstein condensate of sodium," *Review of Scientific Instruments*, vol. 78, no. 1, p. 013102, Jan 2007. (cited on page 68)

[161] W. Petrich, M. H. Anderson, J. R. Ensher, and E. A. Cornell, "Stable, tightly confining magnetic trap for evaporative cooling of neutral atoms," *Phys. Rev. Lett.*, vol. 74, pp. 3352–3355, Apr 1995. (cited on page 70)

[162] K. B. Davis, M.-O. Mewes, M. A. Joffe, M. R. Andrews, and W. Ketterle, "Evaporative cooling of sodium atoms," *Phys. Rev. Lett.*, vol. 74, pp. 5202–5205, Jun 1995. (cited on pages 70 and 72)

[163] A. Toffali, "Production of ultracold sodium and potassium atomic mixture in an optical dipole trap," Master's thesis, Università degli Studi di Trento, 2013. (cited on page 70)

[164] W. Ketterle and N. V. Druten, "Evaporative cooling of trapped atoms," ser. Advances In Atomic, Molecular, and Optical Physics, B. Bederson and H. Walther, Eds. Academic Press, 1996, vol. 37, pp. 181–236. (cited on page 71)

[165] E. Majorana, *Oriented Atoms in a Variable Magnetic Field*, 04 2020, pp. 77–88. (cited on page 72)

[166] Y.-J. Lin, A. R. Perry, R. L. Compton, I. B. Spielman, and J. V. Porto, "Rapid production of ^{87}Rb Bose-Einstein condensates in a combined magnetic and optical potential," *Phys. Rev. A*, vol. 79, p. 063631, Jun 2009. (cited on page 72)

[167] H. P. Mishra, A. S. Flores, W. Vassen, and S. Knoop, "Efficient production of an 87Rb F = 2, mF = 2 Bose-Einstein condensate in a hybrid trap," *The European Physical Journal D*, vol. 69, no. 2, p. 52, 2015. (cited on page 72)

[168] S. Chu, J. E. Bjorkholm, A. Ashkin, and A. Cable, "Experimental observation of optically trapped atoms," *Phys. Rev. Lett.*, vol. 57, pp. 314–317, Jul 1986. (cited on page 74)

[169] D. M. Stamper-Kurn, M. R. Andrews, A. P. Chikkatur, S. Inouye, H.-J. Miesner, J. Stenger, and W. Ketterle, "Optical confinement of a Bose-Einstein condensate," *Phys. Rev. Lett.*, vol. 80, pp. 2027–2030, Mar 1998. (cited on page 74)

[170] R. Grimm, M. Weidemüller, and Y. B. Ovchinnikov, "Optical dipole traps for neutral atoms," ser. Advances In Atomic, Molecular, and Optical Physics, B. Bederson and H. Walther, Eds. Academic Press, 2000, vol. 42, pp. 95–170. (cited on pages 74 and 100)

[171] C. S. Adams, H. J. Lee, N. Davidson, M. Kasevich, and S. Chu, "Evaporative cooling in a crossed dipole trap," *Phys. Rev. Lett.*, vol. 74, pp. 3577–3580, May 1995. (cited on page 75)

[172] C. Simonelli, E. Neri, A. Ciamei, I. Goti, M. Inguscio, A. Trenkwalder, and M. Zaccanti, "Realization of a high power optical trapping setup free from thermal lensing effects," *Opt. Express*, vol. 27, no. 19, pp. 27 215–27 228, Sep 2019. (cited on page 76)

[173] Y. Castin and R. Dum, "Bose-Einstein condensates in time dependent traps," *Phys. Rev. Lett.*, vol. 77, pp. 5315–5319, Dec 1996. (cited on page 81)

[174] F. Dalfovo, C. Minniti, S. Stringari, and L. Pitaevskii, "Nonlinear dynamics of a Bose condensed gas," *Physics Letters A*, vol. 227, no. 3, pp. 259–264, 1997. (cited on page 81)

[175] D. S. Jin, J. R. Ensher, M. R. Matthews, C. E. Wieman, and E. A. Cornell, "Collective excitations of a Bose-Einstein condensate in a dilute gas," *Phys. Rev. Lett.*, vol. 77, pp. 420–423, Jul 1996. (cited on page 82)

[176] T. A. Savard, K. M. O'Hara, and J. E. Thomas, "Laser-noise-induced heating in far-off resonance optical traps," *Phys. Rev. A*, vol. 56, pp. R1095–R1098, Aug 1997. (cited on page 82)

[177] M. E. Gehm, K. M. O'Hara, T. A. Savard, and J. E. Thomas, "Dynamics of noise-induced heating in atom traps," *Phys. Rev. A*, vol. 58, pp. 3914–3921, Nov 1998. (cited on page 82)

[178] S. Friebel, C. D'Andrea, J. Walz, M. Weitz, and T. W. Hänsch, "co_2-laser optical lattice with cold rubidium atoms," *Phys. Rev. A*, vol. 57, pp. R20–R23, Jan 1998. (cited on page 84)

[179] H. Strobel, "Fisher information and entanglement of non-Gaussian spin states," Ph.D. dissertation, University Heidelberg, 2016. (cited on page 84)

[180] M. S. Santos, P. Nussenzveig, A. Antunes, P. S. P. Cardona, and V. S. Bagnato, "Hyperfine-changing collision measurements in trap loss for mixed species in a magneto-optical trap," *Phys. Rev. A*, vol. 60, pp. 3892–3895, Nov 1999. (cited on page 88)

[181] S. Sutradhar, A. Misra, G. Pal, S. Majumder, S. Roy, and S. Chaudhuri, "Fast loaded dual species magneto optical trap of cold sodium and potassium atoms with light-assisted inter-species interaction," *AIP Advances*, vol. 13, no. 6, p. 065317, 06 2023. (cited on pages 88, 89, and 90)

[182] A. Fuhrmanek, R. Bourgain, Y. R. P. Sortais, and A. Browaeys, "Light-assisted collisions between a few cold atoms in a microscopic dipole trap," *Phys. Rev. A*, vol. 85, p. 062708, Jun 2012. (cited on page 89)

[183] G. D. Telles, W. Garcia, L. G. Marcassa, V. S. Bagnato, D. Ciampini, M. Fazzi, J. H. Müller, D. Wilkowski, and E. Arimondo, "Trap loss in a two-species Rb-Cs magneto-optical trap," *Phys. Rev. A*, vol. 63, p. 033406, Feb 2001. (cited on page 88)

[184] S. Dutta, A. Altaf, J. Lorenz, D. S. Elliott, and Y. P. Chen, "Interspecies collision-induced losses in a dual species 7Li–85Rb magneto-optical trap," *Journal of Physics B: Atomic, Molecular and Optical Physics*, vol. 47, no. 10, p. 105301, May 2014. (cited on pages 88 and 90)

[185] L. Wacker, N. B. Jørgensen, D. Birkmose, R. Horchani, W. Ertmer, C. Klempt, N. Winter, J. Sherson, and J. J. Arlt, "Tunable dual-species Bose-Einstein condensates of ^{39}K and ^{87}Rb," *Phys. Rev. A*, vol. 92, p. 053602, Nov 2015. (cited on page 90)

[186] C. Glück, "Quenching of light-assisted collisionsin an optical two-species atom trap," Master's thesis, Albert-Ludwigs-Universität Freiburg, 2008. (cited on page 90)

[187] B. Bussery, Y. Achkar, and M. Aubert-Frécon, "Long-range molecular states dissociating to the three or four lowest asymptotes for the ten heteronuclear diatomic alkali molecules," *Chemical Physics*, vol. 116, no. 3, pp. 319–338, 1987. (cited on page 90)

[188] H. Wang, P. L. Gould, and W. C. Stwalley, "Photoassociative spectroscopy of ultracold ^{39}K atoms in a high-density vapor-cell magneto-optical trap," *Phys. Rev. A*, vol. 53, pp. R1216–R1219, Mar 1996. (cited on page 90)

[189] N. W. Buchheim, "Dual-species apparatus for creating a dipolar quantum gas of 23Na40K molecules," Ph.D. dissertation, Ludwig-Maximilians-Universität München, 2015. (cited on page 90)

[190] J. W. Park, C.-H. Wu, I. Santiago, T. G. Tiecke, S. Will, P. Ahmadi, and M. W. Zwierlein, "Quantum degenerate Bose-Fermi mixture of chemically different atomic species with widely tunable interactions," *Phys. Rev. A*, vol. 85, p. 051602, May 2012. (cited on pages 90 and 91)

[191] J. Appmeier, "Immersed quantum systems: A sodium Bose-Einstein condensate for polaron studies," Ph.D. dissertation, University Heidelberg, 2010. (cited on page 92)

[192] M. Weidemüller, T. Esslinger, M. A. Ol'shanii, A. Hemmerich, and T. W. Hänsch, "A novel scheme for efficient cooling below the photon recoil limit," *Europhysics Letters*, vol. 27, no. 2, p. 109, jul 1994. (cited on page 93)

[193] A. Aspect, E. Arimondo, R. Kaiser, N. Vansteenkiste, and C. Cohen-Tannoudji, "Laser cooling below the one-photon recoil energy by velocity-selective coherent population trapping," *Phys. Rev. Lett.*, vol. 61, pp. 826–829, Aug 1988. (cited on page 93)

[194] D. Nath, R. K. Easwaran, G. Rajalakshmi, and C. S. Unnikrishnan, "Quantum-interference-enhanced deep sub-Doppler cooling of ^{39}K atoms in gray molasses," *Phys. Rev. A*, vol. 88, p. 053407, Nov 2013. (cited on pages 94 and 97)

[195] G. Salomon, L. Fouché, P. Wang, A. Aspect, P. Bouyer, and T. Bourdel, "Gray-molasses cooling of 39K to a high phase-space density," *Europhysics Letters*, vol. 104, no. 6, p. 63002, Jan. 2014. (cited on page 94)

[196] G. Colzi, G. Durastante, E. Fava, S. Serafini, G. Lamporesi, and G. Ferrari, "Sub-Doppler cooling of sodium atoms in gray molasses," *Phys. Rev. A*, vol. 93, p. 023421, Feb 2016. (cited on pages 94, 97, 99, and 120)

[197] A. A. Beikert, "Controlled frequency generation for grey molasses cooling," Bachelor's Thesis, University Heidelberg, 2021. (cited on page 98)

[198] G. Modugno, G. Ferrari, G. Roati, R. J. Brecha, A. Simoni, and M. Inguscio, "Bose-Einstein condensation of potassium atoms by sympathetic cooling," *Science*, vol. 294, no. 5545, pp. 1320–1322, 2001. (cited on page 100)

[199] G. Delannoy, S. G. Murdoch, V. Boyer, V. Josse, P. Bouyer, and A. Aspect, "Understanding the production of dual Bose-Einstein condensation with sympathetic cooling," *Phys. Rev. A*, vol. 63, p. 051602, Apr 2001. (cited on page 102)

[200] T. Weber, J. Herbig, M. Mark, H.-C. Nägerl, and R. Grimm, "Bose-Einstein condensation of cesium," *Science*, vol. 299, no. 5604, pp. 232–235, 2003. (cited on page 102)

[201] C.-L. Hung, X. Zhang, N. Gemelke, and C. Chin, "Accelerating evaporative cooling of atoms into Bose-Einstein condensation in optical traps," *Phys. Rev. A*, vol. 78, p. 011604, Jul 2008. (cited on page 102)

[202] M. Repp, "Interspecies Feshbach resonances in an ultracold, optically trapped Bose-Fermi mixture of cesium and lithium," Ph.D. dissertation, University Heidelberg, 2013. (cited on page 102)

[203] A. Burchianti, C. D'Errico, M. Prevedelli, L. Salasnich, F. Ancilotto, M. Modugno, F. Minardi, and C. Fort, "A dual-species Bose-Einstein condensate with attractive interspecies interactions," *Condensed Matter*, vol. 5, no. 1, 2020. (cited on page 102)

[204] G. Breit and I. I. Rabi, "Measurement of nuclear spin," *Phys. Rev.*, vol. 38, pp. 2082–2083, Dec 1931. (cited on page 104)

[205] G. Roati, M. Zaccanti, C. D'Errico, J. Catani, M. Modugno, A. Simoni, M. Inguscio, and G. Modugno, "^{39}K Bose-Einstein condensate with tunable interactions," *Phys. Rev. Lett.*, vol. 99, p. 010403, Jul 2007. (cited on page 107)

[206] T. Lauber, J. Küber, O. Wille, and G. Birkl, "Optimized Bose-Einstein-condensate production in a dipole trap based on a 1070-nm multifrequency laser: Influence of enhanced two-body loss on the evaporation process," *Phys. Rev. A*, vol. 84, p. 043641, Oct 2011. (cited on page 111)

[207] S. Kumar, S. Hirai, Y. Suzuki, M. Kachi, M. Sadgrove, and K. Nakagawa, "Simple and fast production of Bose–Einstein condensate in a 1 μm cross-beam dipole trap," *Journal of the Physical Society of Japan*, vol. 81, p. 084004, 08 2012. (cited on page 111)

[208] M. Landini, S. Roy, G. Roati, A. Simoni, M. Inguscio, G. Modugno, and M. Fattori, "Direct evaporative cooling of ^{39}K atoms to Bose-Einstein condensation," *Phys. Rev. A*, vol. 86, p. 033421, Sep 2012. (cited on page 111)

[209] T. Maier, "Interactions in a quantum gas of dysprosium atoms," Ph.D. dissertation, University Stuttgart, 2015. (cited on page 111)

[210] W. Hung, P. Huang, F.-C. Wu, M. Bruvelis, H.-Y. Xiao, A. Ekers, and I. A. Yu, "Storage time of cold Rb atoms in an optical dipole trap formed by a multimode fiber laser," *J. Opt. Soc. Am. B*, vol. 32, no. 5, pp. B32–B36, May 2015. (cited on page 111)

[211] C. R. Menegatti, B. S. Marangoni, J. Tallant, and L. G. Marcassa, "Simultaneous loading of ^{39}K and Rb into a crossed dipole trap: Characterization and two-body losses," *Phys. Rev. A*, vol. 88, p. 023411, Aug 2013. (cited on page 113)

[212] Y. Cui, C. Shen, M. Deng, S. Dong, C. Chen, R. Lü, B. Gao, M. K. Tey, and L. You, "Observation of broad d-wave Feshbach resonances with a triplet structure," *Phys. Rev. Lett.*, vol. 119, p. 203402, Nov 2017. (cited on page 114)

[213] J. Li, J. Liu, L. Luo, and B. Gao, "Three-body recombination near a narrow Feshbach resonance in ^{6}Li," *Phys. Rev. Lett.*, vol. 120, p. 193402, May 2018. (cited on page 114)

[214] L. Fouché, A. Boissé, G. Berthet, S. Lepoutre, A. Simoni, and T. Bourdel, "Quantitative analysis of losses close to a d-wave open-channel Feshbach resonance in ^{39}K," *Phys. Rev. A*, vol. 99, p. 022701, Feb 2019. (cited on page 114)

[215] M.-J. Zhu, H. Yang, L. Liu, D.-C. Zhang, Y.-X. Liu, J. Nan, J. Rui, B. Zhao, J.-W. Pan, and E. Tiemann, "Feshbach loss spectroscopy in an ultracold ^{23}Na $-^{40}$ K mixture," *Phys. Rev. A*, vol. 96, p. 062705, Dec 2017. (cited on page 115)

[216] A. Görlitz, J. M. Vogels, A. E. Leanhardt, C. Raman, T. L. Gustavson, J. R. Abo-Shaeer, A. P. Chikkatur, S. Gupta, S. Inouye, T. Rosenband, and W. Ketterle, "Realization of Bose-Einstein condensates in lower dimensions," *Phys. Rev. Lett.*, vol. 87, p. 130402, Sep 2001. (cited on page 125)

[217] P. Cladé, C. Ryu, A. Ramanathan, K. Helmerson, and W. D. Phillips, "Observation of a 2D Bose gas: From thermal to quasicondensate to superfluid," *Phys. Rev. Lett.*, vol. 102, p. 170401, Apr 2009. (cited on page 125)

[218] J. Szczepkowski, R. Gartman, M. Witkowski, L. Tracewski, M. Zawada, and W. Gawlik, "Analysis and calibration of absorptive images of Bose–Einstein condensate at nonzero temperatures," *Review of Scientific Instruments*, vol. 80, no. 5, p. 053103, May 2009. (cited on pages 135 and 136)

[219] M. A. Kristensen, "Atom number fluctuations in Bose-Einstein condensates," Ph.D. dissertation, Aarhus University, 2018. (cited on page 135)

[220] H. Kadau, "A dipolar Bose-Einstein condensate in a one-dimensional optical lattice," Diploma thesis, University Stuttgart, 2011. (cited on page 136)

Acknowledgements

Looking back on my doctoral studies, I feel grateful for all the invaluable support over the years and want to express my sincere appreciation to those who have made this journey possible.

- First and foremost, I would like to thank Markus for accepting me into his amazing group. Your guidance and infectious optimism were especially valuable during the uncertain transition period and the redesign and setup of our cool new mixtures experiment.

- Special thanks to Lauriane for reviewing this work.

- I want to thank Lilo and Rohit. We started setting up this experiment almost six years ago, and it has been quite the journey. It has been a great team effort, and I really enjoyed the work with you in the lab, all the nice evenings where we ordered Indian food, and just in general the time we spent together.

- Many thanks go to Helmut, who taught me so many things in and around the lab and (somehow) always had time for questions about experimental details. Even when things did not go as planned, you were always there to help out and never panicked but always remained calm. Without you and Lilo, the massive disruptive transformation of our experiment would simply not have been possible.

- Sincere thanks to Fred for giving me the opportunity all these years back and putting your trust in me with this (tricky) mixture machine.

- I also want to thank all the current and former members of the SoPa/NaLi/NaKa family. Toni and Brian, I enjoyed the (short) time we had together in the lab, and I am absolutely certain that the experiment is in good hands now. Thanks should also go to Lisa and Maurus. During the short time you spent in the SoPa team, you have been of immense help in the lab prior and during the lab transformation. I am also grateful to Andy for injecting positivity and a bit of craziness when it came to ordering surprising amounts of food or just the usual banter.

- I thank the entire SynQS group. I really enjoyed the daily lunch discussions (even though I was not always contributing much), the insightful labtalks, and the fantastic atmosphere during our two amazing group retreats.
- Heartfelt thanks to Christiane, Dagmar, and Petra for their continuous help and support.
- Thanks to Oscar Martin-Almendral and Corina Müller for processing countless orders and helping with the confusing order forms.
- I would like to thank to David, Julia, and Herr Lamade from the mechanic workshop. I remember countless times when we urgently needed some parts do be precisely cut, milled, or drilled, and your door was always open. Not only was the end result always perfect, but I really enjoyed our discussions on how to improve the design or solve certain problems in the lab.
- And last but certainly not least, I want to thank my entire family! Your support means the world, and I could not have done any of this without you.

”Topic closed!”

Erklärung

Ich versichere, dass ich diese Arbeit selbstständig verfasst und keine anderen als die angegebenen Quellen und Hilfsmittel benutzt habe.

Heidelberg, den 27. November 2023, _____

Jan Kilinc